Selected Cover Images
Cosan Caglayan, Georgios C. Trichopoulos, and Kubilay Sertel:
Hybrid Electromagnetic Modeling of Lens-Integrated Antennas for Non-Contact On-Wafer Characterization of THz Devices and Integrated Circuits - (Bottom Left, Bottom Center, and Right)

GENERAL INFORMATION

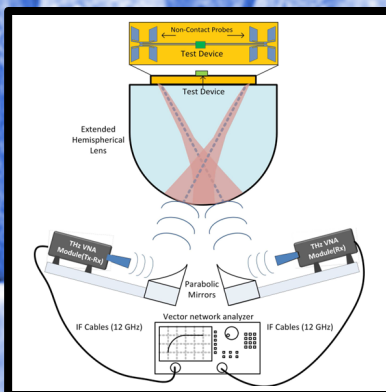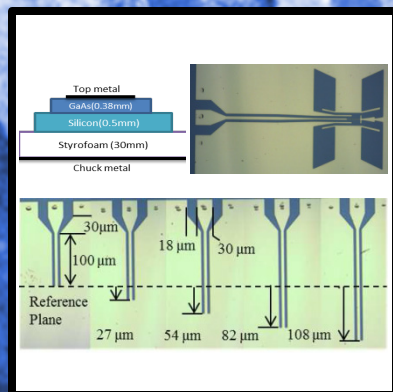**PURPOSE AND SCOPE:** The Applied Computational Electromagnetics Society *(ACES) Express* Journal hereinafter known as the ***ACES Express Journal*** is devoted to the timely and rapid exchange of information in computational electromagnetics, to the advancement of the state-of-the art, and the promotion of related technical activities. The primary objective of the information exchange is to inform the scientific community in a short amount of time on the developments of recent computational electromagnetics tools and their use in electrical engineering, physics, or related areas. The technical activities promoted by this publication include code validation, performance analysis, and input/output standardization; code or technique optimization and error minimization; innovations in solution technique or in data input/output; identification of new applications for electromagnetics modeling codes and techniques; integration of computational electromagnetics techniques with new computer architectures; and correlation of computational parameters with physical mechanisms.

SUBMISSIONS: The ***ACES Express Journal*** welcomes original, previously unpublished papers, relating to applied computational electromagnetics. Typical papers will represent the computational electromagnetics aspects of research in electrical engineering, physics, or related disciplines as well as research in the field of applied computational electromagnetics.

Manuscripts are to be submitted through the upload system of ***ACES*** web site http://aces-society.org Please see "Information for Authors" on inside of back cover and at ***ACES*** web site. For additional information contact the Editor-in-Chief:

Dr. Ozlem Kilic
Department of Electrical Engineering and Computer Science
The Catholic University of America
Washington, DC 20064
Email: kilic@cua.edu

SUBSCRIPTIONS: All members of the Applied Computational Electromagnetics Society are entitled to access and download the ***ACES Express Journal*** of any published journal article available at http://aces-society.org. ***ACES Express Journal*** is an online journal and printed copies are not available. Subscription to ACES is through the web site.

LIABILITY. Neither ***ACES***, nor the ***ACES Express Journal*** editors, are responsible for any consequence of misinformation or claims, express or implied, in any published material in an ***ACES Express Journal*** issue. This also applies to advertising, for which only camera-ready copies are accepted. Authors are responsible for all information contained in their papers. If any material submitted for publication includes material which has already been published elsewhere, it is the author's responsibility to obtain written permission to reproduce such material.

THE APPLIED COMPUTATIONAL ELECTROMAGNETICS SOCIETY EXPRESS JOURNAL

TABLE OF CONTENTS

Assessment of ALEGRA Computation for Magnetostatic Configurations

Michael Grinfeld [1], John Niederhaus [2], and Andrew Porwitzky [1]

[1] The U.S. Army Research Laboratory
Aberdeen Proving Ground, MD 21005, USA

[2] Sandia National Laboratories
Albuquerque, NM 87185, USA

Abstract — A closed-form solution is described here for the equilibrium configurations of the magnetic field in a simple heterogeneous domain. This problem and its solution are used for rigorous assessment of the accuracy of the ALEGRA code in the quasistatic limit. By the equilibrium configuration we understand the static condition, or the stationary states without macroscopic current. The analysis includes quite a general class of 2D solutions for which a linear isotropic metallic matrix is placed inside a stationary magnetic field approaching a constant value $H_i°$ at infinity. The process of evolution of the magnetic fields inside and outside the inclusion and the parameters for which the quasi-static approach provides for self-consistent results is also explored. It is demonstrated that under spatial mesh refinement, ALEGRA converges to the analytic solution for the interior of the inclusion at the expected rate, for both body-fitted and regular rectangular meshes.

Index Terms — Electrostatics, exact solutions, magnetohydrodynamics, magnetostatics, verification and validation.

I. INTRODUCTION

Computational electromagnetics is a strong and continually growing area within modern applied electromagnetics. Computational electromagnetics tools are introducing new insights in many technical fields and contributing to the development of new measurement techniques. The soundness of these insights depends on rigorous assessment, or verification and validation (V&V), of these tools. Presented here is a simple problem in magnetostatics, and an analytic solution, which are useful for verification of computational electromagnetics capabilities.

Assessment is applied here to the computational electromagnetics code ALEGRA, which is currently being used successfully in development of laboratory electromagnetic measurement techniques. [1] ALEGRA is a multipurpose code handling a variety of mechanical and electromagnetic phenomena. This multiphysics capability is a key feature of ALEGRA. Here we assess the accuracy of the portion of the ALEGRA code used to compute transient magnetic diffusion, for a problem involving a permeable, conducting inclusion in a magnetized medium.

The project pursues two goals. First, we explore in the quasi-static approximation the process of evolution of the magnetic fields inside and outside the inclusion and the parameters for which the quasi-static approach in ALEGRA provides for self-consistent results. Second, we explore how reliable ALEGRA is in its static limit. By the static limit we understand the stationary states without macroscopic current. We choose quite a general class of 2D solutions for which a linear isotropic metallic matrix is placed inside a stationary magnetic field approaching a constant value $H_i°$ at infinity.

In this paper, we begin by reviewing the system of equations used to describe quasistatic magnetization and formulating our master system. Next, we analyze the equilibrium configuration of the magnetic field for an elliptical cylinder of linear isotropic material immersed in a 2D uniform magnetic field $H_i°$. The solution outside the ellipse is quite complex, however, inside it is remarkably simple. Therefore, this solution is very convenient for the verification purposes. We describe the ALEGRA code and the setup of the simulations, as well as the quasistatic evolution computed by the code. The quantitative verification analysis concludes the paper.

II. MHD MASTER SYSTEM

In the theoretical part of this project we follow the classical textbook of theoretical physics [1]. The analysis of quasi-statics is based on the following reduced Maxwell system:

$$z^{ijk}\nabla_j E_k = -\frac{1}{c}\frac{\partial B^i}{\partial t}, \qquad z^{ijk}\nabla_j H_k = \frac{4\pi}{c}J^i. \qquad (1)$$

These bulk partial differential equations should be augmented with the constitutive equations $J^i = \sigma^{ij}E_j$ (Ohm's law), the constitutive equation $B^i = B^i(H^k)$, boundary conditions $[B^i]^\pm_\pm n_i = 0$, $[H^i]^\pm_\pm \tau_i = 0$, the conditions at infinity, and appropriate initial conditions.

Here, z^i and t are the spatial (Eulerian) Cartesian coordinates and time; E_i, H_i, and B_i are the electric and magnetic field and magnetic induction, respectively; J_i is the electric current density of free charges, c is the speed of light in vacuum, σ_{ij} is electrical conductivity. In the boundary conditions, n_i and τ_i are the normal and the tangent vectors to the discontinuity boundaries.

Other notation is the following. The metrics co- and contra-variant tensors z_{ij}, z^{ij} of the Eulerian coordinate system are used for lowering and raising ("juggling") the indexes, and for defining the covariant differentiation ∇_i with respect to the coordinates z^i; z_{ijk} is the so-called covariant Levi-Civita skew-symmetric tensor. Using tensor notation permits one to present all the equations in the universal covariant (i.e., coordinate-independent) form.

The ALEGRA code uses the vector potential A_i. The vectors A_i and H_i are interconnected by the covariant differential relation $H^i = z^{ijk}\nabla_j A_k$. With a known spatial distribution of the vector potential $A(z,t)$ one can immediately and explicitly recover the magnetic field H_i.

III. ELLIPTIC PLATE

There are few exact 2D and 3D solutions of the MHD master system. For the static equilibrium configuration a closed form solution can be obtained for an elliptic inclusion in an infinite isotropic matrix, in particular, in vacuum [2], [1], [3], [4]. This solution is described below and used in our project for verification purposes.

Consider an ellipse with the semi-axes a and b coinciding with the Cartesian axes z^1 and z^2. We assume that the elliptical domain is filled with a linear isotropic substance with magnetic permeability μ. We then assume that the ellipse is immersed in the unbounded space in which there is a uniform magnetic field $H^{i\circ}$. If there is an elliptical inclusion, the otherwise uniform field $H^i = H^{i\circ}$ will change. The changes are particularly strong inside the ellipse and in its vicinity. At infinity, the newly generated field H^i approaches its original value $H^{i\circ}$.

This problem was analyzed by many outstanding mathematicians and physicists working on it since Newton's times. First, it was focused on various problems of gravitation and cosmology. The exact solution of this problem has the following form.

a) Outside the ellipse:

$$H_{out}^1 = \left(\alpha \frac{\partial^2 \Theta}{\partial z^1 \partial z^1} + 1\right)H^{1\circ} + \beta \frac{\partial^2 \Theta}{\partial z^1 \partial z^2},$$

$$H_{out}^2 = \alpha \frac{\partial^2 \Theta}{\partial z^2 \partial z^1}H^{1\circ} + \beta \left(\frac{\partial^2 \Theta}{\partial z^2 \partial z^2} + 1\right)H^{2\circ}. \tag{2}$$

b) Inside the ellipse:

$$H_{ins}^1 = \frac{a+b}{a+\mu b}H^{1\circ}, \quad H_{ins}^2 = \frac{a+b}{\mu a + b}H^{2\circ}, \tag{3}$$

where $2\pi\alpha = (\mu-1)(a+b)/(a+\mu b)$, and $2\pi\beta = (\mu-1)(a+b)/(\mu a + b)$. The logarithmic potential of the ellipse $\Theta(z)$ is given by the relationship:

$$\Theta(z) = \int_{\omega_{ell}} d\omega^* d\ln|z - z^*|. \tag{4}$$

Analysis for related magnetic diffusion problems appears throughout the literature. Knoepfel [5] considered linear and nonlinear magnetic diffusion for simple geometries and non-permeable materials. Woodson and Melcher [6] analyzed permeable materials, but only for a slab geometry. Brauer [7] considered slabs and cylinders with linear and nonlinear permeability and finite-element modeling. Here we consider linear permeability with an elliptical geometry.

IV. NUMERICAL MODEL

The "transient magnetics" module of the ALEGRA MHD code [8], [9] (henceforward ALEGRA) computes solutions to the reduced Maxwell system of Equation 1 in quasi-static fashion. It is assumed that the medium is stationary, with variable electrical conductivity σ and fixed magnetic permeability μ. The system is recast in terms of the vector potential A_i and transformed to SI units, and appropriate constitutive relationships are incorporated. These include Ohm's law $J^i = \sigma E^i$, and a simple linear relationship between the magnetic field and the magnetic induction, $B^i = \mu H^i$. An implicit linear solver is used to solve the system with an unstructured finite-element discretization, and evolve the solution forward in time.

ALEGRA is equipped to handle a much broader class of problems, including deforming media, mechanical and electromagnetic forces, and adiabatic and Ohmic sources of heating. These are encompassed within ALEGRA's broader magneto-hydrodynamics (MHD) capability. For the present work, only the transient magnetics module is considered. The scope of the simulations here is restricted to the two-dimensional system described in Section III, treated in ALEGRA as an initial boundary value problem whose final state should be equilibrium.

This problem is shown schematically in Fig. 1. The simulations assume geometric parameters $a = 1.8$ cm and $b = 0.56$ cm, which imply an ellipse with an eccentricity of 0.831 and an aspect ratio of 3.24. A fixed magnetic tangential field $H^\circ = (0, 1/\mu_0)$ Ampere/m is imposed on the left and right boundaries, with zero tangential field on the top and bottom. For the ellipse, a magnetic permeability of $3\mu_0$, and a constant isotropic electrical

conductivity of 10^7 S/m are used. The exterior has the permeability of free space, and an electrical conductivity of 10^{-6} S/m. The magnetic field is initially zero everywhere except on the domain boundary. At equilibrium, the exact solution given in Equation 3 predicts a uniform magnetic induction $B_1 = 0$ in the horizontal direction and $B_2 = 1.18657$ Tesla in the vertical direction, in the ellipse interior.

Two quadrilateral finite-element mesh configurations are used here in the attempt to capture this solution: (1) a simple regular rectangular mesh with multimaterial elements, and (2) a more complex irregular mesh fitted to the ellipse surface. In the former case, ALEGRA uses volume-averaged values of σ and μ in multimaterial elements. The meshes are chosen to provide roughly the same number of elements inside the ellipse for the two cases, to facilitate comparison.
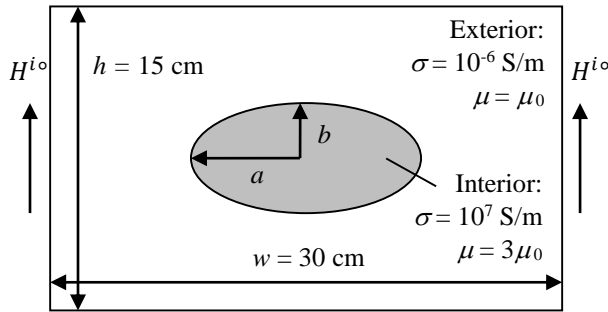
Fig. 1. Schematic layout (not to scale) for problem studied here showing elliptical inclusion.

V. TIME EVOLUTION

The equilibrium solution is obtained in ALEGRA in quasi-static fashion, by a series of timesteps capturing the time evolution. The time required to reach equilibrium can be approximated with a scaling relationship that arises from the 1D magnetic diffusion Equation [3], giving a diffusion time $\tau = \mu\sigma l^2$, where l is a characteristic length scale.

Using the shortest ellipse dimension ($b = 0.56$ cm), we obtain $\tau = 1.2$ ms as the time for one e-fold increase of the interior field magnitude. Therefore, the simulations are run out to a termination time of 0.01 seconds, in order to capture eight e-foldings, and ensure that a fully diffused field can be captured. The timestep size is fixed in this study to $dt = 2$ μs, so that 5000 timesteps are modeled.

The time evolution computed by ALEGRA is shown in Fig. 2. Here we see, as expected, that the magnetic field imposed at the boundary gradually diffuses into the elliptical inclusion, leading ultimately to a nearly uniform interior field. The exterior field is highly nonuniform, with the largest gradients appearing near the poles along the major axis of the ellipse.
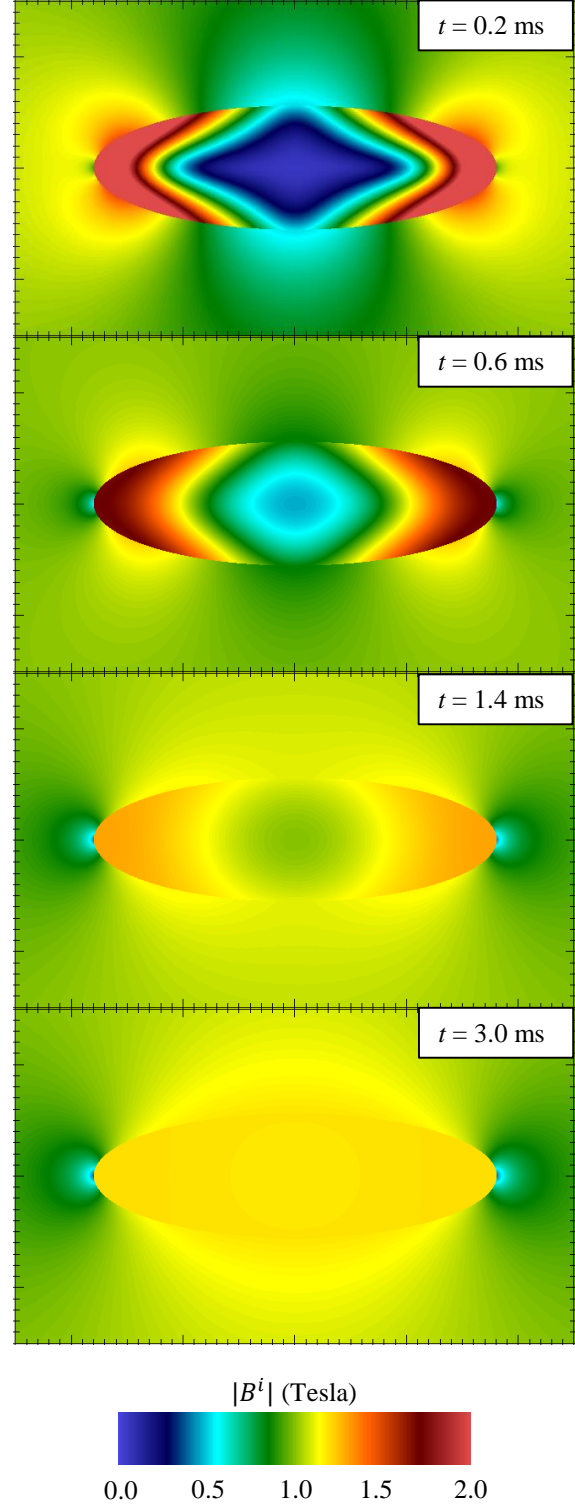
Fig. 2. ALEGRA simulation evolution (zoomed-in): magnetic induction magnitude for a body-fitted mesh with $N = 1280$ elements around the ellipse perimeter.

VI. SOLUTION VERIFICATION

The interior solution at $t = 10$ ms is computed using this setup for six levels of mesh refinement, in order to verify convergence of the solution to the analytic result in Equation 3. The error at each level is measured by summing the square of the local deviation of B_2 from the exact solution inside the ellipse, and normalizing by the tally of elements in the ellipse. Taking the square root yields a root-mean-square (RMS) error metric, and normalizing again by the analytic value of B_2 from Equation 3 yields a "fractional error." ALEGRA's transient magnetics methods are formally second-order accurate. However, verification here is done using the magnetic induction B (of most interest to ALEGRA users), rather than the native vector potential A. Therefore, we expect to see first-order convergence of the solution error with respect to the mesh interval.

Applying this technique for body-fitted and regular meshes with approximately 500 to approximately 500,000 elements inside the ellipse, we arrive at the convergence results shown in Fig. 3. We see that ALEGRA computes highly accurate solutions – to one part in 10^5 on the finest meshes. We find smooth, monotonic convergence at a rate of 0.9 for body-fitted meshes, and 1.3 for regular meshes.
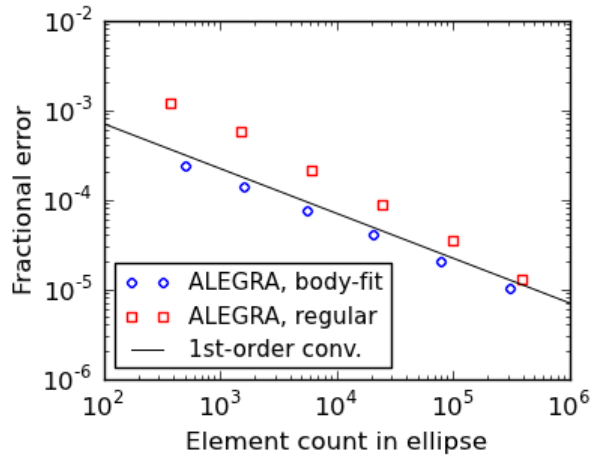
Fig. 3. Convergence of fractional error with respect to analytic solution, showing first order convergence.

VII. CONCLUSIONS

The verification analysis shows that the equilibrium state represented in the analytic solution can be reached with very good accuracy via computation with ALEGRA. The computed solution converges smoothly under mesh refinement at the expected rate, and shows a slight advantage for simple regular meshes over complex body-fitted meshes. This outcome suggests that analysts using tools like ALEGRA for more complex geometries need not avoid using regular meshes, which are much less costly to generate than body-fitted meshes. The closed-form solution provided here makes for convenient verification analysis, and the outcome invites empirical validation by means of laboratory measurement for a similar configuration.

REFERENCES

[1] W. C. Uhlig and C. R. Hummer, "In-flight conductivity and temperature measurements of hypervelocity projectiles," *Procedia Eng.*, vol. 58, pp. 48-57, 2013.

[2] L. D. Landau and E. M. Lifshitz, *Electrodynamics of Continuous Media*, Pergamon, 1984.

[3] J. D. Jackson, *Classical Electrodynamics*, Wiley, 1999.

[4] M. A. Grinfeld, *Thermodynamic Methods in the Theory of Heterogeneous Systems*, Sussex, Longman, 1991.

[5] H. Knoepfel, *Pulsed High Magnetic Fields*, 1st ed., North-Holland, 1970.

[6] H. H. Woodson and J. R. Melcher, *Electro-mechanical Dynamics*, Wiley, 1968.

[7] J. R. Brauer, "Magnetic diffusion times for infusion and effusion in nonlinear steel slabs and cylinders," *IEEE Trans. Mag.*, vol. 42, pp. 3181-3188, 2007.

[8] A. C. Robinson, et al., "ALEGRA: an arbitrary Lagrangian-Eulerian multimaterial, multiphysics code," *Proceedings of the 46th AIAA Aerospace Sciences Meeting*, Reno, Nevada, January 2008.

[9] A. C. Robinson, J. H. J. Niederhaus, V. G. Weirs, and E. Love, "Arbitrary Lagrangian-Eulerian 3D ideal MHD algorithms," *Int. J. Numer. Meth. Fluids*, vol. 65, pp. 1438-1450, 2011.

Far-Field Synthesis of Sparse Arrays with Cross-polar Pattern Reduction

Giulia Buttazzoni and Roberto Vescovo

Department of Engineering and Architecture
University of Trieste, Via A. Valerio 10, Trieste, 34127, Italy
gbuttazzoni@units.it, vescovo@units.it

Abstract — This paper presents a fully deterministic iterative algorithm for the far-field synthesis of antenna arrays with reduction of the cross-polar component. The algorithm synthesizes the excitations as well as the positions of the array elements, providing a sparse geometry. Starting from an initial set of possible positions, the proposed algorithm iteratively solves a sequence of convex optimization problems. At each iteration a suitable objective function is minimized, which allows to reduce the number of radiating elements, among those of the initial set, in presence of constraints on the far-field co-polar and cross-polar patterns. The adopted formulation leads to a second order cone problem (SOCP), which is iteratively solved with CVX, a Matlab-based modeling system developed at the Stanford University and available on the Internet.

Index Terms — Co-polar and cross-polar patterns, far-field synthesis, geometrical synthesis, sparse arrays.

I. INTRODUCTION

Since many decades, antenna arrays became very common in several fields of engineering [1, Ch. 11-13]. Due to the presence of a number of radiating elements, they offer to the designer additional degrees of freedom with respect to a single antenna, thus allowing to meet different tasks.

Initially, the synthesis techniques were analytical and suitable for simple geometries, which were fixed a priori, such as linear [2, 3], rectangular [4] and circular [5, 6] arrays. Subsequently, sophisticated synthesis methods were developed, suitable for arrays of arbitrary geometries, capable of satisfying additional constraints. Some of them are deterministic [7, 8], some others are stochastic [9, 10]. Stochastic methods can solve complicated non-linear optimization problems, but are often costly in terms of computational resources. Thus, when available, the deterministic methods should be preferred.

In recent years, the attention of the array engineers has moved to geometrical synthesis algorithms, which increase the number of the degrees of freedom and, more importantly, allow to reduce the number of elements.

Also in this context, there are deterministic [11] and stochastic procedures [12].

In this paper we present a totally deterministic approach to the geometrical synthesis of antenna arrays of arbitrary geometry, which also allows to control the cross-polar component of the radiation pattern. The paper is organized as follows. In Section II the problem is formulated and the developed algorithm is described. A numerical example is proposed in Section III to prove the effectiveness of the method. Finally, conclusions are summarized in Section IV.

II. METHOD OF SOLUTION

Given an antenna array consisting of N radiating elements, referred to a Cartesian system $O(x, y, z)$, the far-field radiation patterns at the generic direction ϕ of the xy-plane are:

$$F^v(\mathbf{i}, \phi) = \sum_{n=1}^{N} i_n f_n^v(\phi), \qquad (1)$$

where v means "co" or "cr", $\mathbf{i} = [i_1, \dots, i_N]^T$ is the complex column vector of the excitations, $f_n^{co}(\phi)$ and $f_n^{cr}(\phi)$ are, respectively, the co-polar and cross-polar far-field patterns of the n-th array element.

Given a desired far-field co-polar pattern $F_d(\phi)$, which identifies a main beam region MB and a side lobe region SL, the far-field constraints on the co-polar component can be written as:

$$\begin{cases} |F^{co}(\mathbf{i}, \phi) - F_d(\phi)| \leq \epsilon & if \ \phi \in MB \\ |F^{co}(\mathbf{i}, \phi)| \leq \rho^{co}(\phi) & if \ \phi \in SL \end{cases}, \qquad (2)$$

where $\rho^{co}(\phi)$ is a real positive function specifying the maximum allowed side lobe level. Analogously, the far-field cross-polar constraint can be written as:

$$|F^{cr}(\mathbf{i}, \phi)| \leq \rho^{cr}(\phi), \qquad (3)$$

where $\rho^{cr}(\phi)$ is a real positive function specifying the maximum allowed cross-polar far-field level.

The synthesis process that we propose consists in: (a) introducing a very dense grid of elements; (b) iteratively determining the excitations of these elements, while satisfying constraints (2) and (3); (c) finally removing those elements that have excitations lower than a given threshold. The last step yields the required sparse array, consisting of a strongly reduced number of elements. In other words, the synthesized excitations and

positions of the array elements are those of the "surviving" elements.

The method of solution that we are presenting is an evolution of that proposed in [13]. Precisely, Equations (2) and (3) are regarded as the constraints of an optimization problem aimed at reducing (and possibly minimizing) the number of radiating elements. In order to exploit techniques that solve convex optimization problems, an iterative procedure is proposed which, at the k-th iteration, solves the following weighted norm-1 minimization problem:

$$\min_{\mathbf{i}^k} \sum_{n=1}^{N} \alpha_n^k \left| i_n^k \right| \quad \text{subject to (2) and (3),} \quad (4)$$

where $\mathbf{i}^k = [i_1^k, \dots, i_N^k]^T$, and the weights α_n^k are given by:

$$\alpha_n^k = \left(\left| i_n^{k-1} \right| + \epsilon \right)^{-1}, \quad (5)$$

where the parameter $\epsilon > 0$ is to be chosen slightly smaller than the smallest non-zero excitation amplitude that one is willing to implement [14]. All the array elements with an amplitude $\left| i_n^k \right| \leq \epsilon$ are switched-off, and contribute to the evaluation of $\left\| \mathbf{i}^k \right\|_0$, which is defined as the number of zero-components of vector $\mathbf{i}^k$. With reference to (5), note that a zero excitation at the step k, $i_n^k = 0$, might result in a non-zero excitation at the successive step $k + 1$, $i_n^{k+1} \neq 0$. The iterative process is stopped when the number of zero elements does not change in three consecutive iterations. The optimality of the solution is not guaranteed, but numerical examples proved the improvements that can be obtained with respect to usual fixed-grid synthesis algorithms.

The proposed synthesis procedure can be summarized as follows:
1. Define a regular array structure, which will be regarded as the reference array.
2. Make thicker the initial grid to obtain an array with the same geometry but an increased number of possible positions.
3. Choose the parameter ϵ and set $k = 1$.
4. Solve the fixed-grid far-field co-polar synthesis problem described by constraints (2) with one of the algorithms available in the literature: we used the algorithm in [15].
5. Set $k := k + 1$ and evaluate the weights α_n^k by (5).
6. Solve the problem in (4).
7. If $k > 2$ and $\left\| \mathbf{i}^{k-2} \right\|_0 = \left\| \mathbf{i}^{k-1} \right\|_0 = \left\| \mathbf{i}^k \right\|_0$ stop the procedure and consider the vector $\mathbf{i}^k$ as the solution to the problem; else go back to step 5.

In particular, note that the synthesized sparse array consists of only those elements for which $\left| i_n^k \right| > \epsilon$. The step 7 gives the excitations $\mathbf{i}^k$ of such elements. In the following section, a numerical example shows the effectiveness of the proposed algorithm.

III. NUMERICAL RESULTS

Starting from the example in [16], we here propose a numerical example that shows the improvements that can be achieved with the presented algorithm in terms of reduction of the number of radiating elements. Note that, constraints on the cross-polar far-field pattern were not considered in [16]. The array used in [16] is shown in Fig. 1 (a) (blue circles). It consists of $N = 54$ radially oriented equally spaced Huygens radiators with the electrical dipoles parallel to the z-axis. The co-polar pattern was defined as the ϑ-component of the electric far-field on the xy-plane ($\vartheta = \pi/2$). The ϕ-components of the electric far-field on the xy-plane were negligible with the electrical dipoles parallel to the z-axis. So, the electrical dipoles were $\pi/20$ radians tilted with respect to the z-axis. This is regarded as the reference array.

As a first step, the method in [16] has been used to solve the far-field co-polar synthesis problem. The synthesized co-polar pattern and the corresponding cross-polar pattern are depicted in Fig. 1 (b).

In order to implement the iterative procedure above described, firstly the inter-element spacing between adjacent elements on the reference array was reduced by a factor 5, leading to a thicker grid of $N = 270$ possible positions. Then, with reference to constraint (2), in the MB region the pattern synthesized with [16] was chosen as the desired far-field pattern $F_d(\phi)$, whereas in the SL region the upper bound of the mask (red line in Fig. 1 (b)) was chosen as the function $\rho^{co}(\phi)$. The function $\rho^{cr}(\phi)$ in (3) was chosen in such a way as to impose a maximum value of -20 dB for the cross-polar component.

According to [13], we set $\epsilon = 10^{-2}$ in (5). Finally, at each step the optimization problem in (4) was solved using [17] in a Matlab code on a laptop with 8GB RAM. The iterative procedure stopped after 5 iterations and required only 217 seconds to give the results. The synthesized sparse array is shown in Fig. 1 (a) (red triangles). It consisted of only 39 elements among the possible 270 elements. Thus, a reduction of 27,8% of radiating elements with respect to the 54 elements of the reference array was achieved. The far-field co-polar and cross-polar patterns resulted to satisfy both constraints (2) and (3) with great accuracy, as is shown in Fig. 1 (c).

Then, we imposed a more stringent requirement on the cross-polar component. Precisely, we chose $\rho^{cr}(\phi)$ in such a way as to obtain, with respect to the co-polar component, reductions of 20 dB in the MB region and 10 dB in the SL region. Also in this case, the proposed method gave patterns satisfying constraints (2) and (3) with very good accuracy (Fig. 1 (d)). The synthesized array consisted of 50 elements ($N_1 = 19$, $N_2 = 31$, reduction of 7.4%). The algorithm required 7 iterations, performed in 373 seconds. The results, in terms of element positions and excitations, are detailed in Table 1.
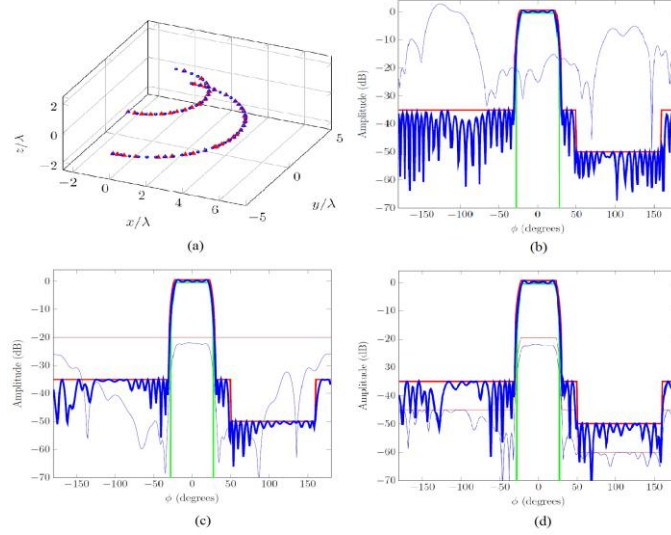
Fig. 1. (a): Geometry of the arrays. Blue circles: elements of the reference array ($N_1 = 20, R_1 = 2.8\lambda, z_1 = \lambda$; $N_2 = 34$, $R_2 = 4.6\lambda, z_2 = -\lambda$). Red triangles: elements of the synthesized sparse array, consisting of $N = 39$ elements ($N_1 = 14$, $N_2 = 25$, the radii and the z coordinates are as in the reference array). Patterns synthesized with: (b) the method in [16]; (c): the presented method, first example; (d): the presented method, second example. Thick lines: co-polar pattern (blue), upper (red) and lower (green) bounds of the mask. Thin lines: cross-polar pattern (blue) and the function $\rho^{cr}(\phi)$ (red).

Table 1: The results obtained with the proposed approach; positions (φ_n) and excitations (i_n) of the array elements (Angles in degrees. The radii and the z coordinates of the elements can be deduced from the above text.)

	First Example			Second Example				First Example			Second Example		
n	φ_n	$\lvert i_n\rvert$	$\angle i_n$	φ_n	$\lvert i_n\rvert$	$\angle i_n$	n	φ_n	$\lvert i_n\rvert$	$\angle i_n$	φ_n	$\lvert i_n\rvert$	$\angle i_n$
1	-57.27	0.44	-154.66	-90.00	0.11	-19.08	26	-1.60	0.59	111.51	-52.72	0.38	-109.61
2	-48.18	0.50	134.86	-82.73	0.19	-141.98	27	-0.53	0.80	76.60	-44.20	0.37	-141.40
3	-35.45	0.70	28.68	-75.45	0.27	96.96	28	4.79	0.86	91.88	-38.88	0.51	134.37
4	-33.64	0.51	93.37	-66.36	0.11	-2.56	29	33.55	0.24	145.39	-30.35	0.68	123.16
5	-24.54	1.84	4.68	-55.45	0.24	-113.26	30	37.81	0.26	139.26	-22.90	0.34	131.91
6	-11.82	2.17	7.23	-46.36	0.23	129.79	31	41.01	0.37	-172.91	-21.83	0.47	106.97
7	-0.91	2.99	17.22	-39.09	0.31	52.63	32	47.40	0.17	-88.67	-16.51	0.83	77.43
8	10.00	2.62	10.61	-30.00	0.43	40.02	33	53.79	0.30	-41.23	-10.12	1.01	94.74
9	22.73	2.14	-2.30	-20.91	1.10	-11.04	34	60.18	0.18	89.01	-4.79	0.22	139.52
10	33.64	0.60	62.34	-10.00	1.05	19.40	35	64.44	0.25	161.08	-3.73	0.93	104.07
11	35.45	0.52	44.09	-8.18	0.94	-31.85	36	74.02	0.14	-21.75	0.53	1.58	104.45
12	44.54	0.40	140.56	2.73	1.89	29.04	37	80.41	0.08	127.73	6.92	1.69	95.17
13	59.09	0.20	-128.33	4.55	0.64	-47.67	38	84.67	0.09	-142.48	14.38	0.95	81.94
14	88.18	0.02	-91.61	15.45	1.45	6.19	39	90.00	0.09	54.98	20.77	0.49	116.59
15	-90.00	0.11	40.87	22.73	0.65	-48.08	40				28.22	0.50	120.56
16	-86.80	0.12	-93.77	33.64	0.88	47.17	41				29.29	0.16	136.32
17	-74.02	0.17	-16.44	42.73	0.35	134.61	42				35.68	0.67	112.26
18	-62.31	0.29	132.79	55.45	0.30	-118.80	43				39.94	0.34	170.10
19	-59.11	0.35	55.64	80.91	0.13	144.31	44				46.33	0.16	-107.80
20	-45.27	0.25	-124.39	-90.00	0.09	76.53	45				51.66	.40	-79.79
21	-41.01	0.12	-176.46	-86.80	0.16	-78.17	46				62.31	0.36	120.16
22	-37.81	0.16	155.68	-82.54	0.10	148.19	47				72.96	0.15	-21.74
23	-20.77	0.25	111.72	-75.09	0.12	45.20	48				80.41	0.17	101.64
24	-16.51	0.25	72.79	-61.24	0.10	109.42	49				83.61	0.06	-129.23
25	-6.92	0.47	94.09	-56.98	0.32	-3.43	50				87.87	0.10	21.88

IV. CONCLUSIONS

The algorithm proposed in this paper is a fully deterministic iterative procedure able to synthesize sparse arrays of quite arbitrary shapes, including conformal ones. Along with the positions of the elements, the iterative procedure yields their excitations in such a way that a desired far-field co-polar pattern is approximated and the far-field cross-polar pattern does not exceed a prescribed threshold.

The optimality of the solution is not guaranteed, but a numerical example is provided that shows the effectiveness of the presented procedure.

At the knowledge of these authors, the literature does not offer deterministic techniques capable of solving the synthesis problem at hand, for arrays of arbitrary geometry and with the considered constraints.

REFERENCES

[1]   C. A. Balanis, *Modern Antenna Handbook*, John Wiley and Sons, 2008.

[2]   A. D. Bresler, "A new algorithm for calculating the current distribution of Dolph-Chebyshev arrays," *Antennas and Propagation, IEEE Transactions on*, vol. 28, pp. 951-952, Nov. 1980.

[3]   A. T. Villeneuve, "Taylor patterns for dicrete arrays," *Antennas and Propagation, IEEE Transactions on*, vol. 32, pp. 1089-1093, Oct. 1984.

[4]   S. W. Autrey, "Approximate synthesis of non-separable design responses for rectangular arrays," *Antennas and Propagation, IEEE Transactions on*, vol. 35, pp. 907-912, Aug. 1987.

[5]   R. Vescovo, "Constrained and unconstrained synthesis of array factor for circular arrays," *Antennas and Propagation, IEEE Transactions on*, vol. 43, no. 12, pp. 1405-1410, Dec. 1995.

[6]   T. T. Taylor, "Design of circular apertures for narrow beamwidths and low side lobes," *Trans. IRE*, vol. 8, pp. 17-22, Jan. 1960.

[7]   G. Buttazzoni and R. Vescovo, "An efficient and versatile technique for the synthesis of 3D copolar and crosspolar patterns of phase-only reconfigurable conformal arrays with DRR and near-field control," *Antennas and Propagation, IEEE Transactions on*, vol. 62, no. 4, pp. 1640-1651, Apr. 2014.

[8]   L. I. Vaskelainen, "Constrained least-squares optimization in conformal array antenna synthesis," *Antennas and Propagation, IEEE Transactions on*, vol. 55, no. 3, pp. 859-867, Mar. 2007.

[9]   G. Buttazzoni and R. Vescovo, "Deterministic and stochastic approach to the synthesis of conformal arrays for SAR applications," *Electromagnetics in Advanced Applications (ICEAA), 2013 International Conference on*, pp. 520-523, Sept. 9-13, 2013.

[10] J. M. Johnson and Y. Rahmat-Samii, "Genetic algorithms in electromagnetics," *IEEE Antennas Propag. Magazine*, vol. 39, pp. 7-21, Aug. 1997.

[11] J. L. Araque Quijano, M. Righero, and G. Vecchi, "Sparse 2-D array placement for arbitrary pattern mask and with excitation constraints: a simple deterministic approach," *Antennas and Propagation, IEEE Transactions on*, vol. 62, no. 4, pp. 1652-1662, Apr. 2014.

[12] V. Murino, A. Trucco, and C. S. Regazzoni, "Synthesis of unequally spaced arrays by simulated annealing," *Signal Processing, IEEE Transactions on*, vol. 44, no. 1, pp. 119-122, Jan. 1996.

[13] B. Fuchs, "Synthesis of sparse arrays with focused or shaped beampattern via sequential convex optimizations," *Antennas and Propagation, IEEE Transactions on*, vol. 60, no. 7, pp. 3499-3503, Jul. 2012.

[14] E. J. Candés, M. B. Wakin, and S. P. Boyd, "Enhancing sparsity by reweighted l_1 minimization," *J. Fourier Analy. Appl.*, vol. 14, pp. 877-905, Dec. 2008.

[15] G. Buttazzoni and R. Vescovo, "Synthesis of co-polar and cross-polar patterns with dynamic range ratio reduction for phase-only reconfigurable arrays," *Antennas and Propagation (EUCAP), 2012 6th European Conference on*, pp. 2623-2627, Mar. 26-30, 2012.

[16] R. Vescovo, "Power pattern synthesis for antenna arrays with null constraints in the near-field region," *Microwave and Optical Technology Letters*, vol. 44, no. 6, pp. 542-545, Mar. 2005.

[17] CVX, [Online]. Available at: http://cvxr.com/cvx/download/

Compact Shaped Antennas for Wide-Band Radiogoniometry

Antonio Manna [1], Giuseppe Pelosi [2], Monica Righini [2], Luca Scorrano [1], Stefano Selleri [2], and Fabrizio Trotta [1]

[1] Elettronica S.p.A.
Via Tiburtina Km. 13.700, Rome, Italy
[antonio.manna, luca.scorrano, fabrizio.trotta]@elt.it

[2] Department of Information Engineering
University of Florence, Via di S. Marta 3, Florence, Italy
[giuseppe.pelosi, monica.righini, stefano.selleri]@unifi.it

Abstract — In this paper, a wide band monopole antenna with a shaped profile is presented. Shaped profile and end-caps allow for a compact antenna with respect to wavelength. Antenna is designed to be as isotropic as possible and with low phase deviation from spherical wave front to allow accurate detection of the direction of arrival of an unknown signal when used in radiogoniometry applications.

Index Terms — Antennas, shaped monopole, radiogoniometry, wide-band antennas.

I. INTRODUCTION

As part of the safety-related control of the territory, it is important to locate vehicles, aircraft or vessels not only actively, using surveillance radars, but also passively, on the basis of the electromagnetic emissions, intentional or not, of the target. This second system, or passive radar, detects the direction of the origin of the signal emitted by the target or emitted by an unrelated source and scattered by the target itself like a radio or television broadcasting station [1-3]. Of course, if more than one system is deployed, by integrating the data from each system, a 3D localization of the target is possible. Being the system fully passive, only a receiving chain is necessary and complexity, size and power consumption are much reduced with respect to an active radar.

On the other hand, while the antenna of an active radar must be highly directive and can be relatively narrow banded, the antenna of a passive detector must be necessarily as omnidirectional as possible and must cover the largest possible bandwidth, since it is not known a priori neither the position nor the emission spectrum of the target; direction of arrival of the signal being computed by comparing the delays with which signal is received from two or more antennas of the single system [1-3].

Broad band antennas are usually bulky and large, the dimension being comparable to the wavelength of the lowest working frequency. If a system is to be at the same time efficient but compact and possibly having a reduced impact on landscape, antenna must be conveniently miniaturized.

In this context, an electrically small antenna (ESA) is an antenna whose maximum dimension is less than $\lambda/2\pi$ (radianlength) [4,5]. Small antennas fitting this definition radiate the first order spherical modes of a Hertzian dipole and hence, are quite close to omnidirectional. Yet the main issue of an ESA is the presence of a strong reactive behavior in its input impedance which severely impairs radiation characteristics and band. Several techniques exist to solve this issue: it is possible to load the antenna with lumped elements or metamaterials inspired elements [6-9], alternatively, the electrical path of the currents can be made longer by folding conductors or applying appropriate sinuous shapes [10-14].

In this contribution the second technique is applied, and a printed monopole with a fractal-like profile designed. A shaped end cap is also added to further lengthen the current path without making the antenna too high. Particular attention has been given to the phase of antenna pattern in azimuth, since phase fluctuations directly reflect on direction finding errors. Being the antennas to be placed around a circle, with varying orientation, phase uniformity in azimuth is a key point in this application. The proposed design has then been realized and measured.

The paper is organized as follows. Section II presents the antenna design. Section III reports the comparison between simulations and measurements results. Finally, Section IV draws some conclusions.

II. ANTENNA DESIGN

The aim of this project has been the design,

optimization and realization of a high performance small antenna for direction finding applications.

The element presented in this paper is a monopole antenna placed over a circular ground plane, working in the frequency range 600 MHz – 3 GHz. The key feature of the monopole is keeping a small size even if it operates in a wide band, about 2.3 octaves (Fig. 1). Although the present paper concentrates on a single element, an array of such elements placed along a circumference on a conducting disk is the final goal.
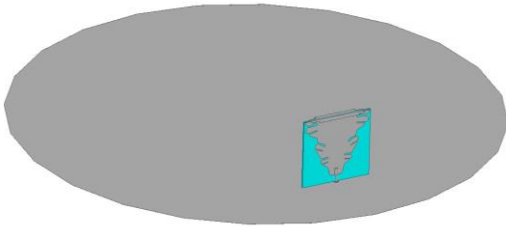

Fig. 1. Monopole antenna over a circular ground plane. Plane diameter is 300 mm, the antenna is placed at 125 mm from the disk center.

The element has been designed starting from a standard Bow-Tie Antenna (BTA), which has been modified improving its geometry with fractal based contour shaping. Furthermore, a fractal based contour shaping plate has been added at the end of the structure. These modifications allowed to extend the electric path of the currents achieving a better behavior in the lower-band of the antenna, without a significant increasing in its sizes.

The antenna shape derives from a spline base element whose shape is governed by 10 control points (Fig. 2), which is iterated and, at each iteration, rotated by $\alpha = -30°$ on odd iterations, by $\alpha = 30°$ on even ones, and scaled by a $k = 0.2$ scaling factor [15]. Dimensions, control points positions, and number of repetitions have been numerically optimized via genetic algorithms [16], so as to minimize the reflection loss, attaining the profile in Figs. 3, 4.

Miniaturization is also achieved via end-caps which, extending the antenna in the third dimension, allows for a better filling of Chu's sphere. End-caps are themselves realized with a sinuous contour devised, again, to allow extended paths for currents.

The monopole is fed by a 50 Ω coaxial cable passing through the aluminum ground whose probe is directly connected on the antenna surface. The element is printed over a DE104 ($\varepsilon_r = 4.46$ @ 100 MHz, $\tan\delta = 0.023$ @ 2 GHz) substrate 1.6 mm thick and covered with a 0.0018 mm thick copper metallization. The whole antenna spans a box 56x10x50 mm^3, considering the 10 mm wide end-cap (Figs. 3, 4).

The behavior of antenna has been simulated numerically in the shape optimization phase of the design. To have a most realistic simulation both the finite aluminum ground and the coaxial cable connector were considered in the numerical model.
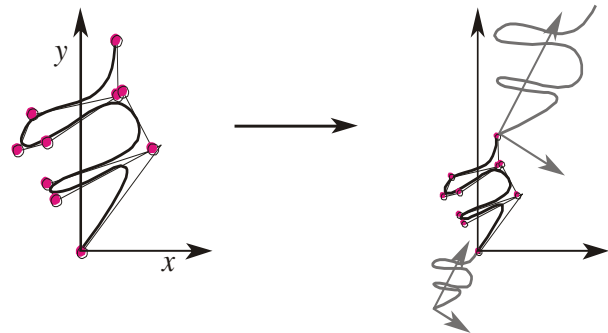

Fig. 2. Profile primitive (spline control points in purple) and profile generation by scaled replication.
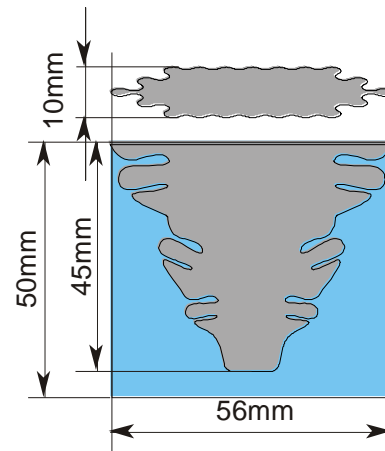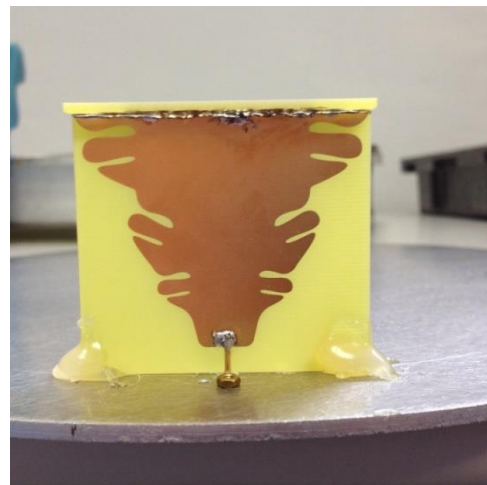

Fig. 3. Antenna basic layout and dimensions.

Fig. 4. Prototype of the monopole antenna

III. MEASUREMENT RESULTS

The realized prototype is shown in Fig. 4 and the results of its measurements have been compared to simulations.

Figure 5 presents the comparison between simulations and measures for S_{11}, an excellent agreement is shown. Hatched rectangle shows requirements. An $|S_{11}|<-5$ dB is considered acceptable. Requirements are relaxed in comparison to standard ones, but key point in the application is band, not matching.

Measures were carried out in the University of Florence semi-anechoic chamber, which is 3500 mm x 4900 mm x 3000 mm, with anechoic multilayer wideband absorbers Eccosorb An-79, made of polyurethane foam loaded with graphite featuring an optimized conductance profile, for a reflection coefficient amplitude of at least -17 dB.

Signal generator is an Agilent Technologies E4438C, capable of sweeping from 250 kHz to 6 GHz, with -136 dBm to 25 dBm output. For the receiving side, the Agilent (Hp) 8596E spectrum analyzer was used, capable of spanning 100 kHz - 12.8 GHz in AC with a resolution bandwidth from 1 kHz to 3 MHz.

Measurements were made exploiting two identical realization of the proposed antenna, one transmitting and one receiving.

Figure 6 shows experimental results for the phase of the received signal as a function of frequency and for two values of the elevation angle. Phase is given as an average over the azimuth angle. Error bars at $\pm 2\sigma$ with respect to average, σ being the standard deviation, shows the limits within which 95% of the phase values fall. As it can be seen phase variation along azimuth is very limited. This being the most relevant aspect in accurate radiogoniometry. Gain patterns are nearly omnidirectional, with a variance of less than 1.8 dB over the whole azimuth angle, and are not reported for brevity. This is due to the ground plane, being the antenna placed next to the border, which deteriorates the pattern symmetry. System specifications allowed for a maximum variance of 2 dB, hence results satisfy them. Finally, Fig. 7 shows simulated and measured gain for the proposed monopole, while Fig. 8 shows the realized gain at centerband; good isotropy can be observed on azimuth. It must be noted that simulations concerned the dipole plus the finite ground disk in free space, while measurements were carried out in the semi-anechoic chamber at the University of Florence, hence fluctuations in the measured gain are due to multipath. It is anyway important to note that such fluctuations are very close to simulations results, as the best fit dotted line in Fig. 7 shows.
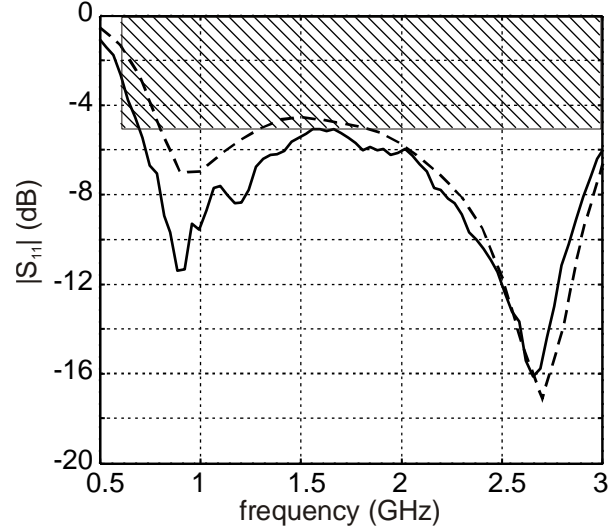

Fig. 5. |S11| for the monopole antenna. The figure shows the comparison between simulation result (dashed line) and measured result (solid line).
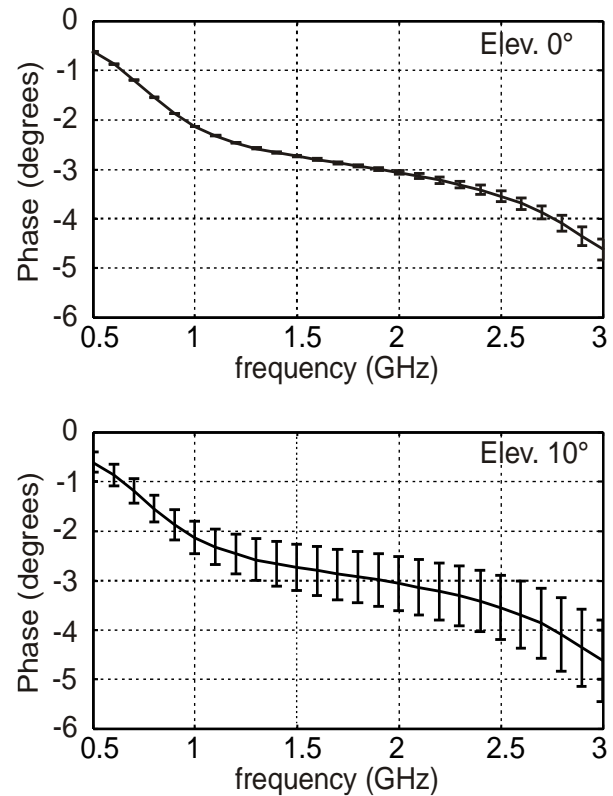

Fig. 6. Average and standard deviation of the received signal phase over azimuth, for elevation equal to 0 (top) and 10° (bottom).
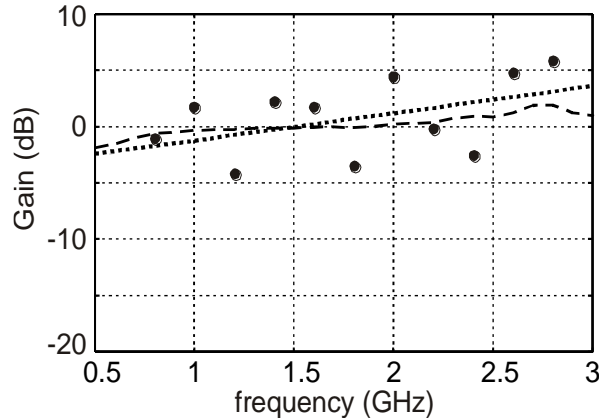
Fig. 7. Simulated (dashed line) and measured (bullets) gain for the proposed antenna. Dotted line represents a first order polynomial best fit on the measured gain.
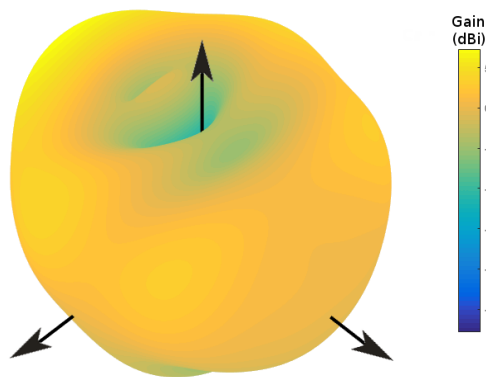

Fig. 8. Simulated realized gain for the proposed antenna.

VI. CONCLUSION

Preliminary results for a compact UWB monopole antenna for radiogoniometry have been presented, measured data fit well with simulations and prove the effectiveness of the proposed fractal-based design.

REFERENCES

[1] P. E. Howland, D. Maksimiuk, and G. Reitsma, "FM radio based bistatic radar," *IEE Proc., Radar Sonar Navig.*, vol. 152, pp. 107-115, 2005.

[2] P. E. Howland, "Target tracking using television-based bistatic radar," *IEE Proc., Radar Sonar Navig.*, vol. 146, pp. 166-174, 1999.

[3] A. Farina, P. Gallina, L. Lucci, R. Mancinelli, G. Pelosi, and S. Selleri, "Back lobe minimization for a VHF LPDA-based interferometer," *11th Int. Symp. Microwave Optical Techn. (ISMOT-2007)*, Monte Porzio Catone – Roma (Italy), pp. 195-198, Dec. 17-21, 2007.

[4] H. A. Wheeler, "Fundamental limitations of small antennas," *Proc. IRE*, vol. 35, pp. 1479-1484, 1947.

[5] R. C. Hansen, "Fundamental limitations in antennas," *Proc. IEEE*, vol. 69, pp. 170-182, 1981.

[6] R. W. Ziolkowski and A. D. Kipple, "Application of double negative materials to increase the power radiated by electrically small antennas," *IEEE Trans. Antennas Propagat.*, vol. 51, pp. 2626-2640, 2003.

[7] R. W. Ziolkowski and A. Erentok, "At and below the Chu limit: passive and active broad bandwidth metamaterial-based electrically small antennas," *IET Microwaves, Antennas Propagat.*, vol. 1, no. 1, pp. 116-128, 2007.

[8] A. Erentok and R. W. Ziolkowski, "Metamaterial-inspired efficient electrically small antennas," *IEEE Trans. Antennas Propagat.*, vol. 56, pp. 691-707, 2008.

[9] P. Jin and R. W. Ziolkowski, "Broadband, efficient, electrically small metamaterial-inspired antennas facilitated by active near-field resonant parasitic elements," *IEEE Trans. Antennas Propagat.*, vol. 58, pp. 318-327, 2010.

[10] S. Tanaka, et al., "Miniaturised wideband folded bow-tie antenna," *Electronics Letters*, vol. 45, pp. 295-297, 2009.

[11] K. L. Shlager, G. S. Smith, and J. G. Maloney, "Optimization of bow-tie antennas for pulse radiation," *IEEE Trans. Antennas Propagat.*, vol. 42, pp. 975-982, 1994.

[12] C. Cho, I. Park, and H. Choo, "Design of a small antenna for wideband mobile direction finding systems," *IET Microwaves, Antennas Propagat*, vol. 4, pp. 930-937, 2010.

[13] D. H. Werner and S. Ganguly, "An overview of fractal antenna engineering research," *IEEE Antennas Propagat. Mag*., vol. 45, pp. 38-57, 2003.

[14] J. P. Gianvittorio and Y. Rahmat-Samii, "Fractal antennas: a novel antenna miniaturization technique, and applications," *IEEE Antennas Propagat. Mag*., vol. 44, pp. 20-36, 2002.

[15] Y. Liu, S. Yoon, J. R. DeLuis. F. D. Flaviis, and N. G. Alexopoulos, "Polya elements with application to antennas, thin absorbers and filters," *IEEE Trans. Antenna Propagat.*, vol. 60, pp. 5092-5099, Nov. 2012.

[16] E. Agastra, G. Pelosi, S. Selleri, and R. Taddei, *Multiobjective Optimization Techniques*, in The Wiley Encyclopedia of Electrical and Electronics Engineering, John Wiley & Sons, New York (NY), pp. 1-29, 2014. ISBN 978-0-471-34608-1.

RCS Results for an Electrically Large Realistic Model Airframe

**Ciara Pienaar [1], Johann W. Odendaal [1], Johan C. Smit [2],
Johan Joubert [1], and Jacques E. Cilliers [2]**

[1] Department of Electrical Electronic and Computer Engineering
University of Pretoria, Pretoria, South Africa
u11175070@tuks.co.za, wimpie@up.ac.za, jjoubert@up.ac.za

[2] Defence Peace Safety and Security
Council for Scientific and Industrial Research, Pretoria, South Africa
jcsmit@csir.co.za, jcilliers@csir.co.za

Abstract ─ The accuracy with which MLFMM, PO and PO with SBR can calculate the RCS of a realistic electrically large model airframe is investigated. The target has a maximum electrical length of 106λ. An accurate 3D numerical model of the target was created using a laser scanner. The numerical results are validated against data measured in a compact range.

Index Terms ─ Method of moments, other asymptotic methods, RCS measurements, scattering/RCS.

I. INTRODUCTION

Validated radar cross section (RCS) data is required for various radar and electronic warfare (EW) applications, viz. detection studies and the development and testing of non-cooperative target recognition (NCTR) techniques. A number of studies have compared measured and simulated RCS of canonical structures or targets constructed of simple canonical structures. A few RCS benchmarking targets have been defined in [1], but almost all of these structures are either electrically simple and/or small. Recently a study compared the measured and simulated data of a relatively electrically large Boeing 777 scale model. This model had a total length of 21λ. A commercially available computer aided design (CAD) model of the Boeing 777 was used with the CADRCS software package, which implements physical optics (PO) combined with ray-tracing and shadowing to calculate the RCS [2]. In [3], three different electrically large targets were analyzed. The computational electromagnetic (CEM) methods that were compared included the multilevel fast multipole method (MLFMM) and PO with shooting and bouncing rays (SBR). The three targets that were analyzed included a trihedral corner reflector, a generic cruise missile and a Cessna 172 model. Only simulated results were considered with MLFMM results used as a reference.

This paper considers the RCS of a realistic 1:25 scale model of a Boeing 707. The model is electrically large with a maximum electrical length of 106λ. The scale model is constructed from thin-walled aluminium. Instead of representing the target as a composition of simple canonical structures or using a commercially available CAD model, a very accurate 3D CAD model was created by laser scanning the scale model. Different CEM methods were used to calculate the RCS of the airframe, using three software packages, viz. MLFMM using FEKO and CST, PO using FEKO, and PO with SBR using SigmaHat (developed by CSIR DPSS, South Africa). The calculated data are validated against RCS data measured in a compact range at the University of Pretoria, South Africa.

II. EXPERIMANTAL SETUP

The VV-polarized monostatic RCS of the model was measured in the compact range (Fig. 1) as a function of frequency and azimuth angle (-180º to 180º) with a typical accuracy of 0.2 dB. The angular increments were 0.2º.

Simulations were performed in the three packages, utilizing different CEM methods, to calculate the VV-polarized monostatic RCS of the target. All the simulations were performed at 10 GHz and 17 GHz over azimuth (0º to 180º) in 0.2º steps, at 0º elevation.

Fig. 1. Boeing 707 scale model in the compact range and laser scanned 3D CAD model in FEKO.

The 3D CAD model used for the simulations is also shown in Fig. 1. The laser scanning was conducted at CSIR Technology for Special Operations (TSO) with

a hand scanner which generated a 3D point cloud of the model. This point cloud was converted to a mesh model using 3D processing software. The mesh model was imported into FEKO and a simulation mesh was created. The scanned model has an average accuracy of better than 0.2 mm relative to the actual scale model.

FEKO and CST simulations were performed using the MLFMM solver with the combined field integral equation option to increase the computational speed of the simulations [4, 5]. The model was discretized with a mesh size of $\lambda/10$ at 10 GHz, resulting in 570,236 and 570,196 mesh triangles in FEKO and CST, respectively. The full-wave and asymptotic methods compared to the measured data at 10 GHz are provided in Fig. 2 and Fig. 3, respectively. The 17 GHz data is provided in Fig. 4 and Fig. 5, respectively.

III. METRICS AND PERFORMANCE

In general, the results show good agreement between the overall shape of the measured and simulated data over the entire azimuth range for all four CEM techniques considered. The two asymptotic techniques differ from the measured data over small angular regions, where the RCS values are low. There are some distinct characteristic returns in the angular RCS response, the first being at port side broadside, between 89º to 91º (10 GHz) and 89.4º to 91.8º (17 GHz), when the fuselage of the aircraft is perpendicular to the incident field. Here, the RCS values are the largest and have narrow beam-widths. The second characteristic return is the flash produced by the leading edge of the port side wing, between 38º to 41.2º (10 GHz) and 38.2º to 40.4º (17 GHz).

A. Accuracy metrics

The critical ranges in the accuracy analysis were chosen to be the azimuth ranges which included the characteristic returns, namely the broadside return and wing flash. Four accuracy metrics were defined to compare the measured and simulated RCS results, and to quantify the accuracy of the various methods.

The first metric is the difference between the measured and simulated peak RCS values, in the critical azimuth ranges. The absolute values of the deep nulls were disregarded as they may have led to misleadingly large RCS differences. These large differences could be due to the miss sampling of nulls or slight misalignment between the geometrical shape of the physical and numerical models. The second metric is the azimuth angle ranges, in the critical regions, over which the difference between the measured and simulated RCS remained less than 5 dB. The angular accuracy of the side lobes near the characteristic returns is chosen as the third metric. The fourth metric is the peak RCS differences and the side lobe accuracies of the methods over an azimuth range

where the RCS values are lower (i.e., below -5 dBsm). This range is chosen from 41.2º to 60º for the 10 GHz data and 40.4º to 64º for the 17 GHz data, and will be referred to as the lower RCS range.

Expanded views of the angular ranges surrounding the port broadside and wing flash of the 17 GHz data are provided for easier visual comparison in Fig. 6 and Fig. 7. Figure 7 also includes an expanded view of the lower RCS azimuth range from 40.4º to 64º.

B. Numerical performance

A summary of the evaluated accuracy metrics for all four methods at 10 GHz is provided in Table 1.

MLFMM (FEKO) results at 17 GHz of the broadside return are accurate to within 5 dB and the wing flash to within 4.0 dB. The azimuth ranges over which the simulated RCS remains within 5 dB of the measured RCS is 43.6º and 29.4º, respectively. The angular accuracy of the side lobes near the characteristic returns are 0.2º and 0.4º, respectively. This method's RCS results are accurate over 40.4º to 64º (the lower RCS range). Here, the maximum difference between the calculated and measured data is 7.3 dB and the side lobes are accurate to within 0.4º.

The MLFMM (CST) results at 17 GHz of the broadside return are accurate to within 5 dB and the wing flash to within 4.2 dB. The azimuth ranges over which the simulated RCS remains within 5 dB of the measured RCS is 44.8º and 30.4º, respectively. The angular accuracy of the side lobes near the characteristic returns are 0.2º and 0.4º, respectively. This method's RCS results are accurate over the lower RCS range. Here, the maximum difference between the calculated and measured RCS data is 8.0 dB and the side lobes are accurate to within 0.4º.

With PO (FEKO) at 17 GHz some ranges are slightly inaccurate, but there is overall good agreement at the characteristic returns. The broadside return and wing flash is accurate to within 2.5 dB and 3.5 dB, respectively. The azimuth range over which the simulated RCS remains within 5 dB of the measured RCS is 29.8º and only 8º, respectively. The angular accuracy of the side lobes near the characteristic returns is 0.2º. The maximum RCS difference in the lower RCS range is 11.7 dB and there is almost no correlation between the simulated PO and measured side lobes in this range. Larger errors are produced by the PO method, between 43.4º and 59.6º compared to the MLFMM method.

PO with SBR (SigmaHat) results for the broadside return and wing flash are accurate to within 3.3 dB and 3.7 dB, respectively at 17 GHz. The azimuth ranges over which the simulated RCS remains within 5 dB of the measured RCS is 24.8º and only 9.6º, respectively. The angular accuracy of the side lobes near the characteristic returns is 0.2º. The maximum difference

in the lower RCS range is 10.1 dB and although the RCS trends are similar in this azimuth region, there is almost no correlation between the simulated PO with SBR and measured side lobes. This method produced larger errors between 43.4° and 59.6° compared to the MLFMM method.

A summary of the evaluated accuracy metrics for all four methods at 17 GHz is provided in Table 2. Key specifications of the computers that were used for the simulations, as well as the computing resources required by each method, are summarized in Table 3.

Fig. 2. RCS measured at 10 GHz compared to RCS calculated with MLFMM in FEKO and in CST.

Fig. 5. RCS measured at 17 GHz compared to RCS simulated via PO in FEKO; PO with SBR in SigmaHat.

Fig. 3. RCS measured at 10 GHz compared to RCS simulated via PO in FEKO; PO with SBR in SigmaHat.

Fig. 6. RCS measured and simulated with the different methods, at 17 GHz for the port side broadside.
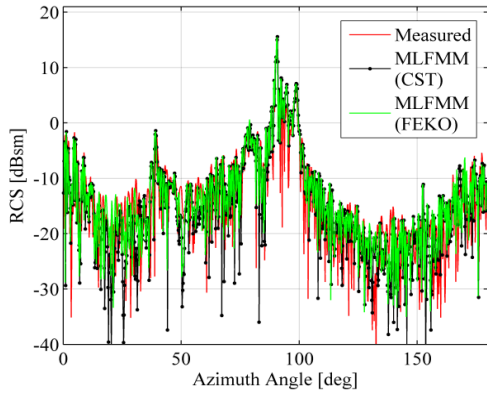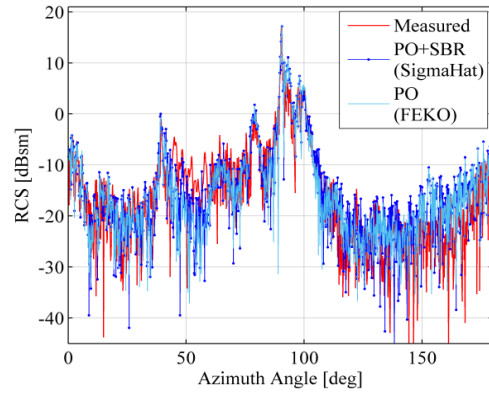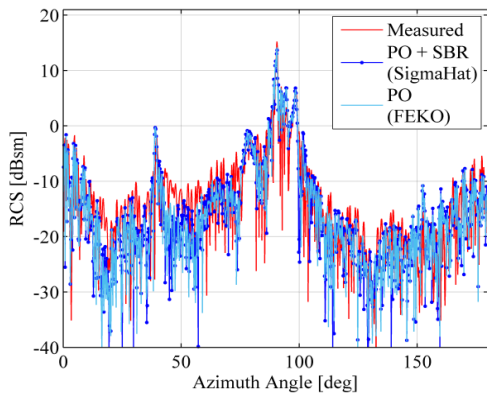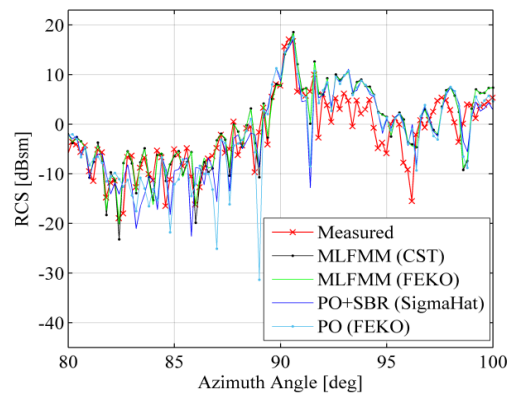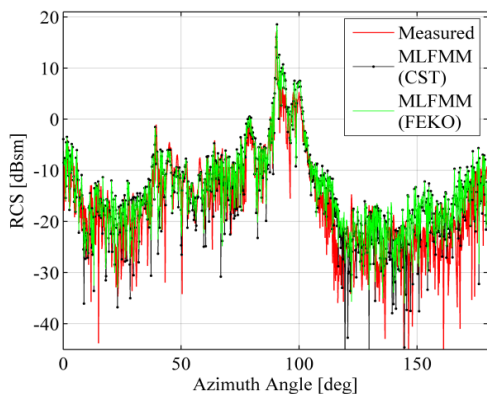

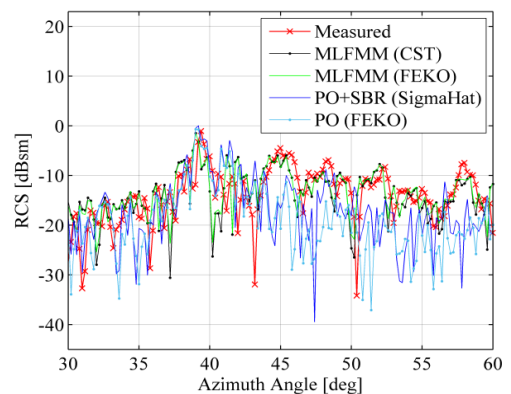Fig. 4. RCS measured at 17 GHz compared to RCS calculated with MLFMM in FEKO and in CST.

Fig. 7. RCS measured and simulated at 17 GHz at the port side wing flash and the lower RCS range.

Table 1: Summary of the accuracy metrics at 10 GHz

Metric	MLFMM (FEKO)	MLFMM (CST)	PO (FEKO)	PO+SBR (SigmaHat)
Broadside				
Max. Δ_{RCS} [a]	2.3 dB	4.1 dB	3.8 dB	1.8 dB
Range [b] $\leftrightarrow$ $\Delta_{RCS} \leq 5$ dB	26.5º	39.0º	19.5º	24.2º
Side lobe accuracy	0.2º	0.3º	0.3º	0.6º
Wing Flash				
Max. Δ_{RCS}	2.7 dB	3.1 dB	4.1 dB	3.7 dB
Range $\leftrightarrow$ $\Delta_{RCS} \leq 5$ dB	24º	29.2º	4.7º	7.6º
Side lobe accuracy	0.4º	0.4º	0.5º	0.6º
Lower RCS Range				
Max. Δ_{RCS}	4.7 dB	4.9 dB	10.5 dB	10.8 dB
Side lobe accuracy	0.6º	0.4º	0.6º (41º- 43º)	0.6º (41º- 43º)

[a]The difference between the peak RCS values.
[b]The azimuth angle range where Δ_{RCS} is equal to or less than 5 dB.

Table 2: Summary of the accuracy metrics at 17 GHz

Metric	MLFMM (FEKO)	MLFMM (CST)	PO (FEKO)	PO+SBR (SigmaHat)
Broadside				
Max. Δ_{RCS}	5.0 dB	5.0 dB	2.5 dB	3.3 dB
Range $\leftrightarrow$ $\Delta_{RCS} \leq 5$ dB	43.6º	44.8º	29.8º	24.8º
Side lobe accuracy	0.2º	0.2º	0.2º	0.2º
Wing Flash				
Max. Δ_{RCS}	4.0 dB	4.2 dB	3.5 dB	3.7 dB
Range $\leftrightarrow$ $\Delta_{RCS} \leq 5$ dB	29.4º	30.4º	8º	9.6º
Side lobes accuracy	0.4º	0.4º	0.2º	0.2º
Lower RCS Range				
Max. Δ_{RCS}	7.3 dB	8.0 dB	11.7 dB	10.1 dB
Side lobe accuracy	0.4º	0.4º	None	None

Table 3: Computational resources (Intel Xeon) for 17 GHz

	MLFMM	MLFMM	PO	PO+SBR
Software	FEKO	CST	FEKO	SigmaHat
N_{Cores}	12	12	12	16
CPU	2.3 GHz			2.7 GHz
RAM	32 GB			48 GB
Processes / Threads	12	12	12	1
Resources Required				
Memory	23.7 GB	8.0 GB	4.2 GB	0.66 GB
CPU-time per sample + mesh and matrix setup	33.7 min + 2.1 h	26.9 min + 6.9 h	52.5 s + 1.9 min	13.2 s

IV. CONCLUSION

An electrically large conducting 1:25 scale model of a Boeing 707 with a maximum electrical length of 106λ was analyzed. Instead of representing the target as a composition of simple canonical structures or using a commercially available CAD model, a very accurate 3D CAD model was created by laser scanning the model. Different CEM methods and three software packages were used to predict the RCS of the target, viz., MLFMM using CST and FEKO, PO using FEKO and PO with SBR using SigmaHat. The simulated data was validated against measured RCS data of the scale model, obtained in a compact range. All the methods showed good agreement with the measured data over the important azimuth ranges at 10 GHz and 17 GHz. The accuracies of the asymptotic methods increased as the frequency did. The accuracies with which the asymptotic methods calculated the larger RCS values (above -5 dBsm) compared well to the more rigorous full-wave methods. The lower RCS values calculated with the PO with SBR method was a slightly better approximation of the measured data compared to the PO method, at 17 GHz. In this lower RCS range the accuracies of the full-wave methods were much better than the asymptotic methods. MLFMM was the most accurate method at both frequencies, and the FEKO implementation thereof was the most accurate for the lower RCS values at 10 GHz. The most efficient in terms of computational time, memory requirements and accuracy was the PO with SBR method.

ACKNOWLEDGMENT

REFERENCES

[1] A. C. Woo, H. T. G. Wong, M. J. Schuh, and M. L. Sanders, "Benchmark radar targets for validation of computational electromagnetic programs," *IEEE Antennas and Propagation Magazine*, vol. 35, no. 1, pp. 84-90, February 1993.

[2] I. M. Martin, M. A. Alves, G. G. Peixoto, and M. C. Rezende, "Radar cross section measurements and simulations of a model airplane in the X-band," *PIERS Online*, vol. 5, no. 4, pp. 377-380, 2009.

[3] J. C. Smit, J. E. Cilliers, and E. H. Burger, "Comparison of MLFMM, PO and SBR for RCS investigations in radar applications," in *IET International Conference on Radar Systems*, Glasgow, pp. 22-27, 2012.

[4] FEKO Suite, ver. 7.0.2, Altair, South Africa, 2015.

[5] CST STUDIO SUITE®, CST AG, Germany, 2015.

Measurements of Backscattering from a Dihedral Corner in a Reverberating Chamber

Antonio Sorrentino, Giuseppe Ferrara, Maurizio Migliaccio, and Sergio Cappa

Università degli Studi di Napoli Parthenope, Dipartimento di Ingegneria
Centro Direzionale di Napoli, Isola C 4, 80143, Napoli, Italy
{asorrentino}@uniparthenope.it

Abstract ─ In this paper, the backscattering of a dihedral corner is evaluated by measurements accomplished within the reverberating chamber (RC) of the Università degli Studi di Napoli Parthenope, formerly Istituto Universitario Navale (IUN). The obtained results are found in good agreement with those of a previous very accurate model, whose validity was assessed by anechoic chamber measurements.

Index Terms ─ Anechoic chamber, dihedral corner, reverberating chamber.

I. INTRODUCTION

The dihedral corner has been largely used as target in experimental determinations of radar cross section (RCS). Moreover, it is readily applied in a wide variety of complex target configurations. Experimental studies of dihedral corner backscattering have been always accomplished within the anechoic chamber (AC) [1]. The AC is a test-environment in which each direction around the device under test (DUT) is evaluated without any extraneous reflections. In other words, the AC is an artificially simulated controlled environment in which the studies on the DUT can be performed without any reflections or diffraction from the AC walls, i.e., in an ideal environment. The AC is employed for providing antenna parameters but other measurements, such as radiated emission, radiated susceptibility, shielding effectiveness and other electromagnetic compatibility measurements (EMC) are also accomplished in it [1]. Despite of these aspects, the AC is a very expensive test-site due to the large amount of electromagnetic absorbers that are fixed on its walls, floor and ceiling [1].

In the last years, a completely different test-site, i.e., the reverberating chamber (RC) enjoys growing popularity for studies and applications on electromagnetic fields [2-12]. The RC is a metallic chamber in which the input electromagnetic field is randomized by employing different stirring techniques such as mechanical, frequency and source stirring techniques [12]. Nowadays, the RC is become a well-established standard for EMC [13] and it is recently become also standard for wireless applications [14]. Differently from the AC where only a direct link is present between the transmitting antenna and the DUT, within the RC several plane waves incoming from all directions and with own polarizations arrive to the DUT in addition to the direct link. Although from an electromagnetic point of view, the RC appears slightly more complicated with respect to the AC, from an economical point of view, it is more convenient since it is made of aluminum that is essentially much cheaper than the AC absorber. In this paper, a first approach to study the backscattering from a dihedral corner within the RC is accomplished and the obtained results are compared with those of a previous very accurate model, whose validity was already assessed by AC measurements. Although the RC walls are not covered of absorber material, experimental results show that the RC can be used as alternative test facility to the traditional AC measurement procedures for measuring the RCS of dihedral corner. This fact, in addition to its affordability, makes the RC a suitable alternative to the AC for equipping an electromagnetic laboratory with a good performance and not expensive test site facility.

II. MEASUREMENTS OF BACKSCATTERING IN RC

In an RC the field can be expressed in terms of S_{21} scattering coefficient between the two antennas. This is a common approach used to determine the statistical behaviour of the received field within an RC [8]. In particular, the field obtained can be read as a sum of a deterministic component between the transmitting and the receiving antennas and the scattered component associated to reflections and diffraction on the RC walls and stirrers. Let us call such components $S_{21,d}$ and $S_{21,r}$. Hence, S_{21} can be expressed as follows:

$$S_{21} = S_{21,d} + S_{21,r}. \qquad (1)$$

In particular, $S_{21,d}$ has zero variance and no zero mean. On the other hand, the real and the imaginary parts of the

scattered component, i.e., $S_{21,r}$, follow independent zero mean normal distribution with the same variance σ^2. Therefore, it follows that,

$$E\lfloor S_{21} \rfloor = E\lfloor S_{21,d} \rfloor + E\lfloor S_{21,r} \rfloor = E\lfloor S_{21,d} \rfloor. \qquad (2)$$

According to (2), the square amplitude of $S_{21,d}$ is equal to the power of direct link component and the variance of $S_{21,r}$ is equal to the power of multipath scattered components [10]. Since we are dealing with the radiation characteristics of a perfectly conducting dihedral corner reflector within the RC, a single but effective sample-based estimator, that takes into account the powers of the direct link and the one of the reflected/diffracted components, must be achieved. Hence, the Rice factor estimator, i.e., $\hat{K}$, is applied. $\hat{K}$ is equal to the power ratio between the direct to the scattered component of the received electromagnetic field, i.e.,

$$\hat{K} = \frac{|S_{21,d}|^2}{\left\langle |S_{21} - S_{21,d}| \right\rangle^2}, \qquad (3)$$

where $\left\langle |S_{21} - S_{21,d}| \right\rangle^2$ is the power of the scattered field component. The $\hat{K}$ factor has been estimated by following the technique developed in [3] in order to improve the accuracy of the backscattering measurements.

III. SIMULATION OF DIHEDRAL CORNER BACKSCATTERING

In this section, a brief explanation of the model employed for the dihedral corner backscattering is summarized. The model used for the simulations is a combination of the improved physical optics (IPO) model and of the physical theory of diffraction (PTD) contribution. It allows predicting very accurately the RCS of the corner in a plane normal to its wedge. The solution of the dihedral corner backscattering is given from the sum of four contributions, in sequence of their quantitative relevance:

a. the backscattering from the faces lighted from the reflected rays;
b. the backscattering due to the direct lighting by the impinging wave;
c. the backscattering due to the lighting of each face by the rays diffracted from the edge of the other one;
d. finally, the PTD correction term.

The first order contribution (a) is the first order term of interaction scattering and the second order contribution (b) is the first order term of the direct scattering, while the contribution (c) is the second order term of the interaction scattering and (d) is the second order term of the direct scattering. The joined IPO and PTD model has

been developed and experimentally assessed in [15-16] by comparisons with AC measurements. Representative results of the above-mentioned model are shown in Fig. 1, where the backscattering from dihedral corners with different sizes is reported versus the azimuthal angle. The dihedral face dimensions are $a \times b$ where a is the size of the smallest side. In particular, with respect to the working wavelength, the blue, red, green and black curves are relative to $a/\lambda = 3$, $a/\lambda = 4$, $a/\lambda = 4.5$ and $a/\lambda = 5$, respectively. In the following section, the backscattering measurements from a dihedral corner performed within the RC are compared with the simulated results obtained from the joined IPO and PTD model.
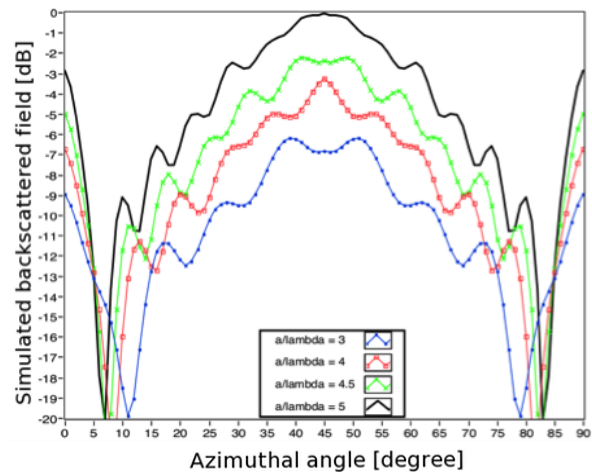
Fig. 1. Simulated dihedral backscattering for different dihedral dimensions. The graph shows the backscattered field (in dB) versus the azimuthal angle (0, 90°). The blue curve is relative to $a/\lambda = 3$; the red curve is relative to $a/\lambda = 4$; the green curve is relative to $a/\lambda = 4.5$; finally, the black curve is relative to $a/\lambda = 5$. The different curves are separated of 6, 4, 2 dB, respectively, from the black one.

IV. EXPERIMENTAL RESULTS

In this section, a meaningful set of experimental results is provided and discussed. Measurements have been conducted at the RC of the Università degli Studi di Napoli Parthenope, formerly Istituto Universitario Navale (IUN). The IUN RC is a $120\,m^3$ metallic chamber wherein five mechanical stirrers are present. The first two stirrers are volumetric stirrers. They can operate both in step or in continuous mode with a maximum speed of 15 rate per minute (rpm). The horizontal one is placed at the right side of the entrance door; the vertical stirrer is placed opposite to the entrance door. The three flat stirrers can rotate in continuous mode in clockwise or in counter clockwise and with different velocity up to 300 rpm. It is important to note that the stirrer speed

control system uses an interface connection, developed in LabVIEW, between the personal computer and the stirrer controller. Through this last one, the desired rpm of the stirrer speed is set up. The first stirrer, S1, is on the wall opposite to the entrance door, the second one, S2, is on the right of the entrance door. Finally, the third stirrer, S3, is on the ceiling of the RC. A sketch of the RC used for the measurements is shown in Fig. 2. Assuming a distance of 0.35 m from walls and stirrers, at minimum usable frequency, the working volume (WV) one considered exhibits an area of about 22 m^2 and a volume of about 70 m^3 [7]. Two Narda Standard Gain Horn working on X-band (8.20 – 12.4 GHz) have been employed, see Fig. 2. The antennas have a shape of four sided pyramids with a rectangular cross-section of 0.078×0.059 m^2 area dimensions. Measurements from dihedral corner backscattering have been accomplished by using monochromatic signals at 10 GHz frequency. The dihedron is placed about 1 m from the floor on polystyrene support and it is moved by means of a rotating table (Microcontrole ITL 09) that is managed by LabVIEW. Figure 2 shows a particular of inner of the IUIN RC used for the measurements. For each single measurement, a data set of 501 samples is acquired in 2.00 s, that corresponds to a sample time equal to about 4 ms. In all the experiments all the stirrers are operated together. In particular, the volumetric stirrers are operated at 10 rate for minute (rpm), S1 is operated at 65 rpm, S2 is operated at 45 rpm. Finally, S3 is operated at a 30 rpm. A full calibration of the entire system is *a priori* accomplished to allow obtaining data free of noise due to, for instance, to the cable losses or instrumentation thermal noise. The scattering coefficient S_{21} is measured by making use of the Agilent Technologies Network Analyzer (VNA).

The software used to off-line analyse the acquired data is developed in LabVIEW.

Figure 3 shows the comparison between the backscattering measurement of the dihedral corner with $a/\lambda = 5$ performed within the RC and the simulated ones. In particular, the red line is obtained from the RC measurement while the black line is given by simulation. A spherical coordinate system and an azimuthal angle range (0, 90°) have been considered. Two antennas are physically employed for the backscattering measurement. Hence, a pseudo-monostatic configuration with the electromagnetic field in a vertical polarization has been employed. The cross polarimetric separation of the two antennas is equal to 20 dB. Hence, it has no effect on the received dihedral corner backscattering. A fairly good agreement between measurements and simulations is shown in Fig. 3. In particular, two curves, relative to the backscattering of the dihedral corner with $a/\lambda = 5$ versus the azimuthal angle, are shown: the AC simulated one (continuous black line with crosses) and the RC measured curve (continuous red line with dots). The

good agreement between the two curves witnesses that the RC can be used as alternative test facility to the traditional AC measurement procedures for measuring the RCS of a dihedral corner. It must be noted that these backscattering measurements of dihedral corner within the IUN RC are only a first approach to the RCS measurements in a multipath environment such as the RC.
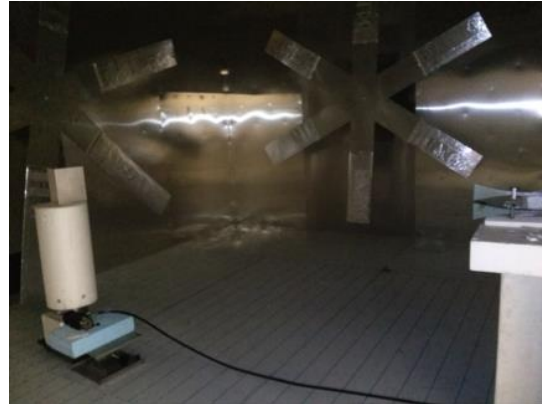
Fig. 2. Particular of the inner IUN RC with the flat S1 and S2 stirrers, the antennas in pseudo-monostatic configuration and with the dihedral corner reflector on the Microcontrole ITL 09 rotating table.
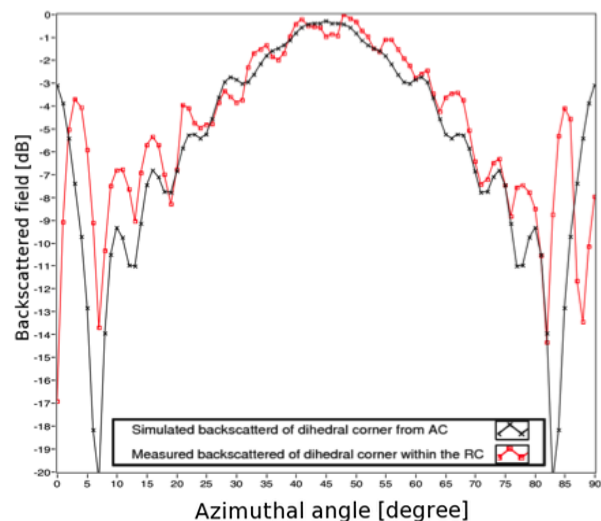
Fig. 3. Comparison between the backscattering measurement from the dihedral corner with $a/\lambda = 5$ performed within the RC (red line) and the simulated one (black line), versus the azimuthal angle.

V. CONCLUSIONS

In this paper, an innovative method for the backscattering from a dihedral corner within the RC has been proposed and successfully accomplished. Experiments conducted at the IUN RC have shown that

a significant agreement between the measurement results and the simulated ones obtained with a very accurate and reliable model occurs.

Therefore, the RC can become a valid and economical convenient alternative to the well-established AC procedures for RCS measurements.

REFERENCES

[1] L. H. Hemming, *Electromagnetic Anechoic Chambers: a Fundamental Design and Specification Guide*, IEEE Press, 2001.

[2] A. Sorrentino, A. Gifuni, G. Ferrara, and M. Migliaccio, "Mode-stirred reverberating chamber autocorrelation function: Model, multifrequency measurements and applications," *IET Microwave Antenna & Propagation*, 2015, in print.

[3] C. Lemoine, E. Amador, and P. Besnier, "On the K-factor estimation for Rician channel simulated in reverberation chamber," *IEEE Trans. on Antennas and Propagation*, vol. 59, no. 3, pp. 1003-1012, 2011.

[4] A. Sorrentino, A. Gifuni, G. Ferrara, and M. Migliaccio, "Mode-stirred reverberating chamber Doppler spectra: Multi-frequency measurements and empirical model," *IET Microwave Antenna & Propagation*, vol. 8, no. 15, pp. 1356-1362, 2014.

[5] A. Sorrentino, G. Ferrara, A. Gifuni, and M. Migliaccio, "An alternative technique for estimating the k-factor from the phase of the electromagnetic field within a reverberating chamber," *Progress In Electromagnetics Research C*, vol. 44, pp. 27-40, 2013.

[6] A. Sorrentino, G. Ferrara, and M. Migliaccio, "Kurtosis index to characterize near LOS conditions in reverberating chambers," *IET Microwaves, Antennas & Propagation*, vol. 7, no. 3, pp. 175-179, 2013.

[7] F. Moglie and V. M. Primiani, "Numerical analysis of a new location for the working volume inside a reverberation chamber," *IEEE Trans. Electromagn. Compat.*, vol. 54, no. 2, pp. 238-245, 2012.

[8] C. L. Holloway, D. A. Hill, J. M. Ladbury, P. F. Wilson, G. Koepke, and J. Coder, "On the use of reverberation chambers to simulate a Rician radio environment for the testing of wireless devices," *IEEE Trans. Antennas Propag.*, vol. 54, no. 11, pp. 3167-3177, 2006.

[9] A. Sorrentino, G. Ferrara, and M. Migliaccio, "On the coherence time control of a continuous mode stirred reverberating chamber," *IEEE Antennas and Propagation*, vol. 57, no. 10, pp. 3372-3374, 2009.

[10] A. Sorrentino, G. Ferrara, and M. Migliaccio, "The reverberating chamber as a line-of-sight wireless channel emulator," *IEEE Antennas and Propagation*, vol. 56, no. 6, 2008.

[11] G. Ferrara, M. Migliaccio, and A. Sorrentino, "Characterization of GSM non-line-of-sight propagation channels generated in a reverberating chamber," *IEEE Trans. On Comp.*, vol. 49, no. 3, pp. 467-473, 2007.

[12] D. A. Hill, *Electromagnetic Fields in Cavities: Deterministic and Statistical Theories*, NewYork, NY, IEEE Press, 2009.

[13] "Reverberation chamber test methods," International Electrotechnical Commission, Geneva (IEC), Std. 61 000-4-21, 2011.

[14] 3GPP - 3rd Generation Partnership Project RAN4 - R4-111690: TP for 37.976: LTE MIMO OTA Test Plan for Reverberation Chamber Based Methodologies, Azimuth Systems, Bluetest, CTTC, 2011.

[15] P. Corona, A. De Bonitatibus, G. Ferrara, and C. Gennarelli, "Accurate evaluation of backscattering by 90° dihedral corners," *Electromagnetics*, pp. 23-36, 1993.

[16] P. Corona, A. De Bonitatibus, G. Ferrara, and C. Gennarelli, "A very accurate model for backscattering by right angled dihedral corners," *Proceeding on Antennas and Propagation Society International Symposium*, vol. 4, pp. 1734-1737, 1990.

Geometrical Scale Modeling of Gain and Echo Area: Simulations, Measurements and Comparisons

Constantine A. Balanis, Life Fellow, IEEE, Kaiyue Zhang, and Craig R. Birtcher

School of Electrical, Computer and Energy Engineering
Arizona State University, Tempe, AZ 85287, USA
balanis@asu.edu, kaiyue.zhang@asu.edu, craig.birtcher@asu.edu

Abstract – Geometrical scale modeling is often necessary to perform measurements of parameters and figures-of-merit of antennas and radar targets with large physical dimensions that cannot be accommodated in indoor and controlled experimental facilities. The measured and simulated parameters and figures-of-merit of the scaled-models can then be translated to represent, if transformed properly, those of the full-scale models. In this paper, the basic theory is summarized which relates the gain and the echo area (RCS) of scaled models to those of their full-scale counterparts. Simulations and measurements are performed on scaled models, for both gain and RCS, and compared with those of full-scale models to verify the geometrical scaling. For the gain, a quarter-wavelength monopole on a scaled helicopter airframe, and for the RCS, a flat plate of complex configuration, are considered for simulations, measurements and comparisons. A very good agreement has been obtained for both gain and RCS between both sets of data.

Index Terms – Antenna, gain, measurement, radar cross section, scale model.

I. INTRODUCTION

In many applications (such as antennas on ships, aircraft, large spacecraft, etc.), antennas and their supporting structure are so immense in weight and/or size that they cannot be accommodated by indoor experimental facilities to measure their radiation characteristics. To overcome some of the challenges presented by physically large structures, a technique that can be used to perform antenna simulations, measurements and comparisons of fundamental parameters and figures-of-merit of antennas and scattering is *geometrical scale modeling* [1], [2]. Geometrical scale modeling is employed to:

- Physically accommodate, within small antenna ranges or enclosures, measurements on relatively small physical scaled models that can be referred to those of large structures.
- Allow experimental, environmental and security control over the measurements.

- Minimize costs and time associated with measurements of physically large structures and corresponding experimental parametric studies.

While [1] laid the foundation for scale modeling, it did not present any predictions, simulations, measurements or comparisons. This paper specifically focuses on Gain (Amplitude) and Echo Area (RCS), and illustrates both concepts with simulations and measurements of an antenna on a scale model helicopter and scattering from square and irregular-shaped metallic plates, for which full-scale and scale model data are compared. The scaling of other antenna and scattering parameters and figures-of-merit can be found in [1], [2]. The theory of geometrical scale modeling is based on the development of *absolute scale modeling* [1], of which the *geometrical scale modeling* is a special case when the ratio of the scale factor of the electric field (α) to that of the magnetic field (β) is unity ($\alpha/\beta = 1$), and the ratio of the scale factor of time (γ) and the geometrical scale factor of linear dimensions (n) is also unity ($\gamma/n = 1$). These two ratios are satisfied when the permittivity (ε) and permeability (μ) of the full-scale and scaled models are identical [1]. Both the absolute and geometrical scale modeling are based on Maxwell's equations.

II. GAIN (AMPLITUDE): SIMULATION, MEASUREMENTS AND COMPARISONS

Using Maxwell's equations and a geometrical scaling factor of n, the relationship between the antenna gain G_o (of the full-scale model) to the antenna gain G_o' (of the scaled model) are developed based on the definition of antenna gain between the two scale models. A summary of the derivation is outlined below. The scaled-model parameters are indicated by a prime. It can be shown that:

$$G_o (\text{Gain}) = \frac{U}{U_o} = \frac{4\pi U}{P_{rad}} = 4\pi \left(\frac{U}{P_{rad}} \right) = 4\pi r^2 \left(\frac{W}{P_{rad}} \right), \text{ (1a)}$$

$$G_o' = 4\pi \left(\frac{U'}{P_{rad}'} \right) \overset{U'=(r')^2 W'}{=} 4\pi \left(\frac{(r')^2 W'}{P_{rad}'} \right) = 4\pi (r')^2 \left(\frac{W'}{P_{rad}'} \right), \text{ (1b)}$$

$$G_o^{'} = 4\pi \left(\frac{r}{n}\right)^2 \frac{W/(\alpha\beta)}{P_{rad}/(\alpha\beta n^2)} = 4\pi r^2 \left(\frac{W}{P_{rad}}\right) = G_o, \quad (1c)$$

$$G_o^{'} = G_o, \quad (1d)$$

where U represents radiation intensity (W/steradian), W represents power density (W/m^2) and P_{rad} is the power (W) radiated by the antenna. Thus, the gain $G_o^{'}$ (scaled model) = gain G_o (full-scale).

For geometrical scale modeling of the antenna gain, the absolute amplitude radiation patterns of a $\lambda/4$ monopole located at the belly (bottom side) of a generic scale model helicopter [see Fig. 1 (a)], having dimensions that are about 1/10 the size of a full-scale helicopter, were simulated, measured and compared. The absolute amplitude patterns of the $\lambda/4$ monopole on the scale model generic helicopter were measured at 7 GHz along the three principal planes; *pitch*, *roll* and *yaw*. In addition, the same patterns were simulated on a full-scale helicopter (10 times larger) but at a frequency of 700 MHz (1/10 the measured frequency) of the same helicopter geometry. The pitch-plane patterns, simulated and measured, are shown in Fig. 1 (b); a very good agreement is indicated. The corresponding roll- and yaw-plane patterns are shown in Figs. 1 (c) and 1 (d), respectively. It is evident that there is, as expected, a correct scaling between the measured amplitude (gain) patterns on the 1/10 scale model but at a frequency of 7 GHz (increased by a factor of 10 since the size of the scale model was 1/10 of the full-scale) and the simulated patterns at 700 MHz (a factor of 1/10 of the measured frequency) but on a full-scale model (larger by a factor of 10). The maximum gain is about 6 dB, which is basically what is expected from a $\lambda/4$ monopole. In addition, there is an excellent comparison between the respective two sets of patterns (simulated and measured), considering the complexity of the airframe.

(a) Scale model helicopter (10:1 scale)
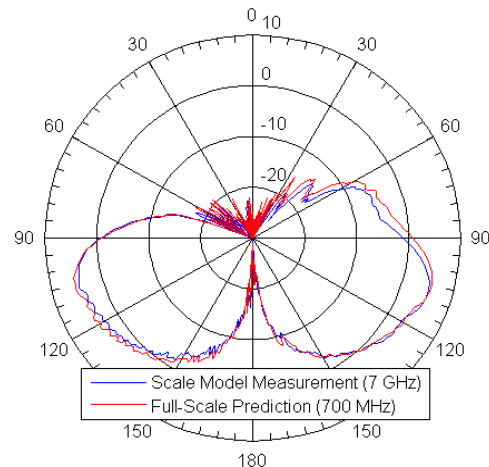
(b) Pitch-plane patterns
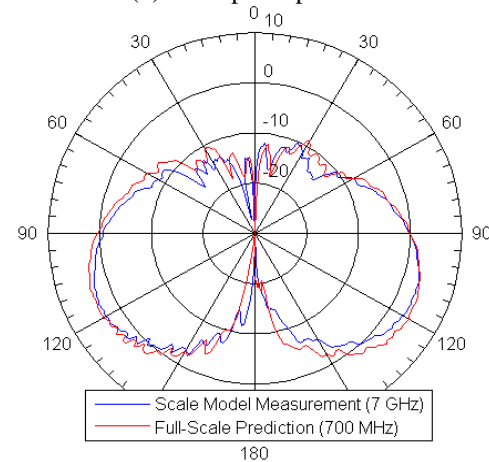
(c) Roll-plane patterns
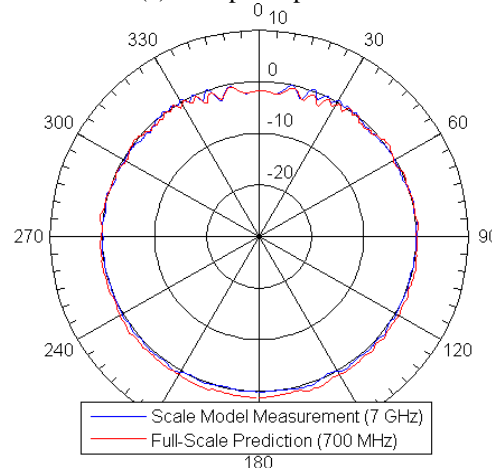
(d) Yaw-plane patterns

Fig. 1. (a) Scale model helicopter. (b) Pitch-plane scale model measurements (7 GHz) and full-scale model simulations (700 MHz) of a $\lambda/4$ monopole on the belly of the helicopter airframe. (c) Roll-plane patterns. (d) Yaw-plane patterns.

III. ECHO AREA (RCS): SIMULATIONS, MEASUREMENTS AND COMPARISONS

Using Maxwell's equations and a geometrical scaling factor of linear dimensions of n, the relationship between the echo area (RCS) A_e (of the full-scale model) to the echo area (RCS) $A_e^{'}$ (of the scaled model) are developed based on the definition of the echo area (RCS) between the two scale models. A summary of the derivation is outlined below. The scaled model parameters are indicated by a prime. It can be shown that:

$$A_e = \lim_{r \to \infty} \left[4\pi r^2 \left(\frac{W_s}{W_i} \right) \right], \tag{2a}$$

$$A_e^{'} = 4\pi (r')^2 \left(\frac{W_s^{'}}{W_i^{'}} \right) = 4\pi \left(\frac{r}{n} \right)^2 \frac{W_s/(\alpha\beta)}{W_i/(\alpha\beta)}, \tag{2b}$$

$$A_e^{'} = \frac{1}{n^2} \left[4\pi r^2 \left(\frac{W_s}{W_i} \right) \right] = \frac{1}{n^2} A_e, \tag{2c}$$

$$A_e = n^2 A_e^{'}, \tag{2d}$$

where both A_e and $A_e^{'}$ represent the echo areas (m²) of the full-scale and scaled models, respectively. Thus, the echo area (full-scale) $A_e = n^2 A_e^{'}$ echo area (scaled model).

The simulated, using the commercial software CST [3], and measured echo area (RCS) monostatic patterns of a scaled and a full-scale odd shaped flat PEC plate, whose geometry is displayed in Fig. 2, were performed and compared. The odd shape of the plate was chosen so that the target will not represent a canonical surface. The dimensions of the full-scale and scaled models are indicated in centimeters; the first number in each axis represents the dimensions (in cm) of the full-scale (large) model, while the second numbers represents the dimensions (in cm) of the scaled (small) model. The overall areas of each are 319.5 cm² and 35.5 cm², respectively. The scale factor is $n = 3$ for the linear dimensions while the scale factor is $n^2 = (3)^2 = 9$ for the areas. The frequencies for the simulations and measurements were 15 GHz (scaled) and 5 GHz (full-scale): a scaling factor of 3, which is the same as that of the linear dimensions.

The parallel (hard) polarization, simulated and measured, monostatic RCS patterns (in dBsm) of the scaled and full-scale models along the principal plane are displayed in Fig. 3 (a), while those for the perpendicular (soft) polarization are displayed in Fig. 3 (b). An excellent agreement is indicated between the simulated, using CST [3], and measured patterns, for both the full-scale (large) and scaled (small) plates. The shape of the perpendicular (soft) polarization RCS patterns of Fig. 3 (b) follow, as they should, a nearly $\sin(q)/q$ distribution based on physical optics [4] and

due to the very weak first-order diffractions from the edges of the plate for this polarization [4]. However, for the parallel polarization, the shape of RCS patterns does not follow the $\sin(q)/q$ distribution, especially at the far minor lobes, because the diffractions for the vertical (hard) polarization are more intense [4] and impact the overall distribution to be different from nearly $\sin(q)/q$.
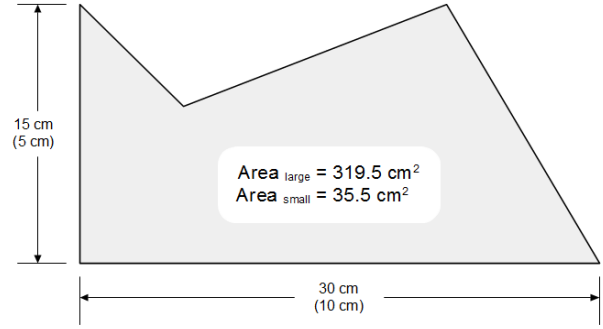
Fig. 2. Shape and dimensions (in cm) of PEC odd shape full-scale (large), and scale (small) plate for echo area (RCS) simulations and measurements.

The maximum monostatic RCS of a flat plate of any geometry, for either parallel or perpendicular polarization (both are identical based on physical optics, PO), occurs at normal incidence and is represented by [4]:

$$\text{RCS}_{max}(\text{PO}) = 4\pi \left(\frac{\text{Area of plate}}{\lambda} \right)^2. \tag{3}$$

Based on the physical optics (PO) RCS of (3), the maximum monostatic RCS occurs at normal incidence ($\theta_i = 0°$), and for the full-scale (large) plate of 319.5 cm² at 5 GHz is (the same for both the parallel and perpendicular polarizations):

$$\text{RCS(full-scale)}_{max} = 4\pi \left[\frac{319.5}{6(100)} \right]^2 = 3.563 \text{ m}^2 = 5.52 \text{ dBsm}, \tag{4}$$

while the simulated maximum of Figs. 3 (a) and 3.(b) is 5.74 dBsm (parallel polarization) and 5.85 dBsm (perpendicular polarization). The measured one for both polarizations is nearly 5.6 dBsm; thus the predicted (based on PO), simulated (using CST) and measured are within 0.3 dB.

For the scaled (small) plate 35.5 cm² at 15 GHz, the maximum monostatic RCS based on (3) is:

$$\text{RCS(scaled)}_{max} = 4\pi \left[\frac{35.5}{2(100)} \right]^2 = 0.396 \text{ m}^2 = -4.02 \text{ dBsm}, \tag{5}$$

while the simulated maximum of Figs. 3 (a) and 3 (b) is -3.79 dBsm (parallel polarization) and -3.68 dBsm (perpendicular polarization). The measured one for both polarizations is nearly -3.9 dBsm; thus the predicted

(based on PO), simulated (using CST) and measured are within 0.3 dB.

It is also apparent from the parallel polarization monostatic RCS patterns in Fig. 3 (a) and the perpendicular polarization of Fig. 3 (b) that, there is a difference of $n^2 = 3^2 = 9$ (dimensionless) or $10\log_{10}(9) = 9.54$ dB, between the scaled and full-scale (both measured and simulated) RCS patterns; i.e., the full-scale measured and simulated monostatic RCS patterns are 9.54 dB greater than those of the scaled, as they should be according to (2d). In fact, if 9.54 dB is added to the measured and simulated monostatic RCS patterns of the scaled (small) plate monostatic RCS patterns, the adjusted (by + 9.54 dB) RCS patterns match those of the full-scale (large) plate, as shown in Figs. 3 (a) and 3 (b). Again, the agreement is so good that it is difficult to distinguish any differences between any of the patterns for the full-scale and scaled plates. Such comparisons and agreements illustrate and validate the scaling principle for echo area (RCS).

area (RCS) patterns for full-scale (large) and scaled (small) odd shape flat PEC plate of Fig. 2.

IV. CONCLUSIONS

Geometrical scale model measurements are relatively inexpensive, convenient, and a quick alternative to full-scale measurements. Scale models enable one to perform measurements that otherwise may be impractical or impossible, and they can be related to those of full-scale models using the appropriate geometrical scaling. This has been demonstrated in this paper for both gain (of an antenna) and echo area (of scattering). An excellent agreement has been illustrated between scaled and full-scale simulations and measurements, using the appropriate geometrical scaling factor for gain and echo area of scaled and full-scale models. Measurements of geometrical scale models are recommended; they provide an alternative and effective process that otherwise may be impractical or not cost effective for full-scale model measurements.

REFERENCES

[1]   G. Sinclair, "Theory of models of electromagnetic systems," *Proc. IRE*, vol. 36, no. 11, pp. 1364-1370, Nov. 1948.
[2]   C. A. Balanis, *Antenna Theory: Analysis and Design*, 3rd edition, Wiley, 2005.
[3]   CST Computer Simulation Technology, https://www.cst.com
[4]   C. A. Balanis, *Advanced Engineering Electromagnetics*, 2nd edition, Wiley, 2012.

(a) Parallel (hard) polarization

(b) Perpendicular (soft) polarization

Fig. 3. Parallel (hard) and perpendicular (soft) polarizations simulated and measured monostatic echo

Review of Recent Advances and Future Challenges in Antenna Measurement

M. Sierra-Castañer

Department of Signal, Systems and Radiocommunications, ETSI Telecomunicación
Universidad Politécnica de Madrid, Madrid, 28040 Spain
manuel.sierra@upm.es

Abstract ─ This paper reviews the last advances in Antenna Measurement Field that took place during the previous years in order to analyse the challenges for the antenna measurement community, both industrial and academic, for the future years. The paper begins with an introductory review of the antenna measurement methodologies innovations, continuing with measurement systems technical improvements and concluding with the challenges for the antenna measurement community in the close future.

Index Terms ─ Antenna measurement, field acquisition, post processing techniques.

I. INTRODUCTION

Antenna measurement topic had a large evolution in the decades of 1960 to 1980, with the introduction of compact antenna test ranges and near field measurements [1-3]. Since that moment the progress has been significant, but basically the same far field (including compact antenna test range) or near field techniques, in the three classical configurations (spherical, planar or cylindrical) were used. Conversely, new antenna technologies have been proposed and designed during the last years: wideband small antennas integrated in portable systems, millimeter and submillimeter wave antennas, active antennas and smart antennas, among others.

This revolution in the antenna area has created the necessity of new advances in antenna measurement. Right now, it is really difficult to separate the performance of the antenna with respect the RF system (in the case of small or active antennas); even the antenna itself has to work, and be measured together with the digital signal processors (in the case of smart antennas); the new terahertz bands require an impressive accuracy in the acquisition system to avoid positioning errors; and the measurement of multibeam antennas should be done very fast to reduce the measurement costs. Of course, defense and space markets still require very accurate measurements. The latest advances in antenna measurement research, together with the availability of new technology, faster and more complex to acquire

data, to get accurate positioning of the antenna probes and antenna under test (AUT), and the revolution of the capability of computers have allowed to face the antenna measurement challenges created by the new antenna technology.

This paper summarizes some of the most important advances, both in hardware and software, during the last years, and finishes with the new challenges to be afforded by the antenna measurement community in the near future. The paper is divided in the following sections: Section II presents a revision of the last improvements in hardware (antenna measurement systems) and Section III some improvements in software techniques. Section IV does an analysis of the future challenges and, finally, Section V will conclude the paper.

II. ADVANCES IN NEW ANTENNA MEASUREMENT SYSTEMS

New concepts of antenna measurement solutions appeared during the last years. The paper focuses on three concepts: new systems for the measurement of small antennas, systems to cope with problematic of sub-millimeter frequencies and portable solutions for in-situ measurements. In the first case, the new communication systems require small and complex terminals, and the effect of the environment changes the radio electric performance. Reverberation chambers [4-5] emulate an isotropic multipath environment where there is a uniform (or quasi-uniform) distribution of the angle of arrival of the rays over the AUT, allowing the quasi real time measurement of small antennas or MIMO systems. Also, post-processing techniques gives the value of some important parameters for the mobile phone community as sensitivity, total radiated power and MIMO or diversity improvement. Figure 1 shows the measurement of a handset together with a phantom in a Bluetest [6] reverberation chamber.

Another solution to measure these terminals is the multiprobe system. In this case, also, almost real time measurement can be used to measure these devices in free space environment. This was not possible with the classical near field measurements where different

positioners were acquire the data. Figure 2 [7] shows a Microwave Vision Group (MVG) multiprobe system to measure small antennas or terminals. None of both environments, free space created by anechoic chambers and isotropic created by reverberation chambers, represent really the real life situation. However, their advantage is that they can be reproduced easily.

Fig. 1. Bluetest reverberation chamber (Bluetest copyright).

Fig. 2. Microwave Vision Group System to measure small antennas on terminals (MVG copyright).

Multiprobe technology was proposed in [8] using the Modulated Scattering Measurement Technique (MST). This technique allows the identification of the signal coming from each antenna probe through a different orthogonal low frequency code. Therefore, a passive combiner network can be used, and each individual probe signal in amplitude and phase can be recovered. Of course, this technology can be used for the implementation of classical near field systems (spherical, cylindrical or planar) replacing one of the axes by a multiprobe system. The main advantage of these systems is the reduction of time, since only one dimension scan is required.

The second focus area is the sub-millimeter (and Terahertz) frequency bands. Obviously, if classical near field solutions are employed, the acquisition precision has to be extremely high to be able to transform in a precise way the near field to far field. Nearfield Systems

Inc. (NSI) proposed a very high accuracy positioning system for millimeter applications based on the modern robotic technology to precisely position the AUT on the spherical grid [9]. A. Räisänen research group at Aalto University presented a completely different concept [10]. They designed holograms as collimating elements in a Compact Antenna Test Range (CATR) to measure antennas up to 650 GHz. In the amplitude holograms, the transmittance of the hologram T(x,y) relates the transmitted electromagnetic field to the incident electromagnetic field. Also, phase holograms can be designed where the dielectric material of the structure is patterned in the right way. Most of the holograms designed by Aalto University are binarized amplitude ones, where the structure is used to generate a plane wave in the quiet-zone. The main advantages of the holograms include the low manufacturing cost and the possibility of building the CATR at the test site. The main disadvantages of the holograms are the losses and the cross-polar performance. Also, these holograms have narrow frequency band compared with reflector CATR.

The last focus area is related to in-situ measurements. Figure 3 shows the multiprobe StarBot system designed by MVG for the measurement of on-board antennas in airplanes. Figure 4 shows the Portable Antenna Measurement System (PAMS) that takes the form of a gondola suspended from the existing cranes. Astrium GmbH has built it, with support from ESA's Advanced Research in the Telecommunication Systems (ARTES) programme [11]. In Fig. 4, PAMS is shown performing near-field probing along a tilted and planar-oriented scan surface. This solution, together post-processing tools, is very convenient for the measurement of satellite antennas. It is also remarkable the work of some researchers from Politecnico de Torino. They designed an antenna test system using a flying hexacopter equipped with RF transmitter and a telescopic dipole [12]. All these solutions simplify the measurement process, making it closer to the design laboratory or to the final placement of the antenna.

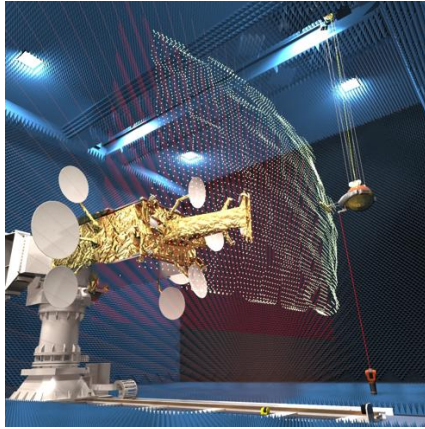Fig. 3. Microwave Vision Group StarBot system (MVG copyright).

Fig. 4. Portable Antenna Measurement System designed by Astrium GmbH under the ARTES program (ESA).

III. RECENT ADVANCES IN ALGORITHMS FOR ANTENNA MEASUREMENTS

During the last years large improvements have been done in algorithms for the post-processing of the acquired data. Near to far field algorithms have been improved in order to be able to measure in non-uniform grids. Particularly, Fast Irregular Antenna Field Transformation has been developed by Technical University of Munich to be able to process the data acquired with the PAMS system explained in the previous section [13-14]. Also, there has been a large improvement in the reduction of acquisition time. In this sense, it is remarkable the work developed during the last years by University of Salerno and University of Naples Federico II [15], where different acquisition schemes have been optimized for cylindrical or spherical scans depending on the shape of AUT. Pursuing this time reduction, Microwave Vision Group, Technical University of Madrid and Aachen University published a comparison of different methods to perform single cut near field to far field methods [16]. All these improvements mean an important reduction in the measurement time.

Also, there has been a rapid evolution in post-processing tools to improve the results of the measurement. Commercial antenna diagnostic tools, as Insight© (MVG) or Diatool© (TICRA), allow a very accurate source reconstruction technique. Other commercial tools, as Mars© (NSI), Isofilter© (MI-Tech) or MVEcho© (MVG) use the decomposition of the acquired field in cylindrical or spherical modes to filter out echoes and other spurious signals. The translation of the near or far field data to other domains (as modes or currents on the antenna surfaces) allows the engineers to recognize and correct errors in an easiest and fastest way. Obviously, the progress in this field has been supported by a deep study in universities and research centres.

Finally, last improvements in the combination of simulation and measurements allow a more accurate and

fast antenna design. In [17], some new concepts in the combination of both tools were presented. All these improvements, combined with the new antenna measurement systems, allow measuring more accurate and faster.

IV. ANTENNA MEASUREMENT CHALLENGES IN A CLOSE FUTURE

The rapid evolution of antenna technology will demand more and more flexibility and reduction in measurement time for the antenna measurements. The antenna industry will demand in-situ, real time, accurate and cost effective measurements. The use and combination of the previous studied techniques and new improvements will allow facing these challenges. In-situ measurements will be required: antenna measurement laboratories will move to the antenna place and not the opposite as we are used to work. The acquisition will be performed using commercial robots, reducing the cost of the measurement equipment. Post-processing techniques will be necessary to substitute the anechoic environments and accurate positioners by less controlled measurement areas. The use of information of positioning of the antenna probe, using laser trackers or other technologies, and the knowledge of AUT geometry, combined with source reconstruction techniques will allow to substitute the high accuracy in the positioning system. This will be completed with the use of post-processing techniques to reduce the effect of reflections or other spurious signals. For larger antennas, unmanned vehicles, with irregular grids, will be used to perform the acquisitions.

A second challenge is the complete integration of the antenna measurement phase in the design and production chain. Simulations and measurements will be combined to optimize the antenna production. Antenna simulation and measurement post-processing platforms will merge in common platforms.

Of course, there will be some specific markets, as space or security, where the classical antenna measurement systems will be used. In this case, the accuracy of the positioning systems will be the most important challenge to improve the accuracy and move to higher frequency bands. Finally, the antenna designers will require the characterization of antennas integrated in the communication systems. In this case, the antenna measurement platforms will have to be able to calculate the quality factors used by the system engineers.

V. CONCLUSION

This document has presented a review of some of the recent advances in the previous years, both in hardware and software technologies. Finally, last section has presented some of the challenges that antenna measurement community will afford during the future years: in-situ measurements, irregular positioning systems, combination of measurements and simulation

for making most effective the design process, and measurement of antennas integrated in the whole communication system. The combination of these improvements will make the antenna measurement process easier and most integrated in the antenna or system simulation platforms.

ACKNOWLEDGMENT

REFERENCES

[1] W. M. Leach and D. T. Paris, "Probe compensated near-field measurements on a cylinder," *IEEE Trans. Antennas Propagat.*, vol. AP-21, no. 4, pp. 435-445, July 1973.

[2] J. E. Hansen (Ed.), *Spherical Near-field Antenna Measurements*, Peter Peregrinus Ltd., London, U.K., 1988.

[3] A. D. Yaghjian, "An overview of near-field antenna measurements," *IEEE Trans. Antennas Propagat.*, vol. AP-34, no. 1, pp. 30-44, Jan. 1986.

[4] D. A. Hill, M. T. Ma, A. R. Ondrejka, B. F. Riddle, M. L. Crawford, and R. T. Johnk, "Aperture excitation of electrically large lossy cavities," *IEEE Trans. on Electromagnetic Compatibility*, vol. 36, pp. 169-178, 1994.

[5] P. S. Kildal and K. Rosengren, "Correlation and capacity of MIMO systems and mutual coupling, radiation efficiency and directivity gain of their antennas: simulations and measurements in reverberation chamber," *IEEE Communications Magazine*, vol. 42, no. 12, pp. 102-112, Dec. 2004.

[6] www.bluetest.com

[7] www.microwavevision.com

[8] J. C. Bolomey and F. Gardiol, *Engineering Applications of the Modulated Scatterer Technique*, Artech House, 2001.

[9] D. Janse van Rensburg, "Factors limiting the upper frequency of mm-wave spherical near-field test systems," *Proceedings of European Conference on Antennas and Propagation (EuCAP 2015)*, Lisbon, Apr. 2015.

[10] T. Hirvonen, J. Ala-Laurinaho, J. Tuovinen, and A. V. Räisänen, "A compact antenna test range based on a hologram," *IEEE Trans. on AP*, vol. 45, no. 8, pp. 1270-1276, 1997.

[11] H. J Steiner, T. Fritzel, A. Geise, C. Schmidt, and M. Paquay, "First results of innovative mobile near-field antenna measurement system for extreme large DUTs," *Proceedings of EuCAP*, 2015.

[12] G. Virone, A. M. Lingua, M. Piras, A. Cina, F. Perini, J. Monari, F. Paonessa, O. A. Peverini, G. Addamo, and R. Tascone. "Antenna pattern verification system based on a micro unmanned aerial vehicle (UAV)," *IEEE Antennas and Wireless Propagation Letters*, vol. 13, 2014.

[13] T. Eibert and C. Schmidt, "Multilevel plane wave based near-field far-field transformation for electrically large antennas in free-space or above material halfspace," *IEEE TAP*, vol. 57, no. 5, 2009.

[14] R. A. M. Mauermayer and T. F. Eibert, "Combining the fast irregular antenna field transformation algorithm with asymptotic high frequency methods," *Proceedings of EuCAP*, 2015.

[15] F. D'Agostino, F. Ferrara, C. Gennarelli, R. Guerriero, and M. Migliozzi, "Experimental testing of nonredundant near-field to far-field transformations with spherical scanning using flexible modellings for nonvolumetric antennas," *International Journal of Antennas and Propagation*, vol. 2013.

[16] R. Cornelius, T. Salmerón-Ruiz, F. Saccardi, L. Foged, D. Heberling, and M. Sierra-Castañer, "A comparison of different methods for fast single-cut near-to-far-field transformation," *IEEE Antennas and Propagation Magazine*, vol. 56, no. 2, pp. 252-261, Apr. 2014.

[17] G. Giordanengo, F. Vipiana, L. J. Foged, F. Saccardi, F. Mioc, M. Bandinelli, M. Bercigli, M. Sabbadini, and G. Vecchi, "Combined NF antenna simulation/measurement for fast testing," *Proceedings of EuCAP*, 2015.

Specific Absorption Rate for Agri-Food Materials from Multiple Antenna Exposure

Dinh Thanh Le [1] and Bruno Bisceglia [2]

[1] Faculty of Radio-Electronics Engineering
Le Quy Don Technical University, 236, Hoang Quoc Viet, Hanoi, Vietnam
le.dinhthanh.vn@ieee.org

[2] Department of Industrial Engineering
University of Salerno, Via Giovanni Paolo II, 132, 84084 Fisciano (SA), Italy
bbisceglia@unisa.it

Abstract — This paper presents an evaluation of the Specific Absorption Rate (SAR) in agri-food when it is exposed to wireless communication devices with multiple transmitting antennas. In particular, we model a simplified coconut which is exposed to antennas working at the frequency of 2.45 GHz. Two antenna configurations are being considered. One is a single dipole antenna, and the other is two co-polarized dipole antenna array. As a result, we observed that the SAR of the coconut for single antenna case is relatively smaller than that for multiple antenna one.

Index Terms — Agri-food, coconut, multiple antennas, SAR, RF exposure.

I. INTRODUCTION

In recent years, exposure to electromagnetic fields becomes more and more important issues for both electrical engineers, and public concerns. Environmental exposure has been increasing rapidly as many kinds of wireless communication systems are being developed. In such living environments, not only human, but also other living things such as animals or crops/fruits are also exposed. While there are a number of publications about human body exposed to electromagnetic sources, quite a few publications addressing the issues of agri-food exposed to electromagnetic fields. In fact, microwave applications in agri-food are an innovative and promising research trend. Microwave treatment could be a sustainable solution for food security, rural/agricultural development, and healthy food for healthy life. The knowledge of dielectric properties of food is important in designing and developing dielectric heating equipment. Therefore, it is important to evaluate the effects of RF exposure on food and in particular how the treatment affects the organoleptic properties of food. The evaluation of SAR (Specific Absorption Rate) gives an insight about the dosimetric parameters.

The exposure to electromagnetic fields of a communication system can be evaluated in different schemes. When the system is near to human body or objects such as crops/fruits, the specific absorption rate (SAR) should be evaluated, and the maximum SAR value should be below a limited number. The SAR is the amount of power absorbed per unit mass of a biological object, and can be computed as:

$$SAR = \frac{\sigma |E|^2}{\rho} \quad \text{[W/Kg]}, \quad (1)$$

where σ is the conductivity, ρ is the mass density, and E is the electric field measured in the biological object.

For human body exposure, the SAR is required to report in form of spatial-average SAR in 1g or 10g according to RF safety international standards [1-3]. The limited value of SAR is 2 W/Kg for 10g spatial-average SAR or 1.6 W/Kg for 1g spatial-average SAR. For agri-foods, there is no guideline or limitation of the exposure level. Since they are living things, and may be affected from exposure to electromagnetic fields, the investigation on SAR of agri-foods will be important for safety food issues.

In this paper, we will carry out a simple study on the exposure of coconut (an example of agri-food materials) to electromagnetic fields radiated from single and multiple sources. A simplified four-layer spherical coconut is modeled and exposed to one antenna and two-antenna cases in Section II. Results and discussions of SAR distributions and levels will be presented in Section III, which is followed by concluding remarks in Section IV.

II. MODELS

For an initial study on the respond of argi-foods to exposure of electromagnetic fields, we will investigate on coconut's fruits as an example. A coconut is simplified as a spherical model, and the size is an averaged-size of real ones. The coconut model consists

of four layers, including the green skin layer (exocarp), the pulpy layer (mesocarp), the hard shell layer (endocarp), and the coconut liquid (endosperm). The electrical parameters of the layers at the frequency of 2.45 GHz is shown in Table 1 which have been presented in [4]. Instead of far field exposure - modeled by a plane wave - in [4], in this paper the coconut is exposed to electromagnetic fields radiated from antennas placed close to it. Two antenna configurations are considered. One is a single dipole, and the other is a multiple antenna scheme which consists of two co-polarized dipoles, spacing a quarter of wavelength. All the antennas are working at 2.45 GHz. The reason to take examinations on multiple antennas is that there will be microwave applications utilizing multiple antennas on treatments or supervisions of food security, rural/agricultural development, and safety foods. Such applications can be the exposure sources for the agri-food. Thus, evaluation of SAR of such systems will be necessary for dosimetric evaluations.

Since we are interested in examining the responds of argi-foods to exposure of electromagnetic fields, the exposure apparatus will be considered in simplified configurations. The dipoles are fed by ideal sources in simulations. However, ones can improve the models with more practical issues including feeding systems as standard dipoles for compliance tests [1, 2]. The lengths of the dipole antenna are chosen so that its reflection coefficient (S11) is well below -10 dB when they are operating near the coconut model. Figure 1 illustrates the coconut model and antenna configurations. Dimensions of both coconut model and antennas are given in millimeter.
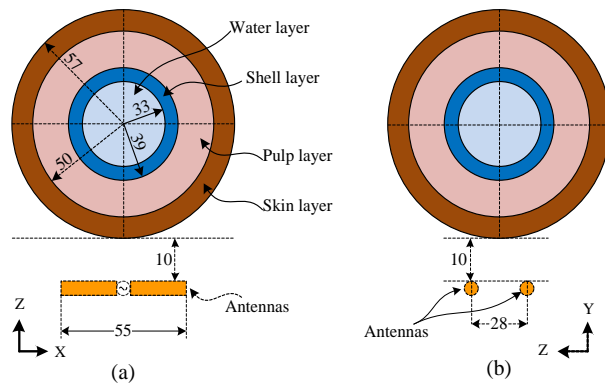

Fig. 1. The simplified four-layer coconut model and radiating antennas working at the frequency of 2.45 GHz: (a) front view XZ plane (for both cases of single and multiple antennas), and (b) side view – YZ plane (for the case of multiple antennas). All dimensions in mm.

The coconut and antennas are modeled and simulated using the electromagnetic simulation software CST Microwave Studio (CST MWS) with transient analysis computations in order to calculate the SAR [6]. The SAR will be examined in terms of 1g, 10g spatial average as well as the point SAR to analyze SAR distributions inside the coconut.

Table 1: Electrical properties of coconut layers at the frequency of 2.4 GHz [4]

Layer	ε_r	tagδ	Mass (ρ) [Kg/m^3]
Skin	19.5	0.53	1064
Pulp	37	0.67	976.5
Shell	120	0.68	1013.6
Water	75.4	0.22	1013

III. RESULTS AND DISCUSSIONS

The input powers to each antenna in the multiple antenna configurations are kept equally. In addition, the SAR is computed for incident power being normalized to 1 W. Table 2 shows the values of spatial-average SAR for 1g and 10g, and maximum local point SARs in different configurations. It is interesting that the SAR values for multiple antenna case can be lower than those for single antenna case. It is because the SAR for multiple antenna case depends on the change of the relative phase of signals from two antennas. In addition, the two antennas are spaced by a quarter of wavelength that would cause a strong mutual coupling between the antennas, thus reducing radiated energy from them.

Figure 2 shows the SAR distributions of the coconut in YZ and XZ planes when it is exposed to one antenna. The SAR is normalized to its maximum point value. As can be seen from this figure, there is only one peak SAR point and it is right close to the expose source (antenna). In addition, Fig. 3 illustrates the SAR distributions of the coconut in YZ plane for the case of multiple antennas. The SARs for three values of the relative phase of signals (β of 0, 90 and 180 deg.) are taken in simulation (respectively called SAR_0, SAR_{90}, and SAR_{180}). We can see that while there is only a local peak SAR in the single antenna case, there may be more than one local peak SAR in the case of multiple antennas.

Table 2: Evaluated SAR [Kg/W] in different models. Incident power is normalized to 1 W

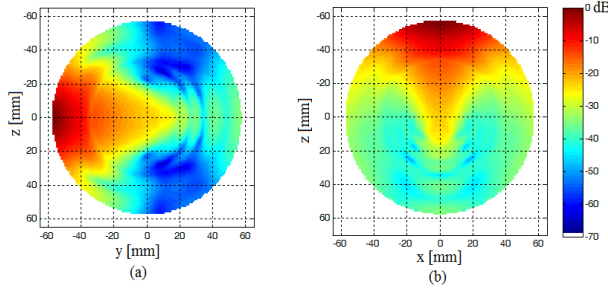| Model	SAR_{1g}	SAR_{10g}	Maximum point SAR
Coconut 1 antenna	16.92	41.11	76.14
Coconut 2 antennas ($\beta = \pi$)	0.75	1.73	2.64

Fig. 2. SAR distributions for one dipole antenna case: (a) in YZ plane, and (b) in ZX plane.
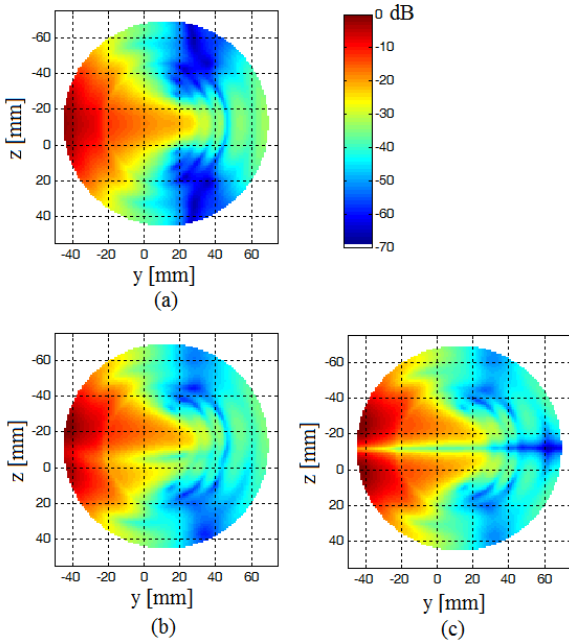

Fig. 3. SAR distributions for different relative phases between two dipole antennas: (a) for β of 0 deg., (b) for β of 90 deg., and (c) for β of 180 deg.

In order to find the value of relative phase that cause the maximum SAR, we utilize the estimation technique developed in our research group in previous works [5]. The three SAR values, i.e., SAR_0, SAR_{90}, and SAR_{180}, will be used to estimate the SAR for other value of β accordingly to the following expression [5]:

$$SAR = C_1 + C_2 \cos\beta + C_3 \sin\beta, \qquad (2)$$

where C_1, C_2, and C_3 are estimation factors which can be determined by:

$$\begin{cases} C_1 &= & (SAR_0 + SAR_{180})/2 \\ C_2 &= & (SAR_0 - SAR_{180})/2 \\ C_3 &= & (2SAR_{90} - SAR_0 - SAR_{180})/2 \end{cases}.$$

By utilizing the estimation in Equation (2), we can find the relative phase β_{max} that causes the maximum SAR. Figure 4 shows the maximum point SAR for different relative phases between two dipole antennas. Here, we

can see that the peak maximum point SAR corresponds to the relative phase of 145 deg.
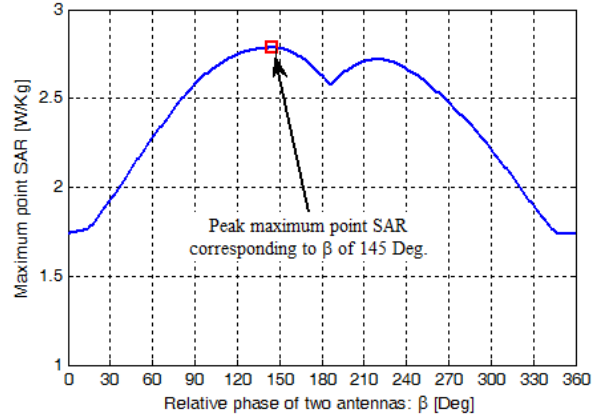
Fig. 4. Maximum point SAR for different relative phases between two dipole antennas. The peak maximum point SAR corresponds to the relative phase of 145 deg.

Figure 5 shows the SAR distribution inside the coconut when it is exposed to electromagnetic fields radiated from the two dipole antennas with the relative phase of 145 deg. Compared to the SAR in Fig. 4, the peak SAR point in Fig. 5 is slightly greater, yielding a higher SAR value.
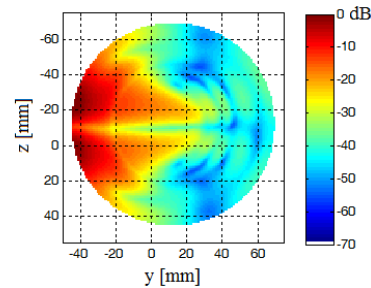
Fig. 5. SAR distribution for the relative phase between two dipole antennas of 145 deg.

The above analysis is based on computational data where the antennas and the coconut are modeled and simulated in the CST Microwave Studio. Experiment on SAR measurements for this case could be very complicated because it might require multi-layer dielectric materials for the coconut model, and complex electric field probes inside the model to capture E-filed or SAR values. The measurement procedures can be similar to the procedures to evaluate SAR of human model specified in [1] and [2], where E-field probes measure the electric fields inside a phantom filled by liquids or dielectric materials. The measured E-field will be then converted into SAR for evaluation. For the case of multiple antenna exposure, it is necessary to set the

phase difference between the antennas in every measurement in order to determine the maximum SAR.

IV. CONCLUSION

This paper presents an initial study on the respond of agri-food materials exposed to electromagnetic fields radiated from multiple antennas. A coconut model is taken as an example of agri-food materials, and two antenna configurations at 2.45 GHz are examined as exposure sources. As a result, several SAR distributions inside the coconut are presented and analyzed. For multiple antenna exposures, due to the correlation and the change of relative phase of signals, the SAR might be lower than that of single antenna exposure. Since there is quite limited number of research on SAR of agri-foods, we expect that this research can be a reference for further works on the fields.

ACKNOWLEDGMENT

REFERENCES

[1] IEEE 1528 Standard, "IEEE Recommended Practice for Determining the Peak Spatial-Average Specific Absorption Rate (SAR) in the Human Head from Wireless Communications Devices: Measurement Techniques," ed. 2013.

[2] IEC 62209-1 Standard, "Human exposure to radio frequency fields from hand-held and body-mounted wireless communication devices - Human models, instrumentation, and procedures - Part 1," Mar. 2010.

[3] ICNIRP, "Guidelines for limiting exposure to time-varying electric, magnetic and electromagnetic fields (up to 300 GHz)," *Health Phys.*, vol. 74, pp. 494-522, 1998.

[4] A. Kundu, B. Gupta, and S. Ray, "A study of specific absorption rate in coconut exposed to RF radiation," *Microwave Review*, vol. 20, no. 1, Sep. 2014. [available online: http://www.mtt-serbia.org.rs/ microwave_review/pdf/Vol20No1%20-%2002% 20-%20AKundu.pdf].

[5] D. T. Le, L. Hamada, S. Watanabe, and T. Onishi, "Measurement procedure to determine SAR of multiple antenna transmitters using scalar electric field probes," in *Proc. of the IEEE Conference on Advanced Technologies for Communications ATC2014*, Hanoi, Vietnam, Oct. 2014.

[6] CST Microwave Studio, Computer Simulation Technology, [online: https://www.cst.com].

Hybrid Electromagnetic Modeling of Lens-Integrated Antennas for Non-Contact On-Wafer Characterization of THz Devices and Integrated Circuits

Cosan Caglayan [1], Georgios C. Trichopoulos [2], and Kubilay Sertel [1]

[1] Electrical and Computer Engineering Department
The Ohio State University, Columbus, OH, 43212, U.S.A
caglayan.1@osu.edu, sertel.1@osu.edu

[2] School of Electrical, Computer and Energy Engineering
Arizona State University, Tempe, AZ, 85289, U.S.A
gtrichop@asu.edu

Abstract—A hybrid full-wave/quasi-optical electromagnetic model for the design of lens-integrated THz antennas for high frequency non-contact device characterization (30 GHz – 3 THz) is presented. Experimental validation of the antenna properties (input impedance and radiation pattern) is also provided to demonstrate the accuracy of the proposed model.

Index Terms — Double-slot antenna, lens antenna, moment method, ray tracing, sub-millimeter waves.

I. INTRODUCTION

Millimeter wave (mmW: 60-300 GHz) and sub-millimeter wave (sub-mmW: 300-3000 GHz) bands are poised to become increasingly utilized in many key applications in the near future, such as high-speed communications, sensing and imaging as well as spectroscopy and non-destructive evaluation. All-electronic systems that can achieve ultrafast switching and extremely-high-frequency operation are badly needed for the proliferation of such sensing and spectroscopy methodologies. In an effort to realize such systems, millimeter-wave and sub-millimeter-wave integrated circuit (IC) technologies using high electron mobility material systems and novel device topologies are being considered.

In addition, testing and characterization of such ICs at their intended operation frequency has long been a challenge due to several bottlenecks. Particularly, the physical fragility of fine-tip contact probes used for on-wafer characterization incurs high maintenance costs and are plagued by repeatability issues. These problems are exacerbated as the operation frequency approached 1 THz, leading to prohibitive costs and large measurement errors.

As an alternative, we recently developed [1] a non-contact on-wafer device characterization approach using a low-cost and wear/tear free setup. This novel contact-free measurement setup consists of planar on-chip receiving and transmitting antennas in a coplanar waveguide environment as illustrated in Fig. 1. An electrically-large, high-resistivity silicon hemispherical lens couples the signals into and out of the device-under-test through the on-chip antennas. To optimize antenna-to-device coupling over a wide bandwidth, the antenna design as well as the effects of the electrically-large, high-index material (n~3.5) lens need to be carefully modeled. Here, we present a hybrid electromagnetic model that employs the Moment Method (MoM) for the slot antenna on the focal plane of the lens and a Ray-Tracing/Huygens-Integral to capture the first-order effects of the electrically large lens. With this approach, a system level computational analysis of the non-contact probe setup can be evaluated. The overall signal coupling performance into and out of the device-under-test can be accurately evaluated using this hybrid computational tool. As verification, the on-wafer antenna impedance is measured using conventional contact-probes at 325-500 GHz and comparisons of the experimental data along with full-wave simulations using HFSS-v.15 and the proposed hybrid approach are provided.

II. PLANAR WIDEBAND ANTENNAS FOR ON-WAFER NON-CONTACT MEASUREMENTS

For contact-free device measurements in mmW and THz bands, the device-under-test is fabricated in a coplanar waveguide (CPW) environment, as illustrated in Fig. 1. The input signal is injected through a planar antenna interfacing with the CPW and placed at the focal plane of a large hemispherical lens. The scattered signal is coupled to the network analyzer's receiver port through a second planar antenna symmetrically placed at the output port of the device. As such, this system

incorporates quasi-optical wave propagation for efficient signal coupling from the network analyzer ports to the on-wafer device terminals. However, due to the very large electrical size of the quasi-optical components (e.g., lenses and mirrors with apertures >30λ), a full-wave numerical simulation of the system is not practical for design purposes. Below, we present a hybrid approach that combines a full-wave solution for the antenna on the wafer and a scalar diffraction approximation to evaluate the effects of the electrically-large lens for fast and accurate analysis of the quasi-optical non-contact link between the test ports and the on-chip device.
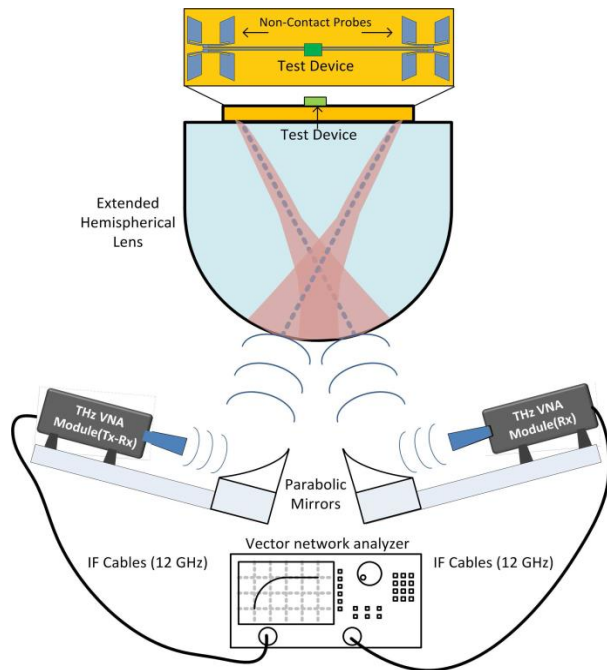

Fig. 1. Quasi-optical coupling setup for the non-contact probe testbed [1].

III. HYBRID ELECTROMAGNETIC MODELING FOR THE QUASIOPTICAL SIGNAL COUPLING

Through careful design of antenna arms and the feed region, butterfly-shaped slot antennas, such as the design depicted in Fig. 1 can achieve much better impedance bandwidth than the previously-studied double-slot antennas [2, 3]. An important simplification can be realized for the antenna impedance design if we assume that the electrically-large hemispherical lens is infinite in extent. This assumption is justified since typical lens sizes are on the order of $d > 30\lambda$, where d is the lens diameter. As such, the magnetic current distribution as well as the input impedance of the antenna can be computed using a half-space Green's function and the magnetic field integral equation (MFIE) [4].

This is achieved by incorporating the half-space Green's function to model the electrically large hemispherical lens, as discussed in [4]. Subsequently, the slot antenna placed at the lens-air boundary was analyzed using moment method in conjunction with quadrilateral elements and conformal rooftop basis functions as detailed in [5].

Curvilinear (bi-quadratic) quadrilateral finite elements and rooftop basis functions were used in the moment method implementation of the antenna problem, as illustrated in Fig. 2 (a) [5]. Although approximate, this approach is extremely efficient for antenna impedance design and to optimize the coupling between the antenna and the device CPW environment. Nevertheless, to evaluate the antenna far-field patterns outside the hemispherical lens and assess the overall signal coupling performance, a quasi-optical modeling of the probe antenna is still needed.

To a first-order approximation [4], the antenna magnetic currents computed via the MoM solution can be used to calculate the far-field radiation patterns into the lens dielectric (assuming an infinitely large lens). Subsequently, ray-tracing (or physical-optics) can be used to compute the antenna pattern outside of the hemispherical lens, as illustrated in Fig. 2 (b). To do so, we first compute the radiated fields just inside the lens-air interface. Next, we use the Fresnel transmission coefficients for both polarizations by tracing the rays emanating the antenna center and impinging upon the inner surface of the lens. Upon multiplying the radiated field intensities on the inner surface of the lens with the corresponding Fresnel transmission coefficients for each associated ray, the tangential electromagnetic fields on the outer surface of the lens can be computed. The final step to compute the antenna pattern outside the lens surface is to apply Huygens-Fresnel principle to the tangential field intensities on the outer lens surface. For example, Fig. 2 (c) depicts the computed E-field intensity of the probe antenna beams propagating away from the silicon lens. As seen, since the input and output antennas are located off the optical axis of the lens, the radiated/received patterns point away from the optical axis. As such, the input and output test signals can be effectively decoupled into the respective ports of the network analyzer using off-axis parabolic mirrors with minimal spill-over/cross-talk. The quasi-optical properties of the antennas beams, such as the Gaussicity [6] can then be calculated to optimize the overall probe system.
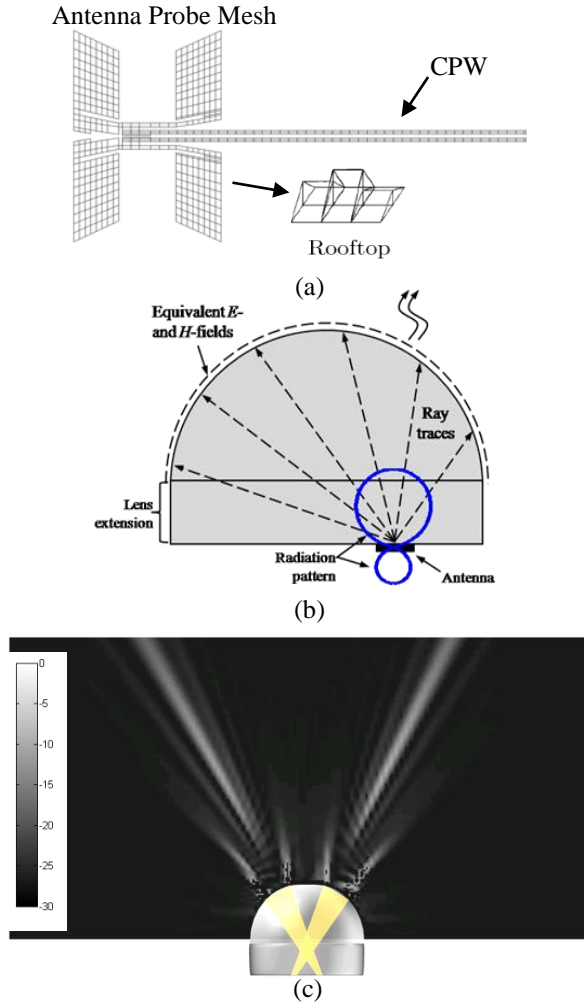
Antenna Probe Mesh

(a)

(b)

(c)

Fig. 2. Hybrid electromagnetic modeling of THz probe antennas: (a) discretization of the antenna slots with bi-quadratic mesh, (b) ray-tracing/physical optics analysis for the THz antenna radiation pattern in the presence of the hemispherical lens, and (c) computed E-field intensity distribution of both receiving and transmitting THz probe antennas.

IV. EXPERIMENTAL VALIDATION OF NON-CONTACT PROBE ANTENNA DESIGN

To illustrate the effectiveness of the proposed approach, we fabricated and characterized a sub-mmW on-chip antenna at the WR 2.2 (325-500 GHz) band. A commercially available contact probe (i500 from Cascade Microtech) was used to conduct input impedance measurements while the antenna chip was placed over the metallic chuck of the probe station. The thickness of the antenna substrate was 380 μm (which is much larger than a quarter wavelength and thus satisfies infinite half-space assumption). However, the radiation boundary

conditions are violated by the presence of the metal chuck. In order to mitigate this problem, a lossy silicon wafer (1 Ω.cm) with 500 μm thickness was added as an absorbing layer under the antenna substrate. In order to further isolate the chip under test from the chuck metal, a 3 cm thick Styrofoam was used as a supporting structure to the substrate and silicon slab. The illustration of this dielectric stack and the on-wafer micrograph of antenna-under-test are shown in Fig. 3 (a).

The contact probe was calibrated up to an on-wafer reference plane using the offset-short calibration kit shown in Fig. 3 (b). To do so, a Short-Open-Load (SOL)-type calibration [7] was employed to account for the systematic errors in the probing fixture, including the repeatable effects of landing pads, the CPW taper and the 100 μm-long section of the transmission line. Two additional standards were used to further suppress non-repeatable errors using a least-squares fit for the error matrix as discussed in [7].

(a)

(b)
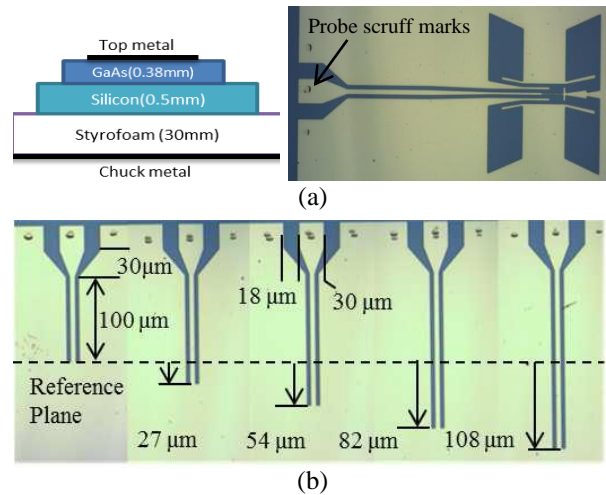
Fig. 3. On-wafer measurement of the non-contact probe antenna: (a) Illustration of the measurement layout and the micrograph of the fabricated antenna with contact probe landing pads, and (b) micrograph of on-wafer offset-short calibration kit

The measured input impedances of the two fabricated antennas are shown in Fig. 4, along with the MoM and HFSS-v.15 simulation data. As seen, both the real and imaginary parts of antenna impedance are in excellent agreement with both simulations. The slight deviations from computed antenna impedance are primarily due to variations in the micro-fabrication of the on-chip antennas. We note that the input impedance is very sensitive to the matching stub geometry at the center CPW connecting two slots to each other.

Design modifications implemented in the feed area do not significantly affect the radiation characteristics of

the butterfly antenna, which is primarily determined by the shape of the slots. Radiation pattern measurements of this type butterfly-antenna topology can be found in [3].
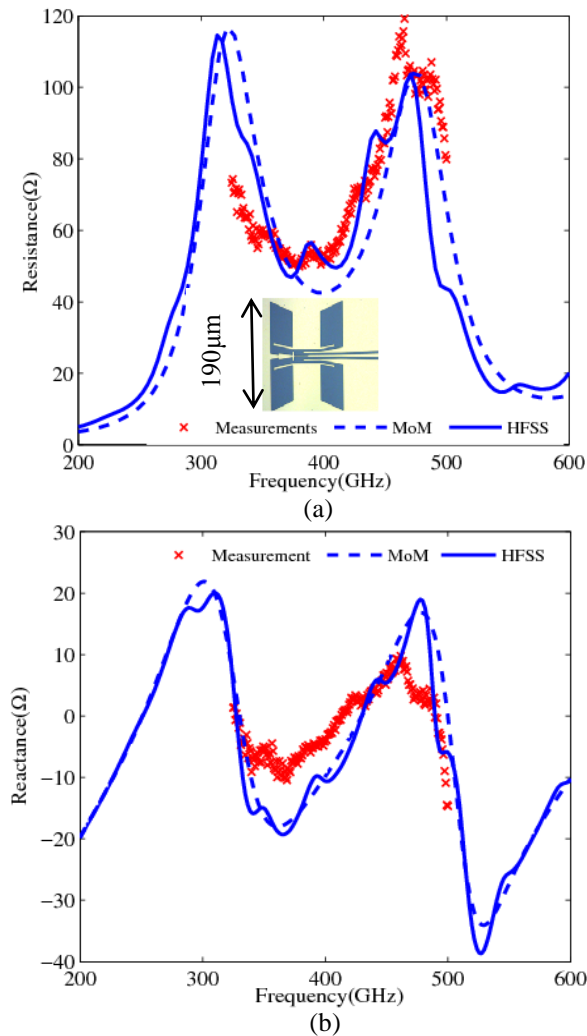
Fig. 4. Antenna impedance: (a) resistance of the non-contact probe antenna (with micrograph of fabricated antenna on inset), and (b) reactance of the non-contact probe antenna

V. CONCLUSION

We presented a hybrid electromagnetic modeling approach for accurate and efficient evaluation of non-contact probes for THz device characterization. The extremely-large computational cost of simulating the whole system has been significantly simplified by applying justified approximations. The proposed model brings together the principles from the RF/microwaves and optics regimes, and efficiently synergizes the two for modeling THz systems. This simple and accurate approach thus allows for a fast optimization of quasi-

optical signal coupling from the network analyzer to the device under test.

REFERENCES

[1] C. Caglayan, G. C. Trichopoulos, and K. Sertel, "Non-contact probes for on-wafer characterization of sub-millimeter wave devices and integrated circuits," *IEEE Transactions on Microwave Theory and Techniques*, vol. 62, no. 11, pp. 2791-2801, November 2014.

[2] G. C. Trichopoulos, G. Mumcu, K. Sertel, H. L. Mosbacker, and P. Smith, "A novel approach for improving off-axis pixel performance of terahertz focal plane arrays," *IEEE Transactions on Microwave Theory and Techniques*, vol. 58, no. 7, pp. 2014-2021, July 2010.

[3] G. C. Trichopoulos, H. L. Mosbacker, D. Burdette, and K. Sertel, "A broadband focal plane array camera for real-time THz imaging applications," *IEEE Transactions on Antennas and Propagation*, vol. 61, no. 4, pp. 1733,1740, April 2013.

[4] G. V. Eleftheriades and G. M. Rebeiz, "Self and mutual admittance of slot antennas on a dielectric half-space," *Journal of Infrared and Millimeter Waves*, vol. 14, no. 10, pp. 1925-1946, July 1993.

[5] K. Sertel and J. L. Volakis, *Integral Equation Methods for Electromagnetics*, Scitech Publishing Inc., 2012.

[6] D. F. Filipovic, S. S. Gearhart, and G. M. Rebeiz, "Double-slot antennas on extended hemispherical and elliptical silicon dielectric lenses," *IEEE Transactions on Microwave Theory and Techniques*, vol. 41, no. 10, pp. 1738-1749, October 1993.

[7] K. Wong, "Uncertainty analysis of the weighted least squares VNA calibration," *64th ARFTG Microwave Measurements Conference*, pp. 23-31, December 2004.

An Empirical Modeling of Electromagnetic Pollution on a University Campus

Çetin Kurnaz

Department of Electrical and Electronics Engineering
Ondokuz Mayıs University, 55139, Samsun, Turkey
ckurnaz@omu.edu.tr

Abstract ─ In this study, electric field strength (E) levels were measured on Ondokuz Mayıs University's Kurupelit Campus and Faculty of Medicine Hospital in Samsun, Turkey between years 2013-2015. 840 short term and two long term measurements were performed using PMM–8053 and SRM–3006 at 60 different locations of which 30 were on both the campus and hospital. The results show that the measured E levels are far below the limits that are determined by ICNIRP. Based on the measurement analysis, a novel empirical model that allows characterizing the total E of medium using three main electromagnetic (EM) sources with 99.7% accuracy was proposed. Then other new models to estimate main distribution of total E were suggested. With the use of these models, E values of main pollution sources can be estimated with 95.2% accuracy and easily lead to prediction of future EM pollution levels.

Index Terms ─ Electric field strength, electromagnetic (EM) measurement, EM pollution, statistical analysis.

I. INTRODUCTION

Electromagnetic waves are radiated from many sources, both natural and man-made, that produce electromagnetic pollution. Since the increase in the use of electromagnetic radiation (EMR) for communication such as radio, TV, wireless internet and cellular communication, the exposure levels of EMR have also increased. Growing demand for mobile communication and multimedia services pushes operators to expand the wireless network capabilities with additional base station installations. Because each base station is an EMR source, one cannot eliminate the exposure of EMR, whether one is a user of the system or not. Therefore, measuring and evaluating the environmental level of EMR, while also determining the detrimental effects of EMR on human health, become more crucial. Therefore, this topic is subject to ongoing research [1-6].

Although the wireless systems and base stations operate at frequencies below 300 GHz, which is within the non-ionizing spectrum, there has been much debate about their potential health effects. There are international standards and limits on the effects of EMR on human health. Each country has determined its own limits. The limits are recommended, with the assumption of 24 hour exposure, by the International Commission on Non-Ionizing Radiation Protection (ICNIRP), which is recognized by the World Health Organization (WHO) [7]. According to guidelines [7] by the ICINRP, the limit value of E at 900 MHz, 1800 MHz and 2100 MHz are 41(V/m), 57(V/m) and 61(V/m) respectively.

Although many factors can cause change in EMR, the number of users, line of sight (LOS), distance from a base station, and geographical structure of coverage area mainly affect EMR levels. Thus, measuring and evaluating the levels of EMR that cause pollution in crowded places where cellular systems are densely used has become of utmost importance. Therefore, in this study, EMR measurements were conducted at 60 different locations in Samsun Ondokuz Mayıs University's Kurupelit Campus and Faculty of Medicine Hospital over a two year period during various times of day. Statistical analysis of the measurement results were performed, then the distribution of each pollution source into the total E was determined.

II. MEASUREMENT OF EM POLLUTION

This study aims to observe the short and long term radiation levels in 100 kHz - 3 GHz frequency band EM sources on OMU's Kurupelit Campus and Faculty of Medicine Hospital, which is one of Turkey's largest university hospitals. The Kurupelit campus, which mainly consists of academic and administrative units, is established on an 8,800 acre field (Fig. 1 (a)). There are approximately 25,000 people on this campus per day, including students, academic and administrative personnel. The Faculty of Medicine Hospital consists of two main buildings, one for adult care and one for pediatric care, and have 11 and 4 floors respectively (Fig. 1 (b)). The hospital is visited by over 700,000 patients each year, equating to approximately 5,000 people (including patients and staff) per day.

Figure 1 (a) shows an aerial photo of the Kurupelit Campus. In the figure, the dashed line indicates Campus boundaries and each measurement location (L) is marked with a circle, while base stations (BS) are marked with

star. There are 13 base stations, of which three rest inside and ten rest outside of campus. The output power of the base stations vary from 10W to 40W. There are also over 200 indoor base stations whose powers vary between 0.13W and 1.34W in the hospital. Currently, there are three mobile communication operators in Turkey and all base stations on and/or outside of campus belong to the operators. Two of them use 900 MHz, and the other one uses 1800 MHz for 2G (GSM). Each operator uses 2100 MHz frequency band for 3G (UMTS).

In this study, EMR measurements were conducted between the years 2013-2015 at 60 different locations, of which 30 were on both the campus and hospital. These locations were chosen based on their distance to base stations on campus while different two locations on each floor of the Hospital. Total EMR in the band between 100 kHz – 3 GHz is measured with PMM–8053 with EP-330 isotropic electric field probe [8] while band selective are done with Narda SRM–3006 with 3501/03 isotropic electric field probe [9]. The duration of each measurement was six minutes. For each measurement, the maximum electric field strength (E_{max}) and average electric field strength (E_{avg}) were recorded.
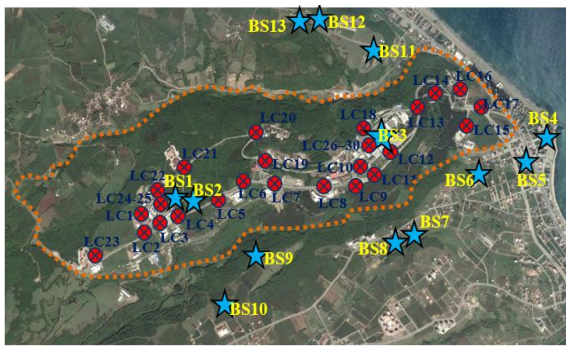
(a)

(b)

Fig. 1. (a) Kurupelit Campus, measurement locations and base stations, and (b) Faculty of Medicine Hospital.

III. MEASUREMENT RESULTS

The recorded E values through 840 short term measurements that were performed eight different times (on different days and hours) between the years 2013-2015 are shown in Fig. 2. In the figure, the measurement time represents the specific measurements dates (16.12.2013, 19.02.2014, 17.04.2014, 17.06.2014, 19.09.2014, 19.11.2014, 17.02.2015, 15.04.2015 for Campus respectively, while 25.12.2013, 21.04.2014, 26.08.2014, 24.12.2014 and 22.04.2015 for Hospital) mentioned. As seen in Fig. 2, E values may vary depending on measurement location and time. The following can be seen from the campus measurements: in the case of LOS, being close to the base station, e.g., location 24 (LC24, refers to 24th location on campus), gives rise to higher E levels of 3.60 V/m in the year 2015; the highest E_{avg} of 2.56 V/m was recorded at LC24 as expected; additionally, E_{max} and E_{avg} values were measured at 2.68 V/m and 1.95 V/m respectively in the hospital measurements at location 9 (LH9, refers to 9th location in the hospital).
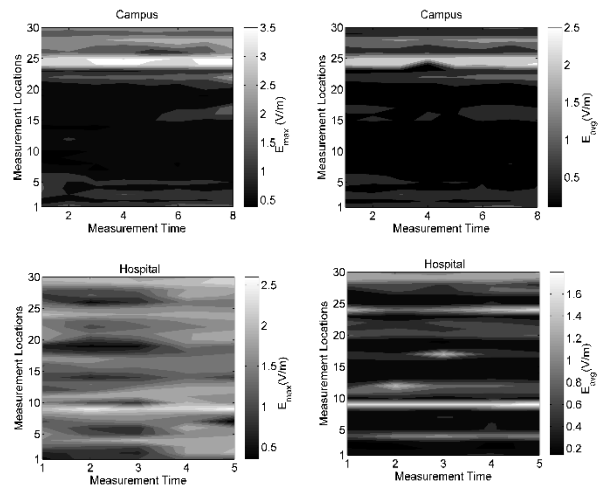
Fig. 2. E_{max}, E_{avg} values versus location for campus and hospital.

Statistical analysis of all the recorded Es were performed, and the maximum, mean values and standard deviations are given in Table 1.

Table 1: Statistical results of campus and hospital measurements

Location	Max.	Mean	Std.
Campus, E_{max}	3.60	1.284	0.828
Campus, E_{avg}	2.56	0.633	0.554
Hospital, E_{max}	2.68	1.509	0.447
Hospital, E_{avg}	1.95	0.574	0.417

Band selective measurements were done using SRM–3006 at all locations on campus and in the hospital. The maximum E strength was also obtained at LC24 on campus, while at LH9 in the hospital. The details of SRM–3006 measurements, which contain the E sources (service name, frequency ranges etc.) caused pollution at LC24 and LH9 as illustrated in Table 2. In

the Table, each E source has a specific index number and the 18th index represents E levels within undefined frequency bands. Total E (E_T) strength of medium is calculated as follows:

$$E_T = \sqrt{\sum_{i=1}^{18}(E_i)^2} ,\qquad (1)$$

where E_i is the electric field strength for ith band.

Table 2: Frequency selective E values for LC24 and LH9

Index	Service Name	Lower Frequency	Upper Frequency	Average E (mV/m)	
				LC24	LH9
1	Low Band	30 MHz	87.4 MHz	61.63	56.24
2	FM Band	87.5 MHz	108 MHz	40.34	80.99
3	Air Band	108.1 MHz	136 MHz	18.66	17.29
4	Land Band-I	136.1 MHz	173 MHz	18.61	17.35
5	TV VHF Band	173.1 MHz	230 MHz	20.01	17.94
6	Land Band-II	230.1 MHz	400 MHz	24.22	22.60
7	Land Band-III	400.1 MHz	470 MHz	13.40	12.64
8	TV UHF Band	470.1 MHz	861 MHz	54.46	37.01
9	ETC1	861.1 MHz	889.9 MHz	6.298	6.228
10	GSM 900	890 MHz	960 MHz	984.2	850.40
11	ETC2	960.1 MHz	1.7 GHz	30.9	30.15
12	GSM 1800	1.701 GHz	1.88 GHz	682.1	1007
13	DECT	1.881 GHz	1.899 GHz	5.746	5.345
14	UMTS 2100	1.9 GHz	2.17 GHz	1926	1259
15	ETC4	2.171 GHz	2.399 GHz	31.27	30.53
16	WLAN	2.400 GHz	2.483 GHz	21.83	36.83
17	ETC5	2.484 GHz	3.000 GHz	57.24	55.58
18	Others			4.882	4.706
19	Total			2.272 V/m	1.823 V/m

All band selective measurements on campus and in the hospital are shown in Fig. 3. In the figure, the 19th index presents E_T values of the medium. As seen in the figure, the sources that have the most contribution to E_T are GSM900, GSM1800 and UMTS2100. For simplicity, all service names' E value will be referred to with an index number (e.g., E_{10} for GSM900) throughout the rest of the paper. The maximum E value was recorded at LC24 as 2.272V/m. Distance from the base station (BS1 in Fig. 1 (a)) to LC24 approximately 100m and there is LOS between the units. In addition, the max E value of 1.823V/m was obtained at LH9 in the hospital, where most of the contributions were given by E_{10}, E_{12} and E_{14}.

All SRM–3006 measurements were analyzed and the max, mean and standard deviations were calculated as 2.27, 0.678 and 0.565 on campus, and 1.83, 0.602 and 0.501 for the hospital. In order to evaluate the change in E for a long-term time period, measurements were carried out at the locations (LC24, LH9) where the maximum Es were obtained. Two long term measurements

were started at 08.00 and stopped at 07.59 each day at a 4 sec. sampling period [5], and results were graphed in Fig. 4.

It is clearly seen from Fig. 4 (a), that the number of users affects E significantly. The max. E value was recorded as 4.20 V/m on campus during midday. After 16:00, when students started to leave campus, the E value decreased. It is also shown in the figure that at class break times, such as 10:00 and 11:00, the measured E levels increased. The E level dropped between 02:00 and 04:00, as the base stations does not fully operate. The min, mean and standard deviation of the measurement are 0.74 V/m, 1.324 V/m and 0.508. Long term E measurement results are given in Fig. 4 (b) for the hospital. There are no sudden fluctuations in E in the hospital as compared to Fig. 4 (a). Having constant visitors and patients because they are in service throughout the entire may be raised as a reason. The max., min, mean and standard deviation of the measurement are 2.38V/m, 1.03V/m, 1.378V/m and 0.229.
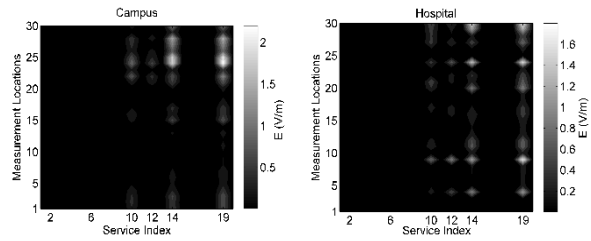
Fig. 3. Band selective E values for campus and hospital.
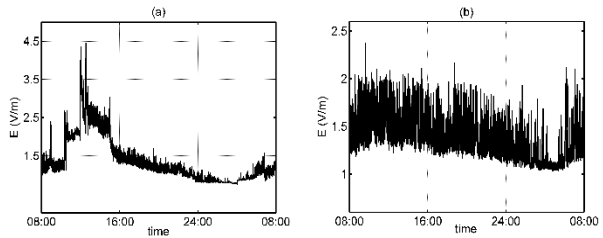
Fig. 4. Long term measurements for: (a) LC24 and (b) LH9.

IV. ANALYSIS

The measurement results for each pollution source were compared and their contributions to the combined E were analyzed. R^2 values, correlation coefficients between E_{19} and E_1-E_{18} and pie chart were used to determine the main E sources. As seen in Fig. 5 (a), E sources that have lower than 0.5 R^2 and correlation can be neglected. Furthermore, it is also seen in Fig. 5 (b) that basic E sources are E_{10}, E_{12} and E_{14} to a significant percentage (98%). On this basis, E_{10}, E_{12} and E_{14} can be determined as the main sources of pollution.
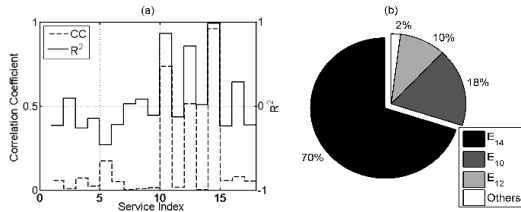
Fig. 5. (a) Correlation coefficient (CC) and R^2 values, and (b) the pie chart of E.

To model total E in medium with E_{10}, E_{12} and E_{14} multilinear regression [10] was applied and total EMR was defined ($\hat{E}_T$) as in Eq. 2:

$$\hat{E}_T = \sqrt{0.0157 + 0.9895E_{10}^2 + 1.0122E_{12}^2 + 1.0015E_{14}^2}. \quad (2)$$

The performance of the method was compared in terms of Normalized Root Mean Square Error (NRMSE), which is defined by the following:

$$NRMSE = \frac{\sqrt{\dfrac{1}{N}\sum_{i=1}^{N}(E_{T,i} - \hat{E}_{T,i})^2}}{\max(E_T) - \min(E_T)}, \quad (3)$$

where $E_{T,i}$ is actual E values, $\hat{E}_{T,i}$ is estimated E, i is measurement location, and N is the number of total measurement locations. The NRMSE is 0.0023 between E_T and $\hat{E}_T$.

Since determining the distribution of total E needs specific band selective EMR meter, which is not generally accessible, calculating the main pollution source from the total becomes more crucial. For this reason, linear regression [10] was applied to the same data and the estimated E_{10} ($\hat{E}_{10}$) was calculated easily with the use of Eq. 4. The NRMSE between E_{10} and $\hat{E}_{10}$ is 0.1187:

$$\hat{E}_{10} = \sqrt{0.0202 + 0.1508E_T^2}. \quad (4)$$

Similarly $\hat{E}_{12}$ and $\hat{E}_{14}$ can be estimated by using the following equations. The corresponding NRMSEs are 0.1238 and 0.0480:

$$\hat{E}_{12} = \sqrt{-0.0017 + 0.1006E_T^2}, \quad (5)$$

$$\hat{E}_{14} = \sqrt{-0.0339 + 0.7478E_T^2}. \quad (6)$$

For E_{14}, the reason for yielding the highest accuracy was having the highest correlation (0.95), while for E_{12} low correlation (0.52) led lower accuracy.

V. CONCLUSION

In this study, EMR levels in Samsun Ondokuz Mayıs University's Kurupelit Campus and Faculty of Medicine Hospital were measured between years 2013 and 2015, and the values were compared with limits determined by ICNIRP. The maximum measured E value was 4.20 V/m for all medium. Comparing this value with the limit shows that there is not significant electromagnetic pollution in Kurupelit Campus and the hospital. The results also show that measured E vary by time and an increase in number of users cause significant increase in E levels. Based on band selective measurements and statistical analysis main reason of EM pollution is determined as UMTS2100. A novel empirical model was proposed for characterizing the total E of medium with 99.7% accuracy. In order to predict the band selective E values from the total E; other new models were suggested. Using these models allow determining each main sources' E and they can be calculated without using any band selective EMR meter.

REFERENCES

[1] A. Mousa, "Electromagnetic radiation measurements and safety issues same cellular base stations in Nablus," *Journal of Engineering Science and Technology Review*, vol. 4, no. 1, pp. 35-42, 2011.

[2] O. Genç, M. Bayrak, and E. Yaldız, "Analysis of the effects of GSM bands to the electromagnetic pollution in the RF spectrum," *Progress in Electromagnetics Research*, vol. 101, pp. 17-32, 2010.

[3] B. K. Gül, Ç. Kurnaz, and B. K. Engiz, "Measurement and evaluation of electromagnetic pollution in Ondokuz Mayıs University Kurupelit Campus in Samsun, Turkey," *Third International Conference on Advances in Information Processing and Communication Technology*, pp. 80-84, Rome, Italy, 2015.

[4] S. Miclaus and P. Bechet, "Estimated and measured values of the radiofrequency radiation power density around cellular base stations," *Environment Physics*, vol. 52, no. 3-4, pp. 429-440, 2007.

[5] L. Seyfi, "Measurement of electromagnetic radiation with respect to the hours and days of a week at 100kHz–3GHz frequency band in a Turkish dwelling," *Measurement*, vol. 46, no. 9, pp. 3002-3009, 2013.

[6] P. Baltrenas and R. Buckus, "Measurements and analysis of the electromagnetic fields of mobile communication antennas," *Measurement*, vol. 46, no. 10, pp. 3942-3949, 2013.

[7] ICNIRP Guidelines, "Guidelines for Limiting Exposure to Time-Varying Electric, Magnetic, and Electromagnetic Fields (up to 300 GHz)," International Commission on Non-Ionizing Radiation Protection, Health Physics, vol. 74, no. 4, pp. 494-522, 1998.

[8] www.pmm.it/docs/8053en1001.pdf

[9] www.narda-ts.us/pdf_files/DataSheets/SRM3006_DataSheet.pdf

[10] S. H. Brown, "Multiple linear regression analysis: a matrix approach with MATLAB," *Alabama Journal of Mathematic*, vol. 34, pp. 1-3, 2009.

A Planar NF–FF Transformation for Quasi-Spherical Antennas using the Innovative Spiral Scanning

F. D'Agostino, F. Ferrara, C. Gennarelli, R. Guerriero, and M. Migliozzi

Dipartimento di Ingegneria Industriale
University of Salerno, via Giovanni Paolo II, 132 - 84084 Fisciano, Italy
fdagostino@unisa.it, flferrara@unisa.it, cgennarelli@unisa.it, rguerriero@unisa.it, mmigliozzi@unisa.it

Abstract ─ An effective probe compensated near-field–far-field (NF–FF) transformation with planar spiral scanning, using a minimum number of NF data, has been experimentally validated. It allows a remarkable measurement time saving, due to the continuous movements of the positioning systems and to the reduced number of needed NF data. Such a technique is based on a nonredundant sampling representation of the voltage acquired by the probe, obtained by using the theoretical foundations of the NF–FF transformations with spiral scans for quasi-spherical antennas. Then, the NF data needed by the plane-rectangular NF–FF transformation are efficiently recovered from those acquired along the spiral, via an optimal sampling interpolation formula.

Index Terms ─ Antenna measurements, near-field – far-field transformation techniques, nonredundant sampling representations, planar spiral scanning.

I. INTRODUCTION

As well-known, near-field–far-field (NF–FF) transformation techniques [1] are widely used to accurately reconstruct the far field radiated by electrically large antennas from NF measurements carried out in an anechoic chamber. Among these techniques, those adopting the planar scannings [2-6] are particularly suitable for high gain antennas radiating pencil beam patterns. Nowadays, one of the hottest topics concerning the NF–FF transformations is the reduction of the measurement time, that is currently very much greater than the computational one. To this end, the nonredundant sampling representations of electromagnetic (EM) fields [7, 8] have been properly used in [3, 4] and [6] to remarkably reduce the number of NF measurements in the plane-rectangular [2] and plane-polar scanning [5], respectively. Another convenient way to reduce the measurement time is, as suggested in [9], the use of NF–FF transformations employing the planar spiral scanning [9-14], which makes faster the NF data acquisition, since it is executed on fly through a continuous linear movement

of the probe and a synchronized rotational one of the antenna under test (AUT). Among them, those [11-14] relying on the nonredundant sampling representations of EM fields are even more effective from the measurement time reduction point of view, due to the lower number of NF data and spiral turns. In particular, the two-dimensional nonredundant representation for the voltage measured by the probe on the plane has been obtained by assuming the AUT as enclosed in the smallest sphere and oblate ellipsoid containing it in [11, 12] and [13, 14], respectively. In both the cases, optimal sampling interpolation (OSI) expansions are used to efficiently recover the data needed by the classical plane-rectangular NF–FF transformation [2] from the nonredundant ones collected along the spiral. Recently, NF–FF transformation techniques with helicoidal and spherical spiral scannings have been also proposed. The interested reader can refer to [15] for a complete bibliography.

The aim of this paper is to provide the experimental assessment of the NF–FF transformation with planar spiral scanning [11] using a ball for modelling volumetric (i.e., quasi-spherical) antennas.

II. NONREDUNDANT PROBE VOLTAGE REPRESENTATION ON A PLANE

Let us consider a quasi-spherical AUT, enclosed in the smallest sphere of radius a able to contain it, and a nondirective probe scanning a spiral lying on a plane at a distance d from the AUT centre. Moreover, let us adopt the spherical coordinate system (r, ϑ, φ) to denote an observation point P (Fig. 1). The voltage measured by such a probe has the same effective spatial bandwidth of the AUT field and, hence, the nonredundant sampling representations of EM fields [7] can be applied to it. Accordingly, to get an effective voltage representation along a curve C lying on the plane, it is convenient to adopt a proper parameter η for describing C and to introduce the "reduced voltage" $\tilde{V}(\eta) = V(\eta)\,e^{j\psi(\eta)}$, where $\psi(\eta)$ is a proper phase function and $V(\eta)$ is the voltage V_φ or V_ρ measured by the probe or by the rotated probe, (ρ, φ) being the polar coordinates on the

plane. The bandlimitation error, occurring when $\tilde{V}(\eta)$ is approximated by a bandlimited function, is negligible as the bandwidth exceeds a critical value W_η [7] and, thus, it can be controlled by choosing the bandwidth equal to $\chi'W_\eta$, $\chi'>1$ being the enlargement bandwidth factor.
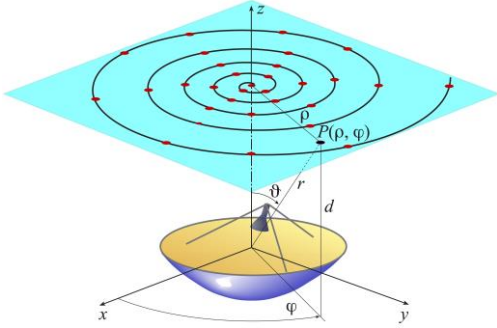

Fig. 1. Planar spiral scanning.

According to the theoretical results on the NF–FF transformations with spiral scannings for quasi-spherical antennas [12], the two-dimensional OSI expansion, for reconstructing the voltage on the plane from a nonredundant number of its samples collected along the spiral, can be rigorously obtained by choosing the spiral in such a way that its pitch be equal to the sample spacing needed for the interpolation along a radial line and developing a nonredundant sampling representation along the spiral. The bandwidth, the parameter relevant to a radial line, and the related phase function are [7, 12]:

$$W_\eta = \beta a \; ; \qquad \eta = \vartheta \, , \qquad (1)$$

$$\psi = \beta\sqrt{r^2 - a^2} - \beta a \cos^{-1}(a/r) \, , \qquad (2)$$

β being the free-space wavenumber.

The sample spacing for the radial line interpolation and, as a consequence, the pitch of the spiral is then $\Delta\vartheta = 2\pi/(2N''+1)$, where $N'' = \text{Int}(\chi N')+1$, $\text{Int}(x)$ denotes the integer part of x, $N' = \text{Int}(\chi'\beta a)+1$, and $\chi > 1$ is an oversampling factor, which controls the truncation error [7]. Accordingly, the equations of the spiral are:

$$\begin{cases} x = d\tan\theta\cos\phi = \rho\cos\phi \\ y = d\tan\theta\sin\phi = \rho\sin\phi \\ z = d \end{cases} , \qquad (3)$$

where ϕ is the angular parameter describing the spiral. Moreover, the condition on the spiral pitch implies that $\theta = k\phi$, with $k = 1/(2N''+1)$ [12]. It is noteworthy that θ, unlike the zenithal angle ϑ, can take also negative values and that, when the spiral crosses the pole, the azimuthal angle φ has a discontinuity jump of π, while the spiral angle ϕ is continuous. Note that such a spiral can be viewed as obtained by radially projecting on the plane a proper spiral wrapping the sphere modelling the AUT.

As regards the nonredundant sampling representation along the spiral, it has been rigorously shown, in [11] for the planar spiral and in [12] for a spiral wrapping a quite arbitrary rotational surface, that the expressions of the phase function γ and of the parameter ξ are:

$$\gamma = \psi \; ; \qquad \xi = \frac{\beta a}{W_\xi}\int_0^\phi \sqrt{k^2 + \sin^2 k\phi'}\, \mathrm{d}\phi' \, . \qquad (4)$$

Accordingly, the parameter ξ is β/W_ξ times the curvilinear abscissa of the projecting point lying on the spiral that wraps the modelling sphere. The bandwidth W_ξ can be determined in such a way that the angle-like parameter ξ covers a 2π range when the whole projecting spiral on the sphere is described. As a consequence,

$$W_\xi = \frac{\beta a}{\pi}\int_0^{(2N''+1)\pi} \sqrt{k^2 + \sin^2 k\phi'}\, \mathrm{d}\phi' \cdot \qquad (5)$$

In light of the above results, the reduced voltage at the point P on the radial line at φ can be reconstructed by the following OSI expansion [11, 12]:

$$\tilde{V}(\vartheta, \varphi) = \sum_{n=n_0-q+1}^{n_0+q} \tilde{V}(\vartheta_n)\,\Omega_N(\vartheta-\vartheta_n, \bar{\vartheta})\,D_{N''}(\vartheta-\vartheta_n) \, , \quad (6)$$

wherein $2q$ is the number of the retained intermediate samples $\tilde{V}(\vartheta_n)$, namely, the reduced voltage values at the intersection points between the spiral and the radial line through P, $n_0 = \text{Int}[(\vartheta-\vartheta_0)/\Delta\vartheta]$, $N = N''-N'$, $\bar{\vartheta} = q\Delta\vartheta$, and

$$\vartheta_n = \vartheta_n(\varphi) = k\varphi + n\Delta\vartheta = \vartheta_0 + n\Delta\vartheta \, . \qquad (7)$$

Moreover,

$$D_{N''}(\vartheta) = \frac{\sin\big((2N''+1)\vartheta/2\big)}{(2N''+1)\sin(\vartheta/2)} \, , \qquad (8)$$

$$\Omega_N(\vartheta, \bar{\vartheta}) = \frac{T_N\big[-1 + 2\big(\cos(\vartheta/2)/\cos(\bar{\vartheta}/2)\big)^2\big]}{T_N\big[-1 + 2/\cos^2(\bar{\vartheta}/2)\big]} \, , \quad (9)$$

are the Dirichlet and Tschebyscheff sampling functions [7], where $T_N(\vartheta)$ is the Tschebyscheff polynomial of degree N.

The following OSI expansion along the spiral [11, 12] allows one to recover the intermediate samples:

$$\tilde{V}(\xi(\vartheta_n)) = \sum_{m=m_0-p+1}^{m_0+p} \tilde{V}(\xi_m)\,\Omega_M(\xi-\xi_m, \bar{\xi})\,D_{M''}(\xi-\xi_m), (10)$$

where $m_0 = \text{Int}[\xi(\vartheta_n)/\Delta\xi]$, $2p$ is the number of the retained samples, $M = M''-M'$, $\bar{\xi} = p\Delta\xi$, and

$$\xi_m = m\Delta\xi = 2\pi m/(2M''+1) \, , \qquad (11)$$

with $M'' = \text{Int}[\chi M']+1$ and $M' = \text{Int}[\chi'W_\xi]+1$.

Since small variations of ξ correspond to large changes of φ in the neighbourhood of the pole ($\vartheta = 0$), it is necessary to properly increase the factor χ' to avoid a significant growth of the bandlimitation error, when interpolating the voltage in this zone [11, 12].

It is so possible to accurately recover the voltages V_φ and V_ρ, acquired by the probe and rotated probe, at

the points required by the classical plane-rectangular NF–FF transformation [2]. Unfortunately, the probe corrected formulas in [2] (whose expressions in the here considered reference system can be found in [11]) are valid only if the probe maintains its orientation with respect to the AUT and this requires its co-rotation with it. To avoid such a co-rotation, a probe exhibiting only a first-order azimuthal dependence in its radiated far field can be used. In fact, in such a case, the voltages V_V and V_H (acquired by the probe and rotated probe with co-rotation) can be determined from V_φ and V_ρ via the relations:

$$V_V = V_\varphi \cos\varphi - V_\rho \sin\varphi \; ; \; V_H = V_\varphi \sin\varphi + V_\rho \cos\varphi . \quad (12)$$

III. EXPERIMENTAL ASSESSMENT

In this section, some experimental results assessing the effectiveness of the described NF–FF transformation are shown. The tests have been performed in the anechoic chamber of the Antenna Characterization Lab of the University of Salerno, which is equipped with a plane-polar NF facility, besides the cylindrical and spherical ones. The amplitude and phase measurements are performed by using a vector network analyzer. The planar scanning is accomplished by mounting the AUT on a roll positioner and anchoring the probe (an open-ended WR90 rectangular waveguide) to a vertical scanner. The antenna employed in the experimental tests is a H-plane monopulse antenna, working in the sum mode at 10 GHz, located in the plane $z = 0$, and built by using a hybrid Tee and two pyramidal horns, whose apertures (8.9×6.8 cm sized) are at a distance of 26 cm between their centers. It has been modelled by a ball of radius $a = 18.0$ cm. The NF data are acquired along a spiral covering a circular zone of radius 110 cm on a plane at distance $d = 50.5$ cm from the AUT. The amplitudes of the recovered voltages V_φ and V_ρ relevant to the radial lines at $\varphi = 0°$ and $\varphi = 30°$ are compared in Figs. 2 and 3 with those directly measured. For completeness, the comparison between the recovered phase of V_φ on the radial line at $\varphi = 0°$ and the directly measured one is also shown in Fig. 4. As can be seen, the reconstructions are very good, save for the zones characterized by very low voltage levels. These reconstructions have been obtained by choosing $\chi = 1.20$ and $p = q = 7$ to ensure a truncation error smaller than the measurement one [11]. Moreover, to make the aliasing error negligible, χ' has been chosen equal to 1.35, save for the zone of the spiral determined by the 24 samples centred on the pole, wherein it has been increased in such a way that the sample spacing is reduced by a factor 9.

At last, the FF patterns in the principal planes E and H, reconstructed from the NF data acquired along the spiral, are compared in Figs. 5 and 6 with those recovered via the classical cylindrical NF–FF transformation. As can be seen, a very good agreement results.

Note that the number of used spiral samples is 1 767 (1 575 regular + 192 extra samples) much smaller than those 21 609 and 33 581 needed by the classical plane-rectangular [2] and the Rahmat-Samii's plane-polar [5] NF–FF transformations, respectively.

Fig. 2. Amplitudes of V_φ and V_ρ on the radial line at $\varphi = 0°$. Solid line: measured. Dashes: reconstructed from the NF data acquired along a spiral.
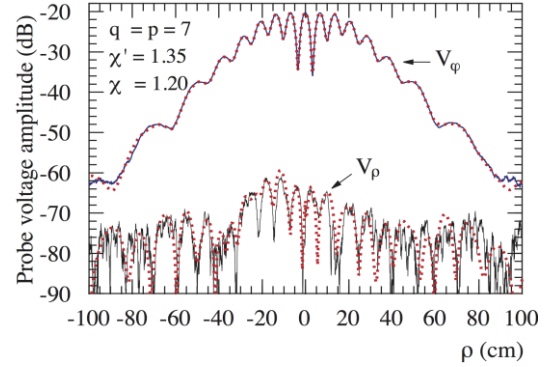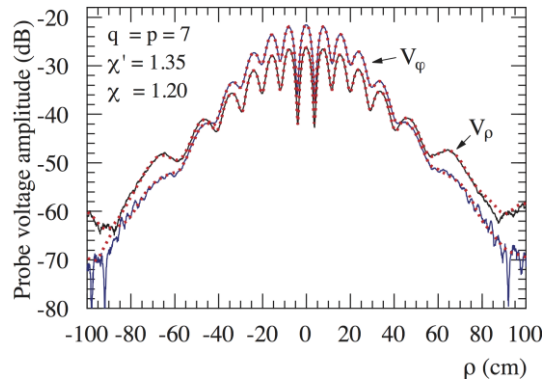

Fig. 3. Amplitudes of V_φ and V_ρ on the radial line at $\varphi = 30°$. Solid line: measured. Dashes: reconstructed from the NF data acquired along a spiral.
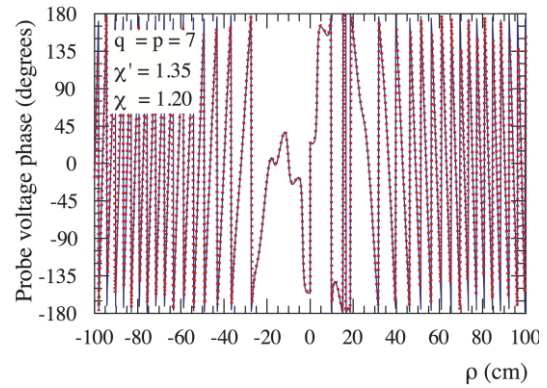

Fig. 4. Phase of V_φ on the radial line at $\varphi = 0°$. Solid line: measured. Dashes: reconstructed from the NF data acquired along a spiral.
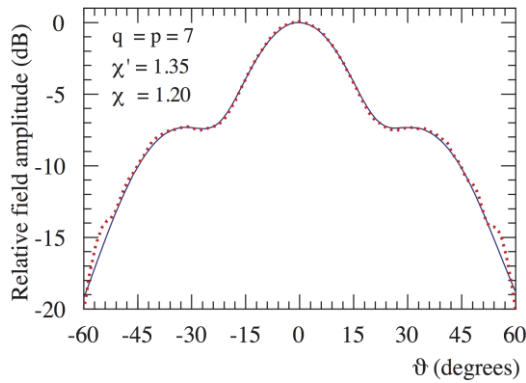
Fig. 5. E-plane pattern. Solid line: reconstructed from cylindrical NF data. Dashes: reconstructed from the NF data acquired along a spiral.
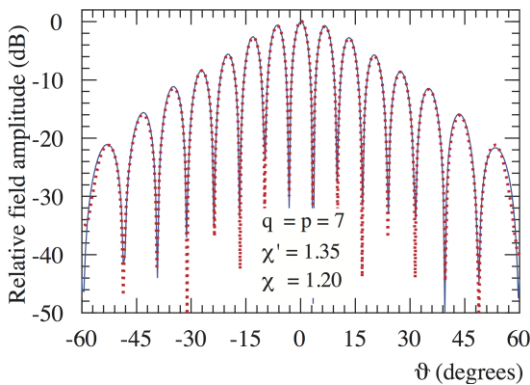

Fig. 6. H-plane pattern. Solid line: reconstructed from cylindrical NF data. Dashes: reconstructed from the NF data acquired along a spiral.

IV. CONCLUSION

An experimental validation of the described NF–FF transformation with planar spiral scan has been provided. The very good agreement found in the NF reconstructions, as well as that resulting from the comparison between the recovered FF patterns and those obtained by employing the cylindrical scanning, have fully confirmed its effectiveness also from the experimental viewpoint.

REFERENCES

[1] M. H. Francis, Ed., *IEEE Recommended Practice for Near-Field Antenna Measurements*, IEEE Standard 1720-2012.

[2] E. B. Joy, W. M. Leach, G. P. Rodrigue, and D. T. Paris, "Applications of probe-compensated near-field measurements," *IEEE Trans. Antennas Prop.*, vol. AP-26, pp. 379-389, May 1978.

[3] F. Ferrara, C. Gennarelli, R. Guerriero, G. Riccio, and C. Savarese, "An efficient near-field to far-field transformation using the planar wide-mesh scanning," *Jour. Electr. Waves Appl.*, vol. 21, pp. 341-357, 2007.

[4] F. D'Agostino, I. De Colibus, F. Ferrara, C. Gennarelli, R. Guerriero, and M. Migliozzi, "Far-field pattern reconstruction from near-field data collected via a nonconventional plane-rectangular scanning: Experimental testing," *Int. Jour. Antennas Prop.*, vol. 2014, ID 763687, 9 pages, 2014.

[5] M. S. Gatti and Y. Rahmat-Samii, "FFT applications to plane-polar near-field antenna measurements," *IEEE Trans. Antennas Prop.*, vol. 36, pp. 781-791, June 1988.

[6] O. M. Bucci, C. Gennarelli, G. Riccio, and C. Savarese, "Near-field–far-field transformation from nonredundant plane-polar data: effective modellings of the source," *IEE Proc. Microw. Antennas Prop.*, vol. 145, pp. 33-38, Feb. 1998.

[7] O. M. Bucci, C. Gennarelli, and C. Savarese, "Representation of electromagnetic fields over arbitrary surfaces by a finite and non redundant number of samples," *IEEE Trans. Antennas Prop.*, vol. 46, pp. 351-359, Mar. 1998.

[8] O. M. Bucci and C. Gennarelli, "Application of nonredundant sampling representations of electromagnetic fields to NF-FF transformation techniques," *Int. Jour. Antennas Prop.*, vol. 2012, ID 319856, 14 pages, 2012.

[9] R. G. Yaccarino, L. I. Williams, and Y. Rahmat-Samii, "Linear spiral sampling for the bipolar planar antenna measurement technique," *IEEE Trans. Antennas Prop.*, vol. 44, pp. 1049-1051, 1996.

[10] S. Costanzo and G. Di Massa, "Near-field to far-field transformation with planar spiral scanning," *Prog. in Electr. Res.*, vol. 73, pp. 49-59, 2007.

[11] O. M. Bucci, F. D'Agostino, C. Gennarelli, G. Riccio, and C. Savarese, "Probe compensated far-field reconstruction by near-field planar spiral scanning," *IEE Proc. Microw. Antennas Prop.*, vol. 149, pp. 119-123, Apr. 2002.

[12] F. D'Agostino, C. Gennarelli, G. Riccio, and C. Savarese, "Theoretical foundations of near-field–far-field transformations with spiral scannings," *Prog. in Electr. Res.*, vol. 61, pp. 193-214, 2006.

[13] F. D'Agostino, F. Ferrara, C. Gennarelli, R. Guerriero, M. Migliozzi, "An effective NF-FF transformation technique with planar spiral scanning tailored for quasi-planar antennas," *IEEE Trans. Antennas Prop.*, vol. 56, pp. 2981-2987, 2008.

[14] F. D'Agostino, F. Ferrara, C. Gennarelli, R. Guerriero, and M. Migliozzi, "The unified theory of near-field–far-field transformations with spiral scannings for nonspherical antennas," *Prog. in Electr. Res. B*, vol. 14, pp. 449-477, 2009.

[15] R. Cicchetti, F. D'Agostino, F. Ferrara, C. Gennarelli, R. Guerriero, and M. Migliozzi, "Near-field to far-field transformation techniques with spiral scannings: A comprehensive review," *Int. Jour. Antennas Prop.*, vol. 2014, ID 143084, 2014.

Gradient-Based Near-Field Antenna Characterization in Planar Geometry

Amedeo Capozzoli, Claudio Curcio, and Angelo Liseno

Dipartimento di Ingegneria Elettrica e delle Tecnologie dell'Informazione
Università di Napoli Federico II, via Claudio 21, 80125, Napoli, Italia
a.capozzoli@unina.it, clcurcio@unina.it, angelo.liseno@unina.it

Abstract ─ A near field characterization technique, based on the optimization of the Singular Value Behavior, is here accelerated by using the analytical expression of the gradient of the relevant objective functional. This solution allows to conveniently tackle the cases of electrically large antennas.

Index Terms ─ Antenna measurements, near field/far field transformation, planar scanning, probe compensation, singular values.

I. INTRODUCTION

The Near-Field (NF) antenna characterization amounts to estimate the Far Field Pattern (FFP) of an Antenna Under Test (AUT), from field data measured in the NF zone [1]. Amplitude and phase or phaseless [2-4] measurements can be exploited; standard metallic or photonic probes can be adopted [5].

In [2-5], the NF characterization has been formulated as a regularized linear inverse problem, outperforming other approaches in terms of number of samples and path length of the scanning curve. The approach has been applied to the canonical scanning geometries in the case of aperture antennas [2-7].

In particular, the number M and the distribution of the field samples (DFS) are determined after a proper optimization procedure improving as much as possible the degree of conditioning of the problem. The procedure is based on the Singular Value (SV) decomposition of the relevant discretized linear operator and on the concept of Singular Value Behavior (SVB) optimization. The DFS and M are determined by means of an iterative process wherein, from one iteration to the next, M is progressively enlarged. At each step, and for a fixed number of samples, the DFS is found as the one optimizing a functional measuring the SVB of the relevant linear operator. The process ends when a saturation behavior of the optimized functional values is observed [2,3]. Given the DFS, the aperture field, and the FFP, can be obtained from the measurements, after a regularized inversion. For electrically large antennas the whole procedure can be accelerated to keep low the computing time required to tackle the optimization.

The crucial steps are:
- Filling the matrix $\underline{T}$ representing the discretized version of the linear operator;
- Calculating the SV Decomposition (SVD) of T;
- Optimizing the SVB of T.

As long as a local tool is deemed adequate to optimize the SVB of $\underline{T}$, it is convenient to exploit an algorithm of the quasi-Newton class. Obviously, the gradient must be available either in analytical or numerical form. This second option typically burdens even more the calculation, since it requires a repeated functional evaluation. In this sense, exploiting the expertise drawn from the computational world becomes crucial to make the method practically feasible for electrically large antennas, showing how the two worlds of measurements and computation can profit of each other to produce unprecedented results.

With particular reference to this paper, we show which beneficial effects an optimization algorithm based on the analytical evaluation of the gradient can achieve in terms of execution time. The case of aperture antennas is here dealt with, in the planar scanning geometry, wherein probe compensation is explicitly considered.

II. THE NFFF TRANSFORMATION

Let us consider an aperture AUT having a $2a_{ap} \times 2b_{ap}$ sized rectangular effective aperture $\mathcal{A}$, centered in x-y plane of the Oxyz reference system (see Fig. 1), and let us denote with $\underline{E}_a$ the aperture field (tangential components). Furthermore, let us assume that the samples of the field radiated by the AUT are collected over a planar surface $\mathcal{D}$ bounded by a $2a \times 2b$ sized rectangle, located at a distance z_0 from $\mathcal{A}$. The parameters a and b are defined according to dimensions of the available scanning system.

The method calculates the FFP given $\underline{E}_a$. This, in turn, is determined starting from the measured field on $\mathcal{D}$, by solving a linear inverse problem, defined by a linear operator, say $\mathcal{T}$, mapping $\underline{E}_a$ onto the measured voltages V on $\mathcal{D}$. The numerical inversion of $\mathcal{T}$ requires its discrete counterpart, determined by considering the smallest finite dimensional functional subspace containing

the relevant functional component of $\underline{E}_a$. After this, discretization is obtained by:

- Expanding Ea by means of an orthonormal basis of the functional subspace above [2-4];
- Considering the measured voltages Vm at the M sampling points, whose coordinates are (xm,ym,z0);

And so the problem turns into its algebraic counterpart, which can be written as:

$$\underline{Y} = \underline{T}\,\underline{X}, \tag{1}$$

where $\underline{Y}$ is the vector containing the measured voltages, $\underline{X}$ is the vector containing the unknown expansion coefficients of $\underline{E}_a$, and $\underline{T}$ is the matrix representing the discrete counterpart of the operator $\mathcal{T}$. To calculate $\underline{E}_a$ is equivalent to determine $\underline{X}$ from $\underline{Y}$ by solving the linear system in Eq. (1). Obviously a regularization strategy is needed to circumvent the ill-conditioning of $\underline{T}$. In the following Eq. (1) will be detailed for the case of a scalar problem, with a linearly polarized aperture field $\underline{E}_a = E_a \hat{\imath}_y$, and standard open-ended waveguide (OEWG) probe, assumed to be linearly polarized and oriented along $\hat{\imath}_y$, assuming negligible the x-component of the probe response.

Accordingly, the voltage V_m measured at the m-th measurement point (x_m, y_m, z_0) can be written as [2,3]:

$$V_m = \frac{1}{z_0} \int_{-a_{ap}}^{a_{ap}} \int_{-b_{ap}}^{b_{ap}} l(x_m, y_m, x', y') h_y E_a \, dx' dy', \tag{2}$$

where $\beta = 2\pi/\lambda$, λ being the wavelength, $l(x,y,x',y') = g(y,y')f(R)$ where $g = g(y,y') = [z_0^2 + (y - y')^2]$, R is given by:

$$R = \sqrt{(x - x')^2 + (y - y')^2 + z_0}, \tag{3}$$

and

$$f(R) = \frac{1}{2\pi}\left(\frac{j\beta}{R} + \frac{1}{R^2}\right)\frac{e^{-i\beta R}}{R}, \tag{4}$$

and $h_y = h_y(x,y,x',y')$ is the y-component of the probe response, in the reference system Oxyz, and $E_a = E_a(x',y')$. Regarding E_a, as in [2,3] it is expanded by using the visible Prolate Spheroidal Wave Functions (PSWF) [8], so to take into account for the geometry of the aperture and for the obvious assumption of non-superdirective source. In this way, E_a is written as:

$$E_a(x,y) = \sum_{p=1}^{P}\sum_{q=1}^{Q} \alpha_{pq}\Lambda_p(c_x, x)\Lambda_q(c_y, y), \tag{5}$$

where $\Lambda_i[c_w, w]$ is the i-th, 1D PSWF with "space-bandwidth product" c_w [8], $c_x = a_{ap}u'$, $c_y = b_{ap}v'$ and u' and v' locate the spectral region of interest [8], as $u' \le \beta$ and $v' \le \beta$, P=Int[$4a_{ap}/\lambda$] and Q=Int[$4b_{ap}/\lambda$], Int[•] denoting the integer part of its argument.

Accordingly, $\underline{X}$ is a vector of S=PQ elements containing the expansion coefficients $\alpha_{p(s)q(s)}$, where p(s) and q(s) map the index s into the corresponding PSWF indices p and q, while $\underline{T}$ is an MxS matrix whose entries are given by:

$$\frac{1}{z_0}\int_{-a_{ap}}^{a_{ap}}\int_{-b_{ap}}^{b_{ap}} l h_y \Lambda_{p(s)}(c_x, x')\Lambda_{q(s)}(c_y, y')\,dx'dy', \tag{6}$$

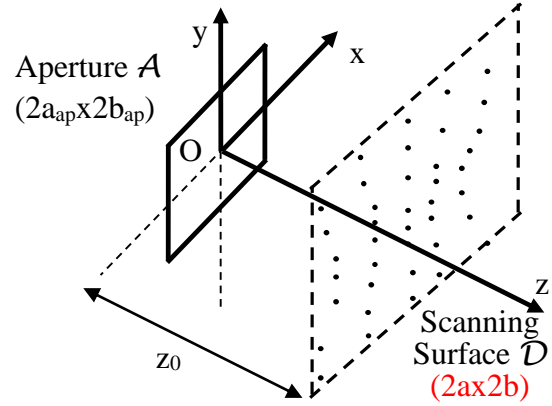where both l and h_y are evaluated at the m-th observation point (x_m, y_m).

Fig. 1. Geometry of the problem.

III. GRADIENT-BASED OPTIMIZATION PROCEDURE

The DFS and M are obtained via a SVB optimization, according to the procedure in [2,3] based on the maximization of the functional:

$$\Xi = \sum_{k=1}^{K}\frac{\sigma_k}{\sigma_1}, \tag{7}$$

where σ_k are the K singular values of the matrix $\underline{T}$, ordered in decreasing order. As shown in [2,3], to keep low the number of unknowns, it is convenient to adopt a proper representation of the measurement point locations. In particular, the sampling points can be determined by starting from an auxiliary uniform Cartesian grid (ξ_m, η_m) by means of a couple of "distortion" mappings, say w_x and w_y, to be determined. Accordingly:

$$\begin{cases} x_m = w_x(\xi_m, \eta_m) \\ y_m = w_y(\xi_m, \eta_m) \end{cases}, \tag{8}$$

where w_x and w_y are represented by means of W basis functions (e.g., polynomials), say τ^x and τ^y, respectively:

$$\begin{cases} w_x(\xi_m, \eta_m) = \sum_{r=1}^{W}\chi_r\,\tau_r^x(\xi_m, \eta_m) \\ w_y(\xi_m, \eta_m) = \sum_{r=1}^{W}\chi_{r+W}\,\tau_r^y(\xi_m, \eta_m) \end{cases}. \tag{9}$$

And so, for a given M, the unknowns turn to be the coefficients χ_r, and the measurement points are determined as the ones maximizing Ξ. The effective and efficient maximization of Ξ is crucial to make the procedure successful.

Among the quasi-Newton class local tools, a very widespread choice if the the Broyden-Fletcher-Goldfarb-Shanno (BFGS) scheme [9]. Given a function f($\underline{x}$) to be optimized, where $\underline{x}$ is the vector of the unknown parameters, the solution at each iteration is obtained by exploiting the expression of the gradient ∇f and an approximate inverse of the Hessian matrix $\underline{H}$, obtained by an update formula based on the f and ∇f evaluation at the current and preceding iteration. Two options are available. The first estimates ∇f numerically and can be very time consuming, especially for large problems and

computationally burdened f. The second analytically evaluates ∇f and typically gives better results in terms of accuracy and computational complexity being often comparable to that of a single evaluation of f [10], since, in our case, the analytical expression of the gradient is at disposal.

In the case of interest, the analytical evaluation of ∇f requires the evaluation of the partial derivatives of Ξ, and then those of σ_k, with respect to the χ_r's. The derivative of interest can be written as [11]:

$$\frac{\partial \sigma_k}{\partial \chi_r} = \frac{1}{2\sigma_k}\left[\underline{u}_k^H\left(\frac{\partial \underline{T}}{\partial \chi_r}\underline{T}^H + \underline{T}\left(\frac{\partial \underline{T}}{\partial \chi_r}\right)^H\right)\underline{u}_k\right], \quad (10)$$

where $\underline{u}_k$ is the k-th left singular vector of the matrix $\underline{T}$, respectively, while $\partial \underline{T}/\partial \chi_r$ denotes a matrix whose entries are the derivatives of the entries of $\underline{T}$, shown in Eq. (6), with respect to the χ_r's, which in turn involve the derivatives of the points coordinates with respect to the χ_r's, and the apex H stands for Hermitian. Regarding the computational point of view, for the considered test cases, the calculation of Eq. (10) is mainly burdened by the term $\partial \underline{T}/\partial \chi_r$. Anyway, the evaluation time can be reduced by recasting Eq. (10) to calculate simultaneously all the derivatives, using the optimized matrix-matrix multiplications [12], as:

$$\frac{\underline{\rho}}{2}.* diag\left[\underline{\underline{U}}^H\left(\frac{\partial \underline{\underline{T}}}{\partial \chi_r}\underline{\underline{T}}^H + \underline{\underline{T}}\left(\frac{\partial \underline{\underline{T}}}{\partial \chi_r}\right)^H\right)\underline{\underline{U}}\right], \quad (11)$$

where $\underline{U}$ is the matrix of the left singular vectors, *diag* provides the diagonal entries of the argument, the symbol .* represent the element-wise multiplication, and $\underline{\rho}$ is a vector such that $\rho_k = 1/\sigma_k$. In particular the entries of $\partial \underline{T}/\partial \chi_r$ are given by:

$$\frac{1}{z_0}\int_{-a_{ap}}^{a_{ap}}\int_{-b_{ap}}^{b_{ap}}[g\left(\frac{\partial f}{\partial \chi_r}h_y + \frac{\partial h_y}{\partial \chi_r}f\right) +$$
$$\frac{\partial g}{\partial \chi_r}fh_y]\Lambda_{p(s)}(c_x, x')\,\Lambda_{q(s)}(c_y, y')dx'dy', \quad (12)$$

where f, g, h_y and the corresponding derivatives are evaluated at the m-th observation point, and

$$\frac{\partial f(R)}{\partial \chi_r} = \begin{cases} \frac{t(R)(x-x')}{R}\tau_r^x(\xi,\eta) & \text{for } 1\leq r\leq W \\ \frac{t(R)(y-y')}{R}\tau_r^y(\xi,\eta) & \text{for } W+1\leq r\leq 2W \end{cases}, \quad (13)$$

with

$$t(R) = \frac{1}{2\pi}\left(-3j\beta - \frac{3}{R} + \beta^2 R\right)\frac{e^{-i\beta R}}{R^3}, \quad (14)$$

and

$$\frac{\partial g}{\partial \chi_r} = \begin{cases} 0 & \text{for } 1\leq r\leq W \\ 2(y-y')\tau_r^y(\xi,\eta) & \text{for } W+1\leq r\leq 2W \end{cases}, \quad (15)$$

while the term $\partial h_y/\partial \chi_r$ depends on the peculiar choice for h_y and is here omitted for just the sake of brevity.

IV. RESULTS

A numerical analysis has been carried by performing the optimization of Ξ, by using both the numerical and the analytical evaluation of the gradient, for antennas with different sizes and a fixed aspect ratio $a_{ap}/b_{ap} = 5/3$. In particular, Case A, B and C refer to antennas with $2a_{ap}=5\lambda$, $2a_{ap}=10\lambda$ and $2a_{ap}=15\lambda$, respectively. For each case, as mentioned before (for a deeper discussion see [2,3]), Ξ has been optimized for different values of M, using the solution obtained at the previous step as starting point of the current one. In particular, by assuming $M=N_xN_y$, the values for M are here obtained by progressively increasing N_y, and using $N_x/N_y=5/3$, according to the aspect ratio of $\mathcal{A}$. The results are reported in Table1 wherein, for each value of N_y, the number of iterations (#it), the execution time and the optimal values of Ξ are shown. By labeling as t_N and t_A the execution times associated to the numerical and analytical case, respectively, the corresponding speedup $S=t_N/t_A$ has been calculated for each value of N_y. Also, the whole speedup S_C for each case is shown. The tests have been performed by using a compiled Matlab script on a PC with an Intel I7-4712HQ CPU working at 2.3 GHz and 16 GB RAM. It's worth noting that, regarding the numerical evaluation of the gradient, different approaches can be adopted [13]. Here the forward finite difference scheme is adopted, the "fastest possible" derivative approximation. The results in Table 1 show that the approach based on the analytical expression of the gradient leads to a faster functional minimization even with respect to the fastest numerical evaluation of the gradient. Furthermore, as it can be noted, S_C remains about constant, even if the aperture area in the biggest case is increased of a factor 9 with respect to the smaller antenna. The behavior is justified by the equal number of expansion coefficients (gradient components) adopted in Eq. (9), 2W, which remains the same across all the test cases. Obviously, since the computing time grows with the antenna size, the faster calculation turns remarkable for larger antennas. Finally, the approach has been exploited for the experimental characterization of standard gain horn Narda 640, at the working frequency of 8 GHz, taking into account also for the probe effects as discussed above. The effective aperture parameters are $a_{ap}=4.9$ cm and $b_{ap}=3.9$ cm, while the measurements have been collected on a planar region with $z_0=37.5$ cm.

A standard OEWG working in the X band has been used as probe. The measurements have been carried out within the anechoic chamber available at the Dipartimento di Ingegneria Elettrica e delle Tecnologie dell'Informazione, Università di Napoli Federico II. In particular, two sets of measurements have been acquired, one for the optimized scanning and the other for the standard sampling, to perform a comparison. The characterization with the standard sampling has required about 5265 samples ($\lambda/2$ sampling rate), while the number of samples obtained with the proposed technique is equal to 130 (with P=6, Q=5). In Fig. 2 the DFS is reported, while in Fig. 3 the reconstructed FFP is presented (blue cross) together with the one obtained with the standard sampling (red lines), for v=0 and u=0, respectively ($u=\beta\sin\theta\cos\varphi$, $v=\beta\sin\theta\sin\varphi$). A satisfactory agreement is

obtained.

Table 1: Optimizer performance for the case of numerical and analytical gradient evaluation

|	Ny	Numerical Grad			Analitical Grad			S	S_C
		#it	t_N	Ξ	#it	t_A	Ξ		
Case A	6	14	13,8	25,4	28	10,3	25,4	1,3	
	8	12	5,4	34,3	5	3,5	34,3	1,5	1,7
	10	14	10,2	38,2	4	4,9	38,2	2,1	
	12	16	15,6	40,6	8	12,6	40,6	1,2	
Case B	12	5	194,4	110,8	30	230,9	107,7	0,8	
	14	6	330,9	123,1	11	132,7	122,9	2,5	2
	16	5	343,7	133,7	9	150,4	133,8	2,3	
	18	21	641,6	140,9	9	185,0	140,8	3,5	
Case C	19	4	2086,0	246,2	20	1698,1	249,8	1,2	
	21	40	3574,6	281,7	14	1410,1	273,9	2,5	2
	23	5	2085,2	295,8	11	1370,1	292,5	1,5	
	25	5	5460,9	308,0	9	1417,3	306,5	3,9	
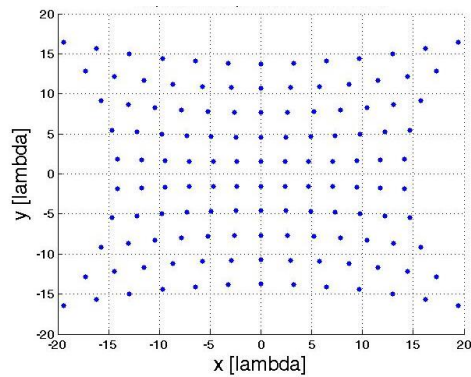
Fig. 2. The locations for the measurement points.
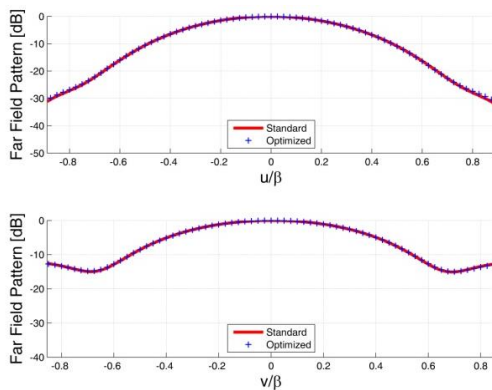
Fig. 3. Cut of the FFP along the u and v axis reconstructed with standard sampling (red line) and with optimized approach (blue cross).

V. CONCLUSIONS

The use of the analytical expression of the gradient evaluation in the optimized NF characterization has been adopted to speed-up the SVB optimization. The analysis show remarkable improvements in terms of computing time when comparing the proposed approach with the one based on the numerical evaluation of the gradient.

REFERENCES

[1] A. D. Yaghjian, "An overview of near field antenna measurements," *IEEE Trans. on Antennas and Propagation*, vol. 34, no. 1, pp. 30-45, 1986.

[2] A. Capozzoli, et al., "Singular value optimization in plane-polar near-field antenna characterization," *IEEE Antennas Prop. Mag.*, vol. 52, no. 2, pp. 103-112, Apr. 2010.

[3] A. Capozzoli, et al., "Field sampling and field reconstruction: a new perspective," *Radio Sci.*, vol. 45, RS6004, pp. 31, 2010.

[4] A. Capozzoli, et al., "NUFFT-accelerated plane-polar (also phaseless) near-field/far-field transformation," *Progress In Electromagnetics Research M*, vol. 27, pp. 59-73, 2012.

[5] A. Capozzoli, et al., "Photonic probes and advanced (also phaseless) near-field far-field techniques," *IEEE Antennas Prop. Mag.*, vol. 52, no. 5, pp. 232-241, Oct. 2010.

[6] A. Capozzoli, et al., "Multi-frequency planar near-field scanning by means of SVD optimization," *IEEE Antennas Prop. Mag.*, vol. 53, no. 6, pp. 212-221, Dec. 2011.

[7] A. Capozzoli, et al., "A probe compensated helicoidal NF-FF transformation for aperture antennas using a prolate spheroidal expansion," *Int. J. of Antennas Prop.*, vol. 2012, 2012.

[8] H. J. Landau and H. O. Pollak, "Prolate spheroidal wave functions, Fourier analysis and uncertainty – III: the dimension of essentially time- and band-limited signals," *Bell Syst. Tech. J.*, vol. 41, pp. 1295-1336, 1962.

[9] W. H. Press, et al., *Numerical Recipes in Fortran 77: The Art of Scientific Computing*, Cambridge University Press, 1992.

[10] Matlab User's Manual, http://it.mathworks.com/help/optim/ug/when-the-solver-might-have-succeeded.html

[11] G. H. Golub and C. F. Van Loan, *Matrix Computations*, Baltimore, John Hopkins University Press, 1996.

[12] K. Atkinson and D. D. K. Chien, "A fast matrix-vector multiplication method for solving the radiosity equation," *Adv. in Comput. Math.*, vol. 12, no. 2-3, pp. 151-174, Feb. 2000.

[13] N. S. Bakhvalov, *Numerical Methods*, Mir Publishers, Moscow, 1977.

INFORMATION FOR AUTHORS

PUBLICATION CRITERIA

Each paper is required to manifest some relation to applied computational electromagnetics. **Papers may address general issues in applied computational electromagnetics, or they may focus on specific applications, techniques, codes, or computational issues.** While the following list is not exhaustive, each paper will generally relate to at least one of these areas:

1. **Code validation.** This is done using internal checks or experimental, analytical or other computational data. Measured data of potential utility to code validation efforts will also be considered for publication.

2. **Code performance analysis.** This usually involves identification of numerical accuracy or other limitations, solution convergence, numerical and physical modeling error, and parameter tradeoffs. However, it is also permissible to address issues such as ease-of-use, set-up time, run time, special outputs, or other special features.

3. **Computational studies of basic physics.** This involves using a code, algorithm, or computational technique to simulate reality in such a way that better, or new physical insight or understanding, is achieved.

4. **New computational techniques** or new applications for existing computational techniques or codes.

5. **"Tricks of the trade"** in selecting and applying codes and techniques.

6. **New codes, algorithms, code enhancement, and code fixes.** This category is self-explanatory, but includes significant changes to existing codes, such as applicability extensions, algorithm optimization, problem correction, limitation removal, or other performance improvement. **Note: Code (or algorithm) capability descriptions are not acceptable, unless they contain sufficient technical material to justify consideration.**

7. **Code input/output issues.** This normally involves innovations in input (such as input geometry standardization, automatic mesh generation, or computer-aided design) or in output (whether it be tabular, graphical, statistical, Fourier-transformed, or otherwise signal-processed). Material dealing with input/output database management, output interpretation, or other input/output issues will also be considered for publication.

8. **Computer hardware issues.** This is the category for analysis of hardware capabilities and limitations of various types of electromagnetics computational requirements. Vector and parallel computational techniques and implementation are of particular interest.

Applications of interest include, but are not limited to, antennas (and their electromagnetic environments), networks, static fields, radar cross section, inverse scattering, shielding, radiation hazards, biological effects, biomedical applications, electromagnetic pulse (EMP), electromagnetic interference (EMI), electromagnetic compatibility (EMC), power transmission, charge transport, dielectric, magnetic and nonlinear materials, microwave components, MEMS, RFID, and MMIC technologies, remote sensing and geometrical and physical optics, radar and communications systems, sensors, fiber optics, plasmas, particle accelerators, generators and motors, electromagnetic wave propagation, non-destructive evaluation, eddy currents, and inverse scattering.

Techniques of interest include but not limited to frequency-domain and time-domain techniques, integral equation and differential equation techniques, diffraction theories, physical and geometrical optics, method of moments, finite differences and finite element techniques, transmission line method, modal expansions, perturbation methods, and hybrid methods.

Where possible and appropriate, authors are required to provide statements of quantitative accuracy for measured and/or computed data. This issue is discussed in "Accuracy & Publication: Requiring, quantitative accuracy statements to accompany data," by E. K. Miller, ACES Newsletter, Vol. 9, No. 3, pp. 23-29, 1994, ISBN 1056-9170.

SUBMITTAL PROCEDURE

All submissions should be uploaded to ACES server through ACES web site (http://aces-society.org) by using the upload button, Express Journal section. Only pdf files are accepted for submission. The file size should not be larger than 6MB, otherwise permission from the Editor-in-Chief should be obtained first. Automated acknowledgment of the electronic submission, after the upload process is successfully completed, will be sent to the corresponding author only. It is the responsibility of the corresponding author to keep the remaining authors, if applicable, informed. Email submission is not accepted and will not be processed.

EDITORIAL REVIEW

In order to ensure an appropriate level of quality control, papers are peer reviewed. They are reviewed both for technical correctness and for adherence to the listed guidelines regarding information content and format.

PAPER FORMAT

Only camera-ready electronic files are accepted for publication. The term **"camera-ready" means that the material is neat, legible, reproducible, and in accordance with the final version format listed below.**

The following requirements are in effect for the final version of an ACES Express Journal paper:

1. The paper title should not be placed on a separate page. The title, author(s), abstract, and (space permitting) beginning of the paper itself should all be on the first page. The title, author(s), and author affiliations should be centered (center-justified) on the first page. The title should be of font size 14 and bolded, the author names should be of font size 12 and bolded, and the author affiliation should be of font size 10 (regular font, neither italic nor bolded).

2. An abstract is required. The abstract should be a brief summary of the work described in the paper. It should state the computer codes, computational techniques, and applications discussed in the paper (as applicable) and should otherwise be usable by technical abstracting and indexing services. The word "Abstract" has to be placed at the left margin of the paper, and should be bolded and italic. It also should be followed by a hyphen (−) with the main text of the abstract starting on the same line.

3. All section titles have to be centered and all the title letters should be written in caps. The section titles need to be numbered using roman numbering (I. II. ….)

4. Either British English or American English spellings may be used, provided that each word is spelled consistently throughout the paper.

5. Internal consistency of references format should be maintained. As a guideline for authors, we recommend that references be given using numerical numbering in the body of the paper (with numerical listing of all references at the end of the paper). The first letter of the authors' first name should be listed followed by a period, which in turn, followed by the authors' complete last name. Use a comma (,) to separate between the authors' names. Titles of papers or articles should be in quotation marks (" "), followed by the title of the journal, which should be in italic font. The journal volume (vol.), issue number (no.), page numbering (pp.), month and year of publication should come after the journal title in the sequence listed here.

6. Internal consistency shall also be maintained for other elements of style, such as equation numbering. Equation numbers should be placed in parentheses at the right column margin. All symbols in any equation have to be defined before the equation appears or right immediately following the equation.

7. The use of SI units is strongly encouraged. English units may be used as secondary units (in parentheses).

8. Figures and tables should be formatted appropriately (centered within the column, side-by-side, etc.) on the page such that the presented data appears close to and after it is being referenced in the text. When including figures and tables, all care should be taken so that they will appear appropriately when printed in black and white. For better visibility of paper on computer screen, it is good to make color figures with different line styles for figures with multiple curves. Color should also be tested to insure their ability to be distinguished after black and white printing. Avoid the use of large symbols with curves in a figure. It is always better to use different line styles such as solid, dotted, dashed, etc.

9. A figure caption should be located directly beneath the corresponding figure, and should be fully justified.

10. The intent and meaning of all text should be clear. For authors who are not masters of the English language, the ACES Editorial Staff will provide assistance with grammar (subject to clarity of intent and meaning). However, this may delay the scheduled publication date.

11. Unused space should be minimized. Sections and subsections should not normally begin on a new page.

ACES reserves the right to edit any uploaded material, however, this is not generally done. It is the author(s) responsibility to provide acceptable camera-ready files in pdf and MSWord formats. Incompatible or incomplete files will not be processed for publication, and authors will be requested to re-upload a revised acceptable version.

COPYRIGHTS AND RELEASES
Each primary author must execute the online copyright form and obtain a release from his/her organization vesting the copyright with ACES. Both the author(s) and affiliated organization(s) are allowed to use the copyrighted material freely for their own private purposes.

Permission is granted to quote short passages and reproduce figures and tables from an ACES Express Journal issue provided the source is cited. Copies of ACES Express Journal articles may be made in accordance with usage permitted by Sections 107 or 108 of the U.S. Copyright Law. The consent does not extend to other kinds of copying, such as for general distribution, for advertising or promotional purposes, for creating new collective works, or for resale. The reproduction of multiple copies and the use of articles or extracts for commercial purposes require the consent of the author and specific permission from ACES. Institutional members are allowed to copy any ACES Express Journal issue for their internal distribution only.

PUBLICATION CHARGES
There is a $200 basic publication charge assigned to each paper for ACES members, and $300 charge for non-ACES members. Corresponding authors should be active members of the society at the time of submission and the time of publication in order to receive the reduced charge.

ACES Express Journal doesn't allow for more than four pages. All authors must comply with the page limitations. ACES Express Journal is an online journal, and printed copies are not available.

Upon completion of its first year, ACES Express Journal will be abstracted in INSPEC, in Engineering Index, DTIC, Science Citation Index Expanded, the Research Alert, and to Current Contents/Engineering, Computing & Technology.